

Applications of High Energy Theory to Superconductivity and Cosmic Inflation

Zhen Wang

Wanzhou, Chongqing, China

Master of Science, The College of William and Mary, 2012  
Bachelor of Science, Sichuan University, 2010

A Dissertation presented to the Graduate Faculty  
of the College of William and Mary in Candidacy for the Degree of  
Doctor of Philosophy

Department of Physics

The College of William and Mary  
August, 2016

© Copyright by Zhen Wang 2016

## APPROVAL PAGE

This Dissertation is submitted in partial fulfillment of  
the requirements for the degree of

Doctor of Philosophy



---

Zhen Wang

Approved by the Committee, May, 2016



Committee Chair

Class of 2017 Associate Professor Joshua Erlich, Physics  
The College of William & Mary



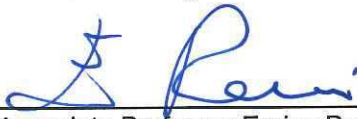
---

Professor Christopher Carone, Physics  
The College of William & Mary



---

Professor Todd Averett, Physics  
The College of William & Mary



---

Associate Professor Enrico Rossi, Physics  
The College of William & Mary



---

Associate Professor Sarah Day, Mathematics  
The College of William & Mary



---

Visiting Assistant Professor Daniel Vasiliu, Mathematics  
The College of William & Mary

## ABSTRACT

This dissertation examines applications of methods of high-energy theory to other physical systems: unconventional superconductors on the one hand, and cosmology on the other. Extra-dimensional models of superconductors, motivated by gauge/gravity duality in string theory, have proven remarkably successful in reproducing qualitative, and sometimes quantitative, aspects of unconventional superconductors. We analyze the universality of some of these predictions, and discover a universal relation between certain superconducting observables. The second part of this dissertation is about cosmic inflation. The evolution of the universe is sensitive to the fundamental particles and their interactions. We investigate models of cosmic inflation which involve the dynamics of one or more axion fields, and we explain how such models might be related to the flavor structure of the standard model.

## TABLE OF CONTENTS

Acknowledgements	iv
Dedications	v
List of Tables	vi
List of Figures	vii
Chapter 1. Outline	1
Chapter 2. Model Universality of Holographic Superconductors	3
2.1 Introduction	3
2.2 Introduction to Holographic Superconductors	5
2.2.1 Gauge/Gravity Duality	5
2.2.2 Superconductivity	8
2.2.3 Gravity Dual of Superconductor Theory	10
2.3 Holographic Superconductors	12
2.4 Deconstructed Holographic Superconductors	15
2.5 Results	16
2.6 Comments	21
Chapter 3. Inflation	24
3.1 Introduction to Inflation	24
3.1.1 The Expanding Universe	25
3.1.2 Idea of Inflation	30
3.1.3 Slow-Roll Inflation	31

3.1.4	Quantum Fluctuations and Large Scale Structure	34
3.2	Dante's Waterfall	39
3.2.1	Introduction	39
3.2.2	Single-Field Effective theory	42
3.2.3	Numerical Analysis	51
3.2.4	Comments	54
3.3	Field-Space Metric in Spiral Inflation and Related Models	55
3.3.1	Introduction	55
3.3.2	Single-Field Effective Description	58
3.3.3	Results	66
3.3.4	Comments	76
3.4	Flavored Axion-Monodromy Inflation	77
3.3.1	Introduction	77
3.3.2	Inflationary Trajectories	81
3.3.3	Models	88
3.3.4	Comments	92
Chapter 4.	Conclusions	94
Appendix A	Discrete Gauge Symmetries, Briefly	96
Bibliography		98



## ACKNOWLEDGEMENTS

In the past few years, it is so lucky for me to have the opportunity to work with my advisor, Joshua Erlich, who has constantly impressed me with his dedication, enthusiasm, and encyclopedic knowledge about physics. He has always been encouraging and helpful to me, making me feel determined no matter things are going well or not, and progress little by little, step by step. I want to thank Josh for what he taught me and what he has always been, which I will treasure all my life.

I want to thank all my collaborators, Christopher Carone, Anuraag Sensharma, Jackson Olsen, and Raymundo Ramos. We had very efficient cooperation and I learned a lot from them. This dissertation would not be possible without them.

I also want to thank all of my defense committee members for carefully reviewing my dissertation and making useful suggestions.

Thanks to all my teachers in William and Mary, Henry Krakauer, Kostas Orginos, Will Detmold, Shiwei Zhang, Carl Carlson, and etc. They have not only taught me physics but also influenced my theoretical thinking. I also want to thank all my previous teachers from college, high school, and every school I went to. I would not even be here without them.

Thanks to all my friends. I cannot list all of their names here but my life would be too boring to live without them. Thanks to Jidong Xiao, we played soccer video games together, and Yunhan Long, for all the useful knowledge he shared with me.

I owe my sincere thanks to my parents, who value my education above anything else. Their unselfish support has always kept me moving forward.

Last but not least, I want to thank my wife, Shu Zhang. I am truly blessed to have you in my life.

This Ph.D. is dedicated to my grandparents,  
Huang (1928 - 2011) and Wen (1933 - 2012).

## LIST OF TABLES

1. Observables for the Continuum Model	18
2. Critical Temperatures for the Deconstructed Model	20
3. Observables for the Deconstructed Model	21
4. Observables from the Single-Field Approximation for the $(p, n) = (4, 1)$ Model	70
5. Observables from the Single-Field Approximation for the $(p, n) = (4, 2)$ Model	73
6. $Z_{21}^\Phi$ Charge Assignment of the Standard Model Fermions	91

## LIST OF FIGURES

1. The Condensate and the Real Part of Conductivity for the Continuum Model	17
2. The Conductivity for the Continuum Model	18
3. The Condensate and the Real Part of Conductivity for the Deconstructed Model	20
4. The Conductivity for the Deconstructed Model	22
5. Conventional Big Bang Cosmology in Conformal Diagram	29
6. Inflation in Conformal Diagram	32
7. Evolution of the Cosmic Perturbations	36
8. The Potential of Dante's Inferno Wrapped in Cylindrical Coordinates	41
9. The Potential of Dante's Waterfall Wrapped in Cylindrical Coordinates	42
10. Inflationary Trajectory in Field Space of Dante's Waterfall	49
11. Time Evolution of the Fields	49
12. Contour Plot of the Potential with the Trajectory in Field Space	53
13. Dynamical Solutions of the Fields	53
14. The Potential of Dante's Inferno	56
15. The Potential of Spiral Inflation	57
16. Contour Plot for the $(p, n) = (4, 1)$ Model with the Trajectory in Field Space	71

17. The Eigenvalues and Eigenvectors of the Mass Matrices	72
18. The Larger Eigenvalue Compared to Hubble Scale for the $(p, n) = (4, 1)$ Model	72
19. Contour Plot for the $(p, n) = (4, 2)$ Model with the Trajectory in Field Space	73
20. The Larger Eigenvalue Compared to Hubble Scale for Dante's Waterfall	75
21. Inflationary Trajectory in Field Space for the Solution without Waterfall Termination	85
22. Inflationary Trajectory in Field Space for the Solution with Waterfall Termination	88

# Chapter 1

## Outline

This dissertation comprises two parts, each addressing an application of methods of high-energy theory to another physical system. The first half focuses on tests of universality of holographic superconductors; the second half is devoted to axion-monodromy models of cosmic inflation and an attempt to naturally link inflationary models with the standard model through the flavor sector.

AdS/CFT-inspired models of superconductors have successfully reproduced certain experimental features of high-temperature superconductors, such as a large gap-to- $T_c$  ratio compared to that of conventional superconductors. Similar phenomenology can be realized in the natural spatial dimension of the superconductors by dimensionally deconstructing these holographic models. The first half of this dissertation addresses the question of robustness of the quantitative success of holographic superconductors and deconstructed versions of those models. Chapter 2 describes our work on holographic models of superconductors and attempts to “deconstruct” those models in order to gain insights into the microscopic mechanisms responsible for certain features of unconventional superconductors. Some of these models are surprisingly successful at reproducing superconducting observables, so we consider variations of those models and analyze the universality of model predictions in order to determine the robustness of these predictions. We include an introduction to gauge/gravity duality and superconductivity, followed by a simple illustration of how the

duality has been used to model superconducting systems.

Axion-monodromy inflation models which incorporate a shift symmetry allow for the production of observably large primordial gravitational waves while maintaining sufficient number of  $e$ -folds of inflation. The second half of this dissertation proposes a class of spiral two-field axion-monodromy models with possible hybrid-type termination of inflation. Chapter 3 describes our work on models of cosmic inflation motivated by earlier work interpreting the inflaton field as a pseudo-Goldstone boson associated with the spontaneous breaking of an anomalous global symmetry. We include a review of standard cosmology and describe how the paradigm of inflation solves certain cosmological puzzles, and we review the calculation of observables in slow-roll inflation models. We demonstrate that the effects of the field-space metric on inflationary observables have consequences for the viability of these models. We also present a scenario in which the dynamics of the axions are related to the hierarchy of fermion masses.

## Chapter 2

# Model Universality of Holographic Superconductor

### 2.1 Introduction

Holographic models of nonperturbative physical systems have been more successful quantitatively than should have been expected. The most developed applications of holographic model building are to quantum chromodynamics (QCD) [1, 2], electroweak symmetry breaking [3] and condensed matter systems, especially superconductors [4, 5]. Arguments based on insensitivity to model details [6], approximate conformal invariance [7] and decoupling of high-dimension states and operators [8] have been put forward in an attempt to understand the unreasonable effectiveness of some of these models.

Holographic models of 3+1 dimensional systems are 4+1 dimensional theories in which the behavior of fields near the boundary of the spacetime, typically Anti-de Sitter (AdS) space, determines the properties of the corresponding lower-dimensional system. However, gauge theories in more than 3+1 dimensions are generally nonrenormalizable. Deconstruction of extra dimensions provides a gauge-invariant completion of higher-dimensional gauge theories [9, 10]. A deconstructed extra-dimensional model is a lower-dimensional theory which, below some energy scale, has an effective description in which one or more extra di-

mensions are latticized. Deconstruction is useful for model building in that it is sometimes possible to reduce the number of “lattice sites” to just a few while maintaining the interesting phenomenology of a higher-dimensional model, yielding a relatively simple model of the system of interest. For example, in the context of electroweak symmetry breaking, deconstruction provides one route to little Higgs models [11]. More recently, this approach has been used to construct models with some of the properties of holographic superconductors, even though defined in the natural dimension of the superconducting system [12].

Among the successful predictions of holographic models are certain features of high-temperature superconductors such as an enhanced ratio of the superconducting gap ( $\Delta$ ) to the critical temperature ( $T_c$ ) [5]. Bottom-up holographic models of finite-temperature systems typically begin with an AdS-Schwarzschild or AdS-Reissner-Nordstrom black hole geometry, the latter taking into account the backreaction of charge density on the geometry. These geometries are chosen mainly for simplicity, but in holographic models of superconductors derived from string theory [4], the spacetime geometries may be more complicated and depend on the fluxes of fields associated with D-brane configurations. Other geometric backgrounds in holographic models arise as the induced metric on a brane embedded in a higher-dimensional spacetime, such as on the flavor branes in the holographic QCD model of Sakai and Sugimoto [2], and these induced geometries are not derived as the solution to Einstein’s equation with a specified energy-momentum tensor.

It is the goal of this chapter to explore the sensitivity of observables to variations in the details of holographic models of superconductors and in deconstructed variations of those models. As such, we consider holographic superconductors in generalizations of the 3+1 dimensional AdS-Schwarzschild metric. We find certain generic features in the phenomenology of these models, but details such as the ratio of the superconducting gap to the critical temperature are sensitive to the model details, which suggests that successful quantitative predictions in prototypical models are likely accidental. This is not to say that those models will not prove valuable in explaining the puzzling properties of unconventional superconductors, only that quantitative predictions are more model dependent than one might have

hoped. It has already been noted that there are quantitative and even qualitative distinctions between superconducting models, for example between those which take into account the backreaction of the charge density on the metric and those that don't [5]. The work presented here focuses on sensitivity to the extra-dimensional spacetime, parametrizing the AdS black-hole metric in a particular way in order to quantify the variability of superconducting observables in a class of holographic models and in deconstructed versions of those models.

## 2.2 Introduction to Holographic Superconductors

Holographic superconductors, which are gravitational theories which describe superconducting systems, have drawn enormous interest from theorists for their quantitative effectiveness in describing certain High- $T_c$  superconductors. This chapter examines the universality of the surprising success of the prototypical holographic models of superconductors, focusing on tests of model sensitivity to variations of the spacetime background in the models. An introduction to the holographic approach and a brief review of the history of superconductors are given in this chapter, and the contents are organized as follows: In Sec. 2.2.1, some original inspirations for the holographic principle and a concise introduction of AdS/CFT correspondence is given. Sec. 2.2.2 contains the history of discovery of various superconductors and some basics of BCS theory and its difficulty explaining High- $T_c$  superconductors. Eventually, Sec. 2.2.3 is devoted to presenting the basic ideas behind modeling holographic superconductor, followed by the motivation of our research and technique used.

### 2.2.1 Gauge/Gravity Duality

The possibility of holography in the context of gauge/gravity duality is rooted in black hole thermodynamics. In the 1970s, Benkenstein and Hawking proposed that the entropy of a black hole depends on the area of its horizon [13]. In a gravitational theory, the entropy of a system is bounded by the entropy of a black hole that fits inside the volume, because by adding additional matter to a gravitational system, the entropy would increase and

ultimately a black hole would be formed. If the original system had a higher entropy than that of the black hole, the second law of thermodynamics would be violated. On the other hand, the maximum entropy is the logarithm of the number of distinct states, which is proportional to the volume of a non-gravitational system. Since entropy is a measure of the degrees of freedom, counting the degrees of freedom on both sides, a gravitational system may indeed contain the same amount of information with that of a non-gravitational system in one lower dimensional spacetime.

The Anti-de Sitter/Conformal Field Theory (AdS/CFT) correspondence, also known as gauge/gravity duality, realizes the holographic principle by relating gravity in a higher dimensional anti-de Sitter (AdS) space to conformal field theory (CFT) in a lower dimensional spacetime. In the original work of Maldacena [14], this correspondence had been based on the relationship between  $\mathcal{N} = 4$  supersymmetric  $SU(N)$  Yang-Mills theory and configurations of D-branes in Type IIB string theory. However, one can deform the geometry on gravity side at the cost of fewer symmetries of the field theory with certain limits applied. The claim is that the dynamics of the classical gravity theory in the bulk spacetime is determined by boundary effects and can be captured by a local field theory that lives in the boundary of the geometry or vice versa. For the classical gravity to be valid, we need the length scale of the higher-dimensional geometry to be large compared to Planck scale, which translates to two conditions in the field theory: strong coupling and large number of fields, also known as the large  $N$  limit, with  $N$  characterizing the gauge symmetry  $SU(N)$ . However, the duality has been proved to work well as phenomenological models even at relatively small  $N$ , for example  $N = 3$  in AdS/QCD. It should be made clear that there are three forms of the AdS/CFT conjecture and the version stated above is the weakest one. The strongest statement matches all the quantum states between the two sides with no limits imposed. A weaker statement requires the t' Hooft limit (large  $N$ ) and matches the field theory to classical solutions of the gravitational theory. These two versions of the conjecture are less tractable and need better understanding. Thus practically, we will follow the weakest claim which has been proved successful in various applications of the duality.

In the bottom-up model building with gauge/gravity duality, which is used in the work in this dissertation, we normally do not know the exact form of the Lagrangian of the field theory. This system is strongly coupled and cannot be solved perturbatively thus entails the use of holographic approach. The knowledge we have are the physical observables and consequently the relevant information of the operators in the field theory. For example, their quantum numbers and the global symmetry charges, if any. Also, every global symmetry would be associated with a conserved current, adding to the inventory of operators. Every operator  $\mathcal{O}^i(x)$  is coupled to a source  $J_i(x)$  and the generating functional is given by

$$e^{W[J]} = \langle e^{i \int \mathcal{O} J} \rangle \quad (2.1)$$

as usual. At this moment  $J_i(x)$ s are just background fields introduced for the purpose of N-point function calculation. However, they are also boundary values of fields that live in the bulk spacetime. For definiteness we assume the strongly coupled field theory lives in a 4-dimensional Minkowski boundary of a 5-dimensional gravitational geometry and  $z$  is the label for the extra dimension. The boundary theory is located at  $z = 0$  and the extra dimension is cut off at the horizon  $z = z_h$  for concreteness. If there is a black hole behind the horizon then this becomes a thermodynamical system because of the associated Hawking temperature. It should be noted that the introduction of the cut-off would break the conformal symmetry. The well known prescription of the duality reads

$$e^{W[J]} = \langle e^{i \int d^4x \mathcal{O}^i(x) J_i(x)} \rangle = e^{i S_{gravity}[\phi_i^{\text{cl}}]} \Big|_{\phi_i^{\text{cl}}(x, z=0) = J_i(x)}. \quad (2.2)$$

$\phi_i$ s are the bulk fields and the superscript cl indicate solution of classical equation of motion. The boundary condition at  $z = 0$  has been encoded in the prescription. On the other end of the extra dimension, the solution is required to be regular at  $z = z_h$ . In the case of the field theory living in a Minkowski boundary, besides the regularity condition, an ingoing wave boundary condition needs to be imposed at the horizon in order to get the correct retarded Green's function. The argument is based on causality that no matter is allowed

to evade a black hole. See [15] for more details. The field theory two-point function can then be calculated by taking second derivative of the on-shell gravity action with respect to the source  $J_i(x)$ , as usual. Since the operator  $\mathcal{O}^i(x)$  coupled to  $J_i(x)$  has the same quantum numbers in order for  $\mathcal{O}^i J_i$  to retain the symmetries, both  $\mathcal{O}^i(x)$  and  $J_i(x)$  should correspond to the same bulk field  $\phi_i$ . Solving the bulk equations of motion for  $\phi_i$ , one would arrive at two linearly independent solutions of  $z$  dependence. And these solutions are classified by their normalizability [16]. The nonnormalizable solution is interpreted as classical background and specifies the boundary condition thus its coefficient is set to the field theory source  $J_i(x)$ . The normalizable solution is the physical mode propagating in the extra dimension if one perturbs the background and its boundary value then correspond to the expectation value of the operator  $\mathcal{O}^i$ .

Before we embark on an exploration of holographic models, we present a brief introduction to traditional and high-temperature superconductors and their theoretical modeling in the following section.

### 2.2.2 Superconductivity

Superconductivity was first discovered by H. Kamerlingh Onnes. In 1908, he successfully liquefied Helium which enabled him to study conductivity at the temperature range of a few degrees Kelvin. In 1911, he found that for mercury, the resistivity suddenly drop to zero when cooled through 4.2K, which is material specific and called critical temperature  $T_c$ . Similar phenomenon were observed for some other metals like lead and tin. In 1933, Meissner and Ochsenfeld found that magnetic fields are actively expelled from the interior of a superconductor in the sense that not only exterior fields are not allowed to enter but also existing fields in a superconductor in its normal state would be expelled as the transition to its superconducting phase. This Meissner effect is found to be reversible. When the applied magnetic field rises above a critical point  $H_c$ , superconductivity is destroyed. For more detailed review of the discovery of superconductivity, see [17].

These pure metal superconductors are called Type I superconductors with very low

$T_c$  and  $H_c$  values. They have been well understood and explained by the BCS theory proposed by John Bardeen, Leon Cooper, and Robert Schrieffer in 1957. The core idea of BCS theory is that electrons form a condensate in the form of pairs (Cooper pairs) when superconducting and travel with a collective wave function. More importantly, below  $T_c$ , there is a band gap opening. The experimental observation of isotopic mass dependence of the band gap suggests the condensate energy, hence the binding force of the Cooper pair, is somehow related to the lattice, which leads to the idea that the pair of electrons are interacting through phonons of the lattice vibration. According to the BCS theory, in a nutshell, the first electron attracts nearby ions which creates local excessive positive charge thus overcomes the repulsive Coulomb force and a net attractive interaction with a second electron results.

BCS theory has been highly successful explaining Type I superconductors. One of the most important predictions it made is about the band gap. At 0K, the gap energy, or the minimum energy for a paired electron to be thermally excited, is found to be

$$\Delta(0) = 1.76k_B T_c. \quad (2.3)$$

And near  $T = T_c$ , the gap energy obeys

$$\frac{\Delta(T)}{\Delta(0)} \approx 1.74\left(1 - \frac{T}{T_c}\right)^{1/2}. \quad (2.4)$$

Experimental measured values of  $2\Delta(0)$  for Type I superconductors range from  $3.0k_B T_c$  to  $4.5k_B T_c$  and are peaked around  $3.5k_B T_c$ , confirming the BCS prediction. The above result is based on the weak coupling limit that is generally true for Type I superconductors, requiring  $N(0)V \ll 1$ , where  $N(0)$  is the density of state per unit energy and  $V$  measures the pairing interaction. Stronger coupling superconductors were found later with higher critical temperature and magnetic field than those of Type I superconductors. They are characterized with the existence of a mixed state sometimes called vortex state, allowing magnetic fields penetrating into the interior of the superconductor in the form of Abrikosov

vortices.

In 1986, cuprate ceramic superconductors were discovered with  $T_c > 30K$  [18]. Because their mechanism cannot be explained by BCS theory, for example the gap to critical temperature ratio  $\Delta/T_c$  is larger than BCS predictions, they are simply referred as high- $T_c$  superconductors. Some of the attributions of high- $T_c$  superconductors still lack reliable microscopic theoretical understanding including pseudogap phase and Nernst effect in both superconducting and pseudogap phase. Pseudogap is a partial energy gap opening up between  $T_c$  and a larger temperature  $T^*$  in the normal state. Iron based high- $T_c$  superconductors were discovered in 2006 and their mechanism remains to be better understood as well. In the next section, a most popular example of holographic description of these systems is briefly reviewed and some extension followed.

### 2.2.3 Gravity Dual of Superconductor Theory

Inspired by the surprising success of AdS/QCD, since high- $T_c$  superconductors are also strongly coupled systems, it is natural for theorists to think of their gravitational description in the sense of AdS/CFT and some of the earliest works can be found at [4, 5]. These gravity duals are called holographic superconductors in that they live in higher dimensional spacetime and the prototype model realizes the physics with an Abelian higgs model in  $AdS_4$  space with a Schwarzschild black hole background to model the planar cuprate superconductors in two spatial dimensions. To start building the extra dimensional Lagrangian, the first step involves determining the operators in the field theory. The BCS theory is essentially a Hartree-Fock theory with a Cooper pair operator generating nonvanishing expectation value for  $T < T_c$ . In its stronger coupled cousins, one still expects a condensate operator  $\mathcal{O}$ . In this dissertation, only spin singlet s-wave condensate that has spherically symmetric spatial wave function has been researched. Therefore, this scalar condensate operator  $\mathcal{O}$  would be dual to a bulk scalar field  $\Psi$ . In addition to the condensate operator, we need a electromagnetic current  $J_\mu$  resulting from a global symmetry that is dual to a  $U(1)$  gauge field  $A_\mu$  in gravity side. For temperature below  $T_c$ , the condensate, read off from

the boundary behavior of  $\Psi$  as coefficient of its normalizable mode, acquires nonvanishing profile, rendering the photon massive thus leading to superconductivity in the field theory.

The formation of unstable scalar modes is said to be a classical instability for the black hole to develop hair. For the scalar field  $\Psi$  charged under  $U(1)$  gauge symmetry, its effective mass gets a negative contribution from the coupling with the gauge field  $A_\mu$  through covariant derivative. As one lower the temperature while fixing charge density, this negative contribution becomes more significant and finally renders  $\Psi$  tachyonic. See [4] for more detailed analysis. Though not relevant to the work in this dissertation, it's worth noting that in the case of neutral scalar field, the black hole also gets hairy at low temperature [5].

A technique called deconstruction is used in our work to effectively, below some energy scale, describe the higher dimensional gravitational dual theory in one fewer dimensional spacetime. Mathematically, the process is realized by discretization of the equations of motion on the extra dimension and reproducing the physics with chains of fields in lower dimensional spacetime. The physical contents of the deconstructed theory are designed to imitate the classical dynamics in the extra dimension. One of the original motive for deconstruction is that gauge theories in more than  $3+1$  dimensions are non-renormalizable, which does not apply to the case here since the holographic theory lives in  $AdS_4$ . That said, it is still intriguing to have a theory lives in the natural dimensional spacetime of the physics described by it.

One of the most significant successes of these holographic models for High- $T_c$  superconductors is the prediction of a higher gap to  $T_c$  ratio than that of BCS theory [5]. However, as mentioned in Sec. 2.2.1, these bottom-up models live in the geometry chosen by the model builder, therefore the sensitivity of the quantitative and qualitative predictions with respect to different spacetime metrics remains to be of our interest. In this chapter, the spacetime geometry of holographic superconductor is parametrized and varied in a particular way based on the original  $AdS_4$  space. The observables are calculated against a series of metrics to explore the pattern of the quantitative predictions and any generic features of a class of these models .

## 2.3 Holographic Superconductors

Here we briefly review the construction of holographic superconductor models and the calculation of observables in those models. In a holographic superconductor, a charged field condenses in an extra-dimensional black-hole background whose Hawking temperature is below some critical temperature  $T_c$ . The temperature of the lower-dimensional system is identified with the Hawking temperature of the higher-dimensional black hole [19]. The charged condensate spontaneously breaks the electromagnetic  $U(1)$  gauge group<sup>1</sup> and gives rise to superconducting phenomenology [5].

In this work we ignore the backreaction of the charge density on the spacetime geometry, and for now we consider an Abelian Higgs model in a 3+1 dimensional AdS-Schwarzschild spacetime background. This is meant to describe a system which is superconducting in two spatial dimensions, *e.g.* the copper-oxide planes of cuprate superconductors. We can choose coordinates such that the lengths are normalized to the AdS scale and the metric has the form

$$ds^2 = \frac{1}{z^2} \left[ f(z) dt^2 - \frac{1}{f(z)} dz^2 - (dx^2 + dy^2) \right], \quad (2.5)$$

where

$$f(z) = 1 - \frac{z^p}{z_H^p}, \quad (2.6)$$

with  $p = 3$  corresponding to the 3+1 dimensional AdS-Schwarzschild metric.

With the Euclidean time  $\tau \equiv it$  compactified with period  $1/T$ , the Hawking temperature associated with the modified black-hole metric follows from the condition that there be no conical singularity at the horizon. In the absence of a conical singularity, if  $z^*$  is the proper distance from the horizon  $z = z_H$  to a nearby point displaced only in the radial ( $z$ ) direction and  $\beta^*$  is the proper circumference of the Euclidean-time circle at that fixed radial position, then  $2\pi z^* = \beta^*$ . For metrics of the form (2.5), for small proper displacements from the

---

<sup>1</sup>To be precise, the  $U(1)$  gauge invariance of the holographic model corresponds to a global  $U(1)$  symmetry of the lower-dimensional system. However, as argued in Ref. [5], this global  $U(1)$  can be weakly gauged in order to determine some aspects of the dynamics of the corresponding superconducting system.

horizon,

$$\begin{aligned} 2\pi z^* &= 2\pi \int_{z_H-\varepsilon}^{z_H} \frac{dz}{z\sqrt{f(z)}} = \int_{z_H-\varepsilon}^{z_H} \frac{dz}{z_H\sqrt{-(z_H-z)f'(z_H)}} \\ &= \frac{4\pi\sqrt{\varepsilon}}{z_H\sqrt{-f'(z_H)}}, \end{aligned} \quad (2.7)$$

$$\beta^* = \frac{\sqrt{f(z_H-\varepsilon)}}{z_H-\varepsilon} \frac{1}{T} = \frac{\sqrt{-f'(z_H)}}{z_H} \frac{\sqrt{\varepsilon}}{T}, \quad (2.8)$$

and with  $f(z)$  given by Eq. (2.6), the Hawking temperature is then:

$$T = -\frac{4\pi}{f'(z_H)} = \frac{p}{4\pi z_H}. \quad (2.9)$$

In the continuum model, observables are independent of the choice of coordinates. However, away from the continuum limit, the deconstructed models are sensitive to the latticization of the extra dimension, which in turn depends on the coordinate choice. In the continuum model, the action for the scalar field  $\psi$  and U(1) gauge field  $A_M$  ( $M \in \{0, 1, 2, 3\}$ ) is

$$S = \int d^4x \sqrt{g} \left[ -\frac{1}{4} F_{MN} F^{MN} + |(\partial_M - iA_M)\psi|^2 - m^2 |\psi|^2 \right], \quad (2.10)$$

where  $g_{MN}$  is the metric defined by Eq. (2.5). For definiteness we take  $m^2 = -2$  in AdS units, as in Refs. [5] and [12].

Near the boundary  $z = 0$ , the field  $\psi$  has solutions

$$\psi(z) \sim \psi^{(1)}z + \psi^{(2)}z^2. \quad (2.11)$$

In this model both independent solutions for  $\psi(x, z)$  have finite action, so the AdS/CFT interpretation of the two solutions is ambiguous. Here we choose the interpretation that  $\psi^{(2)}$  is the condensate of the Cooper pair operator, while  $\psi^{(1)}$  would then be the external source for that operator, which we assume vanishes. Hence,  $\psi^{(1)} = 0$  is a boundary condition for the solutions of interest.

The bulk U(1) gauge field,  $A_M$ , is dual to the electric current and the background

electromagnetic field. In order to allow for nonvanishing chemical potential and charge density, we consider solutions in which the time component,  $A_0$ , is nonvanishing. The equations of motion have solutions for which  $A_0$  behaves near the boundary as

$$A_0 \sim \mu - \rho z, \quad (2.12)$$

where  $\mu$  is the coefficient of the non-normalizable solution and is identified with the chemical potential, which is a source for  $\rho$ , the charge density.

The phenomenology of the model is determined by fixing the temperature  $T$  as it appears in the AdS black-hole metric, solving the coupled equations of motion for  $\psi$  and  $A_M$  subject to the ultraviolet (*i.e.*  $z = 0$ ) boundary conditions  $\psi^{(1)} = 0$ ,  $A_0(0) = \mu$ , and the infrared (*i.e.*  $z \rightarrow z_H$ ) boundary conditions  $A_0(z_H) = 0$  and  $f'(z_H)z_H\psi'(z_H) = m^2\psi(z_H)$ . The last condition follows from the equations of motion, but is enforced as a regularity condition on the numerical solutions. The Cooper pair condensate  $\langle O_2 \rangle$  and background charge density are then determined by  $\psi^{(2)}$  (*c.f.* Eq. (2.11)) and  $\rho$  (*c.f.* Eq. (2.12)), respectively. Varying the temperature  $T$  then allows for a determination of the phase structure of the model, as  $\langle O_2 \rangle = 0$  for  $T > T_c$ .

To analyze the frequency-dependent conductivity we fix the background for  $\psi$  and instead solve the equations of motion for  $A_M$  in a background with  $A_a = e^{-i\omega t}\varepsilon_a A(z)$ ,  $a \in \{1, 2\}$ , corresponding to a uniform oscillating background electric field  $E_a = \partial_0 A_a|_{z \rightarrow 0}$ , polarized in the  $\varepsilon_a$  direction. Solutions are chosen to be ingoing at the horizon in order to enforce causal behavior of the current two-point function [15]. The solution for  $A_a \sim A_a^{(0)} + J_a z$  as  $z \rightarrow 0$  then determines the electric current  $J_a(\omega)$ , from which the conductivity,  $\sigma = J^a/E_a$  follows. A generic feature of superconductors is the existence of a frequency gap  $\omega_g$  below which there are no modes available to excite and generate a current, so that  $\sigma(\omega) = 0$  for  $\omega < \omega_g$  for  $T = 0$ . For nonvanishing temperature, even as  $\omega \rightarrow 0$  the current may be nonvanishing, where for small enough temperature  $\sigma(\omega \rightarrow 0) \propto \exp^{-\Delta/T}$ , where  $\Delta$  is the superconducting gap. From the weakly coupled BCS theory, we would expect  $\Delta \approx \omega_g/2$ , which also appears to be satisfied in the original model of Ref. [5].

## 2.4 Deconstructed Holographic Superconductors

We will study a class of models, based on the models of Ref. [12], in which the extra dimension of the holographic superconductor is deconstructed. Models with certain similarities to these were also considered in Ref. [20]. The higher-dimensional U(1) gauge theory is replaced by a  $U(1)^N$  gauge theory in one fewer dimension, where  $N \rightarrow \infty$  in the continuum limit. Scalar link fields charged under “neighboring” pairs of U(1) gauge groups are arranged to have prescribed expectation values, breaking the  $U(1)^N$  gauge group in such a way that the resulting action is that of the latticized higher-dimensional theory. The massive gauge fields replace the Kaluza-Klein modes in the continuum model. The fluctuations of the link fields do not correspond to degrees of freedom in the continuum theory, so we assume that they are heavy compared to the scales of interest in our analysis and disregard them in our analysis.

Expanding the fields in components, the action of the holographic model is,

$$S = \int d^4x \left[ \frac{1}{2}F_{0z}^2 + \frac{1}{2f(z)}F_{0a}^2 - \frac{f(z)}{2}F_{za}^2 - \frac{1}{4}F_{ab}^2 + \frac{1}{z^2f(z)}|\partial_0\psi - iA_0\psi|^2 - \frac{f(z)}{z^2}|\partial_z\psi - iA_z\psi|^2 - \frac{1}{z^2}|\partial_i\psi - iA_i\psi|^2 - \frac{1}{z^4}m^2|\psi|^2 \right], \quad (2.13)$$

where the lower-case Latin indices  $a, b$  are summed over the  $x$  and  $y$  coordinates. We now lattice the spacetime in one dimension by replacing the  $z$  coordinate by a discrete set of  $N$  points:

$$z_j = \begin{cases} \epsilon + (j-1)a & \text{for } j = 1, \dots, N-1 \\ \epsilon + (N-2)a + a_H & \text{for } j = N \end{cases}, \quad (2.14)$$

where  $z_N = z_H$ ,  $a$  is the lattice spacing in  $z$ -coordinates, and  $\epsilon$  is a UV cutoff. The Lagrangian for the deconstructed theory is of the form,

$$\mathcal{L} = \sum_{j=2}^{N-1} \left[ -\frac{1}{4}(F_{\mu\nu})_j(F^{\mu\nu})_j + Z_j|D_\mu\psi_j|^2 \right] + \sum_{j=1}^{N-1} [|D_\mu\Sigma_j|^2 - Z_jV_j], \quad (2.15)$$

where  $V_j$  is the scalar potential for link field  $\Sigma_j$ , and the coefficients  $Z_j$  and metric factors

$g_{\mu\nu}^j$  by which indices are contracted vary with lattice position  $j$ . The parameters in the model may be chosen (see Ref. [12] for more details) such that the effective theory below the scale set by the link fields is given by the Lagrangian,

$$\begin{aligned}\mathcal{L} = & \sum_{j=1}^{N-1} a_j \left[ \frac{1}{2}(\phi'_j)^2 - \frac{f_j}{2}(A'_{aj})^2 - \frac{f_j}{z_j^2}|\psi'_j|^2 \right] + \sum_{j=2}^{N-1} a_j \left[ \frac{1}{2f_j}(F_{0a})_j^2 - \frac{1}{4}(F_{ab})_j^2 \right] \\ & + \sum_{j=2}^{N-1} a_j \left[ \frac{1}{z_j^2 f_j} |\partial_0 \psi_j - i\phi_j \psi_j|^2 - \frac{1}{z_j^2} |\partial_a \psi_j - iA_{aj} \psi_j|^2 - \frac{1}{z_j^4} m^2 |\psi_j|^2 \right],\end{aligned}\quad (2.16)$$

where  $\phi_j \equiv A_j^0$ ,  $f_j \equiv f(z_j)$ , and the primes correspond to discretized derivatives, for example

$$\phi'_j \equiv \frac{\phi_{j+1} - \phi_j}{a}. \quad (2.17)$$

The U(1) gauge group at the first lattice site (the UV boundary site) is identified with the electromagnetic gauge group. Solutions to the equations of motion with discretized versions of the boundary conditions on the fields  $\psi$  and  $A_M$  allow for the calculation of observables by analogy with the holographic analysis in the continuum model [12]. In the case of a small number of lattice sites there is no *a priori* reason to expect phenomenology similar to that of the continuum model. Indeed, we find significant deviation from the predictions of the continuum model, though certain qualitative features remain. More complete details of these computations are presented below.

## 2.5 Results

To consider the sensitivity of observables to the spacetime geometry, we allow the power  $p$  in Eq. (2.6) to deviate from its value  $p = 3$  corresponding to the AdS-Schwarzschild spacetime. For generic  $p$  the metric is not a solution to Einstein's equations with a prescribed energy-momentum tensor. However, the initial choice of AdS-Schwarzschild geometry was made for simplicity and is equally arbitrary, and we can imagine either fluxes of fields that would give rise to the requisite energy-momentum tensor, or we can imagine that the

class of spacetimes described here corresponds to the induced metric on a brane embedded in a particular higher-dimensional spacetime. The goal here is to parametrize a class of deviations from the prototypical spacetime in order to analyze the sensitivity of observables to the detailed form of the spacetime metric. Our particular choice of parametrized metric is mostly arbitrary, though the class of spacetimes considered here remains asymptotically AdS near the boundary at  $z = 0$ .

We first analyze the continuum theory for  $p = 3, 3.5$  and  $4$ . In our numerics, we cut off the spacetime in the UV at  $z = 10^{-4}$  and near the horizon at  $z = z_H - 10^{-5}$ . We impose the boundary conditions discussed previously, and we fix  $\rho = 1$ , which by a scaling relation in the model also fixes  $T_c \propto \rho^{1/2}$  [5]. The superconducting condensate and the real part of the conductivity are plotted in Fig. 2.1. The delta function in the real part of the conductivity may be inferred from a pole in the imaginary part, not shown in the figure, by the Kramers-Kronig relation for the conductivity.

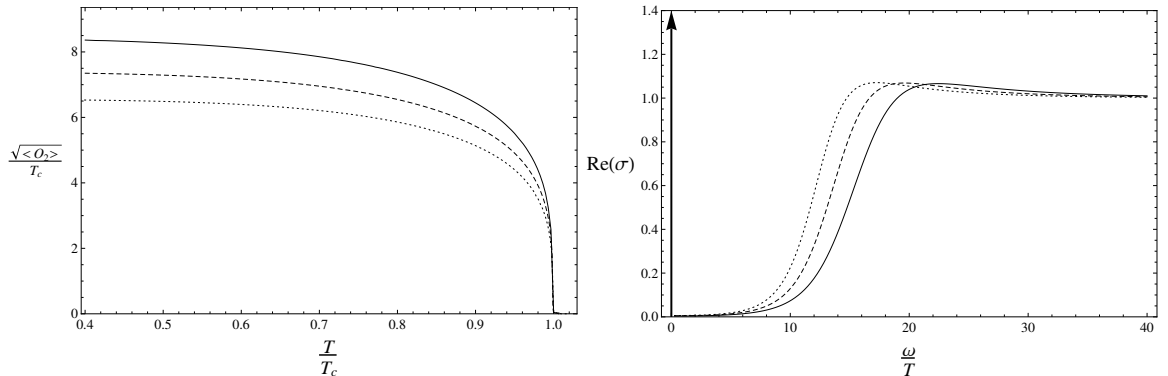


Figure 2.1: The condensate  $\langle O_2 \rangle$  and the real part of conductivity  $\sigma$ , at  $T/T_c = 0.5$ , for the continuum theory. Solid, dashed and dotted curves have  $p = 3, 3.5$  and  $4$ , respectively. The arrow indicates a Dirac delta function. The critical temperature  $T_c$  in unit of  $\rho^{1/2}$  for  $p = 3, 3.5$  and  $4$  are  $0.119, 0.135$  and  $0.153$ , respectively.

At low temperature the conductivity features a sharp gap below which the real part of the conductivity nearly vanishes. At the gap frequency,  $\text{Re}(\sigma)$  display a step-function type behavior, while  $\text{Im}(\sigma)$  has a sharp local minimum. Even at larger temperatures, we define the gap frequency  $\omega_g$  as the location of the local minimum of  $\text{Im}(\sigma)$ . In Fig. 2.2, we plot the conductivity with respect to frequency scaled in units of  $\sqrt{\langle O_2 \rangle}$ . Note that the three plots

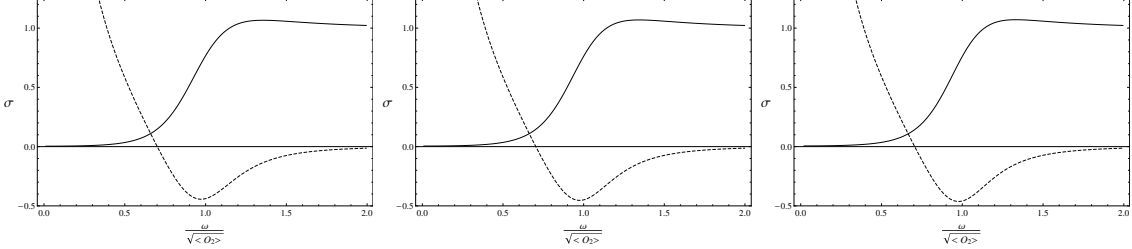


Figure 2.2: The conductivity at  $T/T_c = 0.5$  for the continuum model with different values of  $p$  in the metric. The solid lines are the real part of the conductivity, the dashed are the imaginary part. The  $p$  values for plots from left to right are 3, 3.5 and 4, respectively. The delta function in the real part at  $\omega = 0$  is not shown. Note the similarity of the three plots.

are nearly identical. In particular, the ratio  $\omega_g/\sqrt{\langle O_2 \rangle}$  at the minimum of  $\text{Im}(\sigma)$  is nearly independent of  $p$  in this range. However, as we will see there are important quantitative distinctions at small  $\omega$ .

It was noted in the original model of Ref. [5] that the gap-to- $T_c$  ratio is larger in the holographic model than in the weakly-coupled BCS theory, in rough quantitative agreement with experimental results in high-temperature superconductors. The normal component of the DC conductivity is defined as  $n_n \equiv \lim_{\omega \rightarrow 0} \text{Re}[\sigma(\omega)]$ . For low enough temperatures, we find that

$$n_n \sim e^{-\Delta/T}, \quad (2.18)$$

in which  $\Delta = C_p \sqrt{\langle O_2 \rangle}$ , for some constant  $C_p$ . The coefficient  $\Delta$  in the exponent is the superconducting energy gap. In order to compare with  $\omega_g$  found previously, we fit our data for a range of  $T/T_c$  around 0.5, which gives a good exponential fit for  $n_n$  in that range, with relatively large  $\Delta/T > 6$ . The results are summarized in Table 2.1.

$p$	3.0	3.5	4.0
$\frac{\sqrt{\langle O_2 \rangle}}{T_c}$	8.28	7.29	6.49
$\frac{\Delta}{\sqrt{\langle O_2 \rangle}}$	0.50	0.54	0.59
$\frac{\omega_g}{\sqrt{\langle O_2 \rangle}}$	0.97	0.98	0.98

Table 2.1: Observables for the continuum theory, at  $T/T_c = 0.5$ .

We next examine the deconstructed model with  $p = 3, 3.5$  and  $4$  for  $N \in \{5, 10, 100, 1000\}$ . We generally set the UV cutoff at  $z = \epsilon = 1$ , except for the case  $N = 1000$ , for which we set  $\epsilon = 0.1$  to better match the continuum model. The lattice spacing at the horizon is fixed at  $a_H = 10^{-5}$ , decoupled from the lattice spacing in the bulk which varies as the horizon moves with temperature. We again use a scaling relation to set  $\rho = 1$  so that  $T_c$  is fixed. As discussed in [12], we have the following discretized version of the boundary conditions:

$$\phi'_1 = -\rho = -1, \quad \psi^{(1)} = 0, \quad \phi_N = 0, \quad \text{and } \psi'_{N-1} = \frac{2}{3z_N} \psi_N, \quad (2.19)$$

where the primes are discretized derivatives as in Eq. 2.17. Electromagnetism is defined as the U(1) interaction at the UV boundary site, *i.e.* the lattice site closest to  $z = 0$ . We find solutions for which the  $x$ -component of the bulk gauge fields oscillate while the other components do not fluctuate,

$$A_{xi}(t) = e^{-i\omega t} A_{xi}, \quad (2.20)$$

where on the right-hand side of Eq. (2.20),  $A_{xi}$  is time-independent. The conductivity  $\sigma = J_1^x/E_{x1}$  is found to be given by a discretized version of the holographic calculation for  $\sigma$  in the continuum model:

$$\sigma = -\frac{if_1(A_{x2} - A_{x1})/a}{\omega A_{x1}}. \quad (2.21)$$

To obtain reasonable phenomenology we find that an ingoing-wave type boundary condition is necessary even in the deconstructed models. Due to the behavior of the metric near the horizon, we find it beneficial to impose a discretized version of the ingoing-wave boundary condition a bit away from the horizon in order to better mimic the continuum solutions. In particular, we impose the frequency-dependent boundary condition of Ref. [12]:

$$A_{xN-n} = 1 \quad \text{and} \quad A_{xN-n-1} = 1 - \frac{i\omega a}{f_{N-n-1}}. \quad (2.22)$$

The shift into the bulk, given by  $n$ , is chosen to be  $n = 20, 10, 2$  and  $2$  for  $N = 1000, 100, 10$  and  $5$ , respectively. In Fig. 2.3 we plot the condensate and the real part of the conductivity

for  $p = 3$ . It was suggested in Ref. [12] that the large resonances in the conductivity may correspond to exciton-polariton resonances due to the broken U(1) gauge groups in the model. The  $p = 3.5$  and 4 cases are qualitatively similar, and some examples are given in Fig. 2.4. The critical temperatures at which the condensate starts to form are listed in Table 2.2.

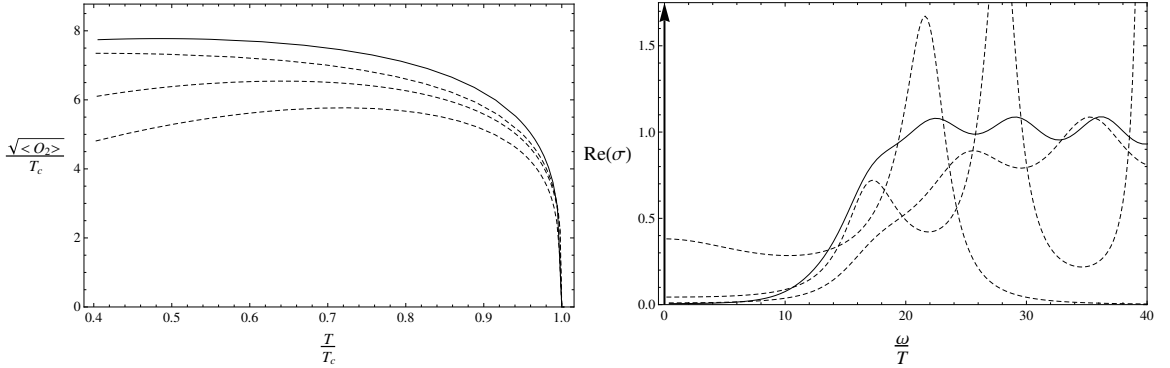


Figure 2.3: The condensate  $\langle O_2 \rangle$  and the real part of the conductivity for the deconstructed model for  $p = 3$  and  $T/T_c = 0.5$ . The solid curves correspond to  $N = 1000$  lattice sites. The dashed curves, in order from top to bottom near the origin in the left-hand plot and from bottom to top in the right-hand plot correspond to  $N = 100, 10$  and  $5$ , respectively. The arrow indicates a Dirac delta function from the DC superconductivity.

$N$	1000	100	10	5
$p = 3$	0.118	0.104	0.094	0.079
$T_c$	3.5	0.134	0.118	0.107
	4	0.151	0.132	0.121

Table 2.2: Critical temperatures in units of  $\rho^{1/2}$ .

To further analyze observables in the deconstructed models we mimic the analysis of the continuum model. It can be seen directly from the locations of the minimum of  $\text{Im}(\sigma)$  in Fig. 2.4 that  $\omega_g/\sqrt{\langle O_2 \rangle} \neq 1$ , but its value is not sensitive to  $p$  in the range examined, even in the 5-site model. The relation (2.18) continues to be well satisfied and defines the gap  $\Delta$  as in the continuum model. The pole in the imaginary part of the conductivity is manifest in Fig. 2.4, and is related to the delta-function in the real part via a Kramers-Kronig relation.

The results for observables are listed in Table 2.3.

$N$		1000	100	10	5
$\frac{\sqrt{\langle O_2 \rangle}}{T_c}$	$p = 3$	7.77	7.32	6.38	5.29
	3.5	6.85	6.48	5.61	4.62
	4	6.09	5.78	4.99	4.09
$\frac{\Delta}{\sqrt{\langle O_2 \rangle}}$	3	0.52	0.52	0.48	0.28
	3.5	0.58	0.58	0.56	0.33
	4	0.64	0.64	0.63	0.38
$\frac{\omega_g}{\sqrt{\langle O_2 \rangle}}$	3	1.03	1.55	1.22	1.83
	3.5	1.05	1.60	1.26	1.84
	4	1.06	1.64	1.30	1.85

Table 2.3: Observables for the deconstructed model. The  $\sqrt{\langle O_2 \rangle}$  and  $\omega_g$  in the table are taken at  $T/T_c = 0.5$ .

## 2.6 Comments

We have analyzed the dependence of the charged condensate and the complex conductivity on the form of the black-hole metric in holographic superconductors and in deconstructed versions of those models. We found that certain model predictions are relatively insensitive to the details of the spacetime. For example, the approximate relation between the gap frequency and the superconducting condensate,

$$\omega_g / \sqrt{\langle O_2 \rangle} = 1, \quad (2.23)$$

persists while the metric is varied in the continuum model. In the deconstructed model this ratio differs from 1, but remains insensitive to the deconstructed metric. On the other hand, we have seen relatively strong dependence of other observables on the details of the metric, such as the ratio of the superconducting gap  $\Delta$  to  $T_c$ . Furthermore, in deconstructed models we found that this ratio can be significantly smaller than in the continuum model.

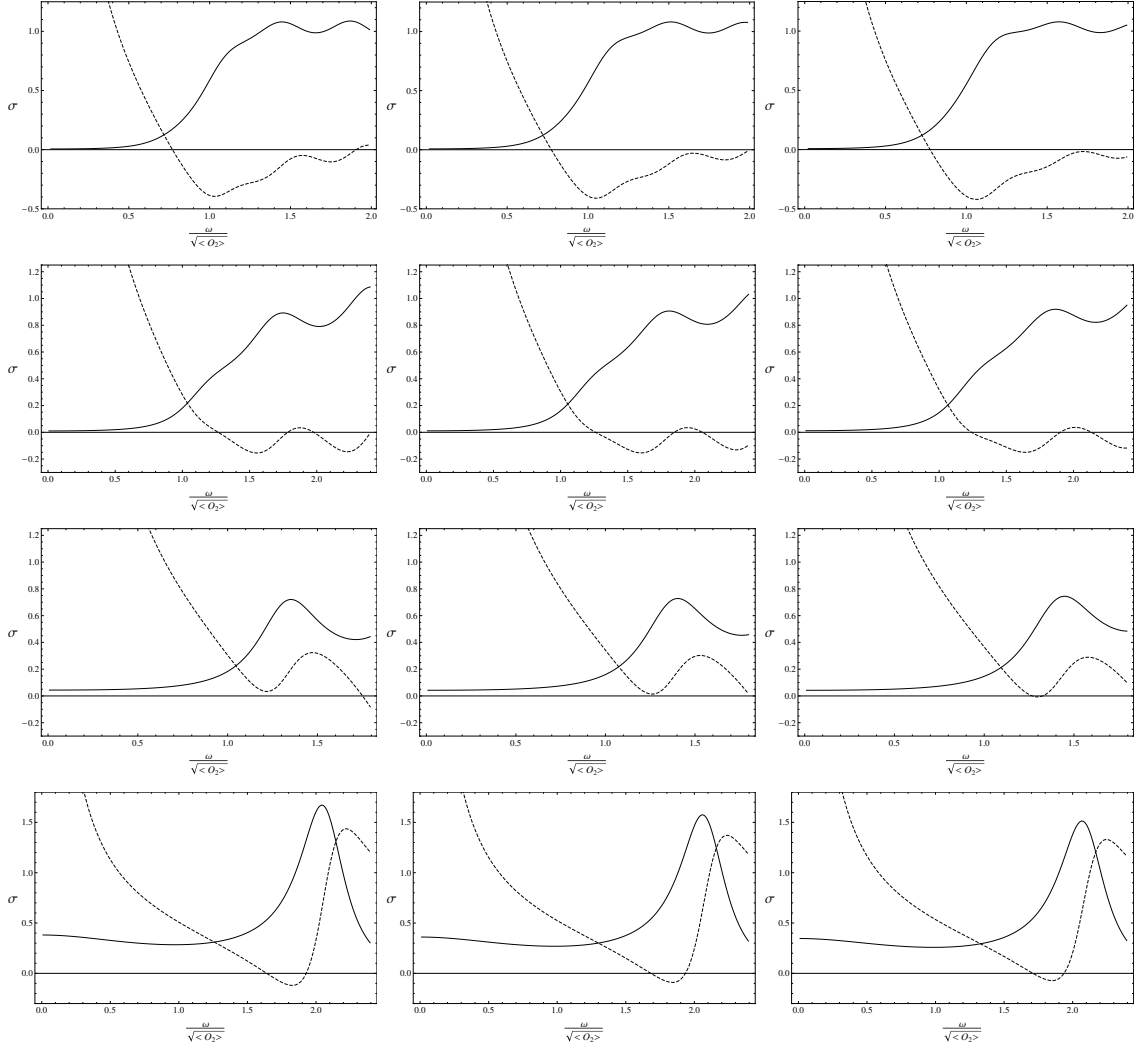


Figure 2.4: The conductivity at  $T/T_c = 0.5$  for the deconstructed model. The solid lines are the real part of conductivity, the dashed are imaginary. The  $p$  values for plots from left to right are 3, 3.5 and 4, respectively. The rows of plots from top to bottom correspond to  $N = 1000, 100, 10$  and 5, respectively.

The model sensitivity supports the conclusion that the quantitative success of the simplest holographic models of superconductors is accidental. However, in an effort to make contact with physical systems, it remains important to continue to investigate which aspects of the holographic models and their deconstructed cousins are responsible for the nonconventional behavior of the superconductors described by these models.

# Chapter 3

## Inflation

### 3.1 Introduction to Inflation

The ongoing experiments observing the cosmic background radiation like BICEP2 and Plank have been looking for evidence of cosmic inflation. Chapter 3 of this dissertation is focused on phenomenological models of inflation. This section presents a basic review of the ideas of cosmology and inflation. The conventional Big Bang theory requires fine-tuned initial conditions to explain the homogeneity and flatness of the observed universe. Although this is not a strict inconsistency, one would like a theory in which these features arise naturally. These two puzzles are solved by a period of inflation, in which the universe expands exponentially with a nearly constant Hubble parameter. This inflationary paradigm developed in the early 1980s in work by Starobinsky [21], Guth [22] and Linde [23]. In effective models of inflation, a spatially uniform scalar field called the inflaton provides the energy of inflation, and inflationary observables depend on the functional form of the inflaton potential. Slow-roll conditions are imposed in order to allow a sufficiently long period of accelerated expansion for the universe. The Lyth bound, which relates the ratio of power in tensor and scalar fluctuations to the number of  $e$ -folds of inflation, implies that the inflaton has to undergo a super-Planckian change in field value to produce an observably large signal of gravitational waves. However, this would render the effective theory invalid.

Axion-monodromy is one of the methods to evade the Lyth bound and several such scenarios are considered in Chapter 3. Contents of the rest of this section are organized as follows. In Sec. 3.1.1, the global description of homogeneous universe is reviewed. The classical dynamics of Inflation is introduced in Secs. 3.1.2 and 3.1.3. Sec. 3.1.4 explains how large-scale structure of the universe arise from theory of inflation.

### 3.1.1 The Expanding Universe

The observed universe displays large scale homogeneity and isotropy but with short scale irregularities, such as inhomogeneous matter distribution and Cosmic Microwave Background (CMB) anisotropies. Homogeneity means the universe is translationally invariant, and looks the same from every point. Isotropy mean every direction is identical thus the universe is rotationally invariant. This section is devoted to the global description of the homogeneous background and its dynamics, while the irregularities are considered later in Sec. 3.1.4.

Assuming the universe lives in a homogeneous and isotropic 3+1 dimensional spacetime, the Friedmann-Robertson-Walker (FWR) metric would be a natural choice for the geometry:

$$ds^2 = -dt^2 + a^2(t)d\Sigma^2, \text{ where } d\Sigma^2 = \frac{dr^2}{1 - kr^2} + r^2(d\theta^2 + \sin^2\theta d\phi^2). \quad (3.1)$$

This can be derived from the induced metric on a 3-dimensional sphere on which homogeneity and isotropy is apparent.  $k$  is a curvature parameter and  $k = +1, 0, -1$  correspond to positively curved, flat, and negatively curved hypersurface  $\Sigma$ , respectively. The scale factor  $a(t)$ , measuring the relative size of the hypersurface  $\Sigma$ , increases as the universe expands. The rate of expansion of the universe is characterized by the Hubble parameter  $H$ , defined as

$$H \equiv \frac{\dot{a}}{a}. \quad (3.2)$$

The Hubble time  $H^{-1}$  and Hubble length  $cH^{-1}$  set the fundamental scales, the age and size, for the universe. Before getting to the dynamics of the universe, the conformal time  $\tau$

is introduced for later convenience,

$$\tau = \int \frac{dt}{a(t)}. \quad (3.3)$$

The traveling of light follows the null geodesics given by  $ds^2 = 0$ . Since the hypersurface  $\Sigma$  is isotropic, one can just consider the radial direction for simplicity and the line element becomes

$$ds^2 = a(\tau)^2 (-d\tau^2 + d\chi^2). \quad (3.4)$$

This is also called the comoving coordinates. One can now write the geodesic as  $\chi(\tau) = \pm\tau + \text{const.}$ , which defines the light cone in  $\tau - \chi$  plane. This will be used for causal structure analysis later in this section.

The only time-dependent piece in the FRW metric is the scale factor  $a(t)$ , thus the dynamics of the homogeneous universe is essentially the evolution of  $a(t)$ , which is determined by the Einsteins equations

$$G_{\mu\nu} + g_{\mu\nu}\Lambda = 8\pi G T_{\mu\nu}, \quad (3.5)$$

where the  $\Lambda$  is a cosmological constant that is assumed to vanish in this section. The Einstein tensor  $G_{\mu\nu}$  is defined in terms of the Ricci tensor  $R_{\mu\nu}$  and the Ricci scalar  $R$ , which ultimately depends on the metric  $g_{\mu\nu}$ . Their explicit expressions are given below

$$G_{\mu\nu} \equiv R_{\mu\nu} - \frac{1}{2}g_{\mu\nu}R, \quad (3.6)$$

$$R_{\mu\nu} = \Gamma_{\mu\nu,\alpha}^\alpha - \Gamma_{\mu\alpha,\nu}^\alpha + \Gamma_{\beta\alpha}^\alpha \Gamma_{\mu\nu}^\beta - \Gamma_{\beta\nu}^\alpha \Gamma_{\mu\alpha}^\beta, \quad R \equiv g^{\mu\nu} R_{\mu\nu}, \quad (3.7)$$

where  $\Gamma_{\alpha\beta}^\mu \equiv \frac{1}{2}g^{\mu\nu}(g_{\alpha\nu,\beta} + g_{\beta\nu,\alpha} - g_{\alpha\beta,\nu})$  is the Christoffel symbol. As for the right hand side of Eq. 3.5, the energy momentum tensor for perfect fluid is considered in this section to be consistent with observation of the universe. In this case, one can write

$$T_{\mu\nu} = (\rho + p)u_\mu u_\nu + pg_{\mu\nu}, \quad (3.8)$$

where the  $u_\mu$  is the timelike 4-velocity given by

$$u_\mu \equiv \frac{dx_\mu}{d\tau}, \quad (3.9)$$

and  $\rho$  and  $p$  are the energy density and pressure in the rest frame of the fluid, in which the  $u^\mu = (1, 0, 0, 0)$ . Working in the fluid rest frame, the energy momentum tensor reads

$$T^\mu_\nu = \begin{pmatrix} \rho & 0 & 0 & 0 \\ 0 & -p & 0 & 0 \\ 0 & 0 & -p & 0 \\ 0 & 0 & 0 & -p \end{pmatrix}. \quad (3.10)$$

The 0-0 component of the Einstein's equations becomes

$$\left(\frac{\dot{a}}{a}\right)^2 = \frac{1}{3}\rho - \frac{k}{a^2}. \quad (3.11)$$

Using Eq. 3.11, the trace of the Einstein's equations is now

$$\frac{\ddot{a}}{a} = -\frac{1}{6}(\rho + 3p), \quad (3.12)$$

where the dots indicate derivative with respect to time. Eq. (3.11) and (3.12) are called Friedmann equations that can be combined to yield the continuity equation

$$\dot{\rho} + 3H(\rho + p) = 0, \quad (3.13)$$

which can also be derived from  $\nabla_\mu T^{\mu\nu} = 0$ . With the definition of the equation of state

$$w = \frac{p}{\rho}, \quad (3.14)$$

the continuity equation can now be used to express the time evolution of  $a(t)$  and  $\rho(t)$  in

terms of each other. One would get

$$\rho \propto a^{-3(1+w)}, \quad (3.15)$$

and

$$a(t) \propto \begin{cases} t^{2/(3+3w)} & w \neq -1, \\ e^{Ht} & w = -1. \end{cases} \quad (3.16)$$

Generally, matter is used to term non-relativistic fluid with  $w = 0$  while radiation to term relativistic fluid with  $w = \frac{1}{3}$ , corresponding to the two major periods dominated by one of each in conventional Big Bang theory.  $w = -1$  corresponds to a cosmological constant. If the universe contains several particular fluids described by  $\rho_i, p_i, w_i$ , the Friedmann equations Eq. (3.11) and (3.12) can be written as

$$H^2 = \frac{1}{3} \sum_i \rho_i - \frac{k}{a^2}, \quad (3.17)$$

$$\frac{\ddot{a}^2}{a} = -\frac{1}{2} \sum_i \rho_i(1 + 3w_i). \quad (3.18)$$

In order to better analyze the causal structure, the particle horizon is defined to be the maximum distance light can travel, in comoving coordinates, between the big bang time  $t = 0$  and the observing time  $t = t_o$ , which is the light speed multiplied by the conformal time that have passed

$$\tau_{\text{ph}} = \int_0^{t_o} \frac{dt}{a(t)} = \int_0^a \frac{da'}{Ha'^2}. \quad (3.19)$$

In the conventional Big Bang theory,  $w$  is larger than 0 leading to the particle horizon behaving as  $\tau_{\text{ph}} \propto a^{(1+3w)/2}$  and the big bang singularity  $a = 0$  would correspond to conformal time  $\tau = 0$ . Since the scale factor  $a$  is always increasing as the universe expands, the particle horizon has been increasing since the big bang singularity. As mentioned above, the particle horizon indicates the maximum distance light could have traveled, which is also the region that is causally connected to the observer. The comoving scale of the CMB one observes today is much larger than the comoving horizon at the time these photons are

emitted. This is illustrated in Fig. 3.1.

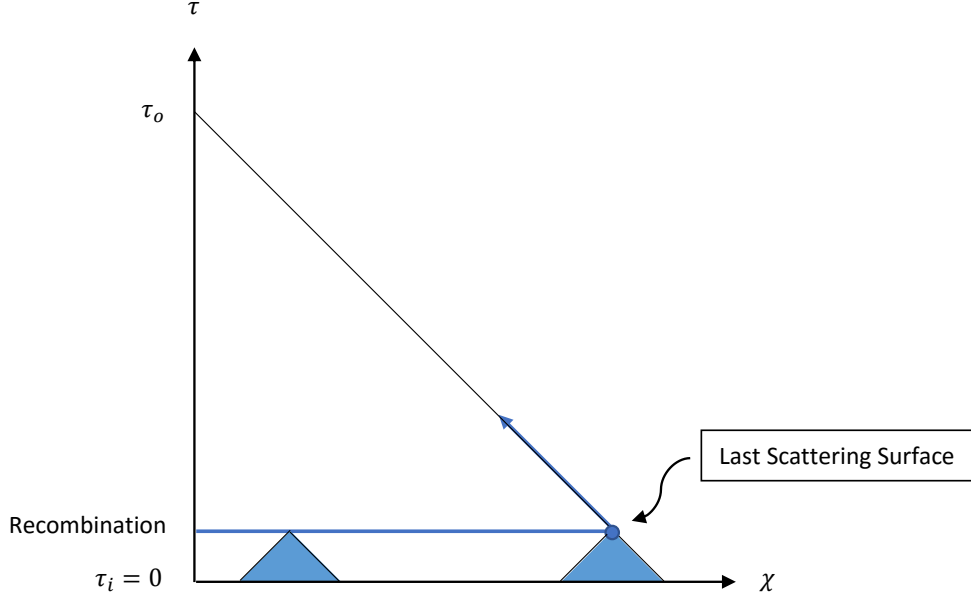


Figure 3.1: Conventional Big Bang cosmology in conformal diagram, the shaded areas are causally connected.

The term recombination in Fig. 3.1 refers to the period when electrons and protons combined into neutral hydrogen and helium. With the transition of ionized plasma to matter, photons are allowed to travel unimpeded. Thus the CMB observed today are actually from the universe in the recombination epoch. It is clear from the plot that the points on the recombination line are not all causally related since the Big Bang singularity, in other words, the CMB contains a number of causally disconnected regions. This conclusion would make it surprising that the CMB is so homogeneous in large scales, if different parts of the background were never in touch with each other. This is called the horizon problem.

Another defect of conventional Big Bang theory is the flatness problem. Eq. (3.12) can be written as

$$\Omega(a) - 1 = \frac{k}{(aH)^2}, \quad (3.20)$$

where  $\Omega(a) \equiv \rho/(3H^2)$  and  $(aH)^{-1}$  is called the comoving Hubble radius. In conventional

cosmology the universe is dominated by either radiation or matter, the comoving Hubble radius is monotonically increasing with  $a$  as  $H_0^{-1}a^{(1+3w)/2}$ . Defining a curvature parameter  $\Omega_k \equiv \Omega - 1$ , one would expect  $\Omega_k$  to increase with time. However, the current  $\Omega_k$  is measured to be less than 0.01, which means it has to be  $\sim 10^{-62}$  at Planck scale!

Strictly speaking, both the horizon problem and the flatness problem are not inconsistencies. One needs fine-tuned initial conditions for the conventional Big Bang theory to work. No one likes fine-tuning, and it will be explained in the next section how inflation solves these problems.

### 3.1.2 Idea of Inflation

From the reasoning in the previous section, it is noticed that a possible solution to the horizon problem is a period that the CMB scale regions were in causal contact at an earlier time, that is, the big bang singularity is pushed back to further negative  $\tau$ . To address this, a comoving Hubble length  $(aH)^{-1}$  is introduced. It appears in the integrand of the definition of conformal time  $\tau$ .

$$\tau = \int \frac{1}{aH} \frac{da}{a}. \quad (3.21)$$

A straightforward realization of large earlier contribution to  $\tau$  is an decreasing comoving Hubble length  $(aH)^{-1}$ . That way, the particle horizon at the epoch of recombination can be large enough to ensure different regions of the CMB were in contact with each other at earlier conformal time and achieved homogeneity then. One can also find that a decreasing comoving Hubble length  $(aH)^{-1}$  is an immediate solution to the flatness problem according to Eq. (3.20). To achieve a decreasing  $(aH)^{-1}$ , since  $a$  is increasing always, a period of nearly constant  $H$  is desirable. This period is then called inflation.

The apparent condition for inflation is

$$\frac{d}{dt} \left( \frac{1}{aH} \right) < 0. \quad (3.22)$$

Eq. (3.22) directly leads to

$$\ddot{a} > 0, \quad (3.23)$$

which means the universe undergoes an accelerated expansion during inflation. From Eq. (3.12), one concludes that during inflation

$$p < -\frac{1}{3}\rho, \quad (3.24)$$

indicating negative pressure during inflation. It is easiest to see how inflation fix the horizon problem in comoving coordinates. With approximately constant  $H$ , the conformal time in terms of  $a$  is

$$\tau = -\frac{1}{aH}. \quad (3.25)$$

The Big Bang singularity is now at  $\tau = -\infty$ , the effect of which is illustrated in Fig. 3.2.

### 3.1.3 Slow-Roll Inflation

The simplest realization of the idea of inflation is through a scalar field called the inflaton. In order to get nearly constant  $H$ , the potential needs to be flat enough so that the potential energy dominates over kinetic energy and the inflaton is said to be slow-rolling during inflation. In the following work, a simplest action for a scalar inflaton field is assumed as follows

$$S = \int d^4x \sqrt{-g} \left( \frac{1}{2}R + \frac{1}{2}g^{\mu\nu}\partial_\mu\phi\partial_\nu\phi - V(\phi) \right), \quad (3.26)$$

where  $g_{\mu\nu}$  is a flat FRW metric. The inflaton field  $\phi$  is usually assumed to be spatially homogeneous. The dynamics of the field is determined by equation of motion

$$\frac{1}{\sqrt{-g}}\partial_\mu(\sqrt{-g}\partial^\mu\phi) + V_{,\phi} = 0, \quad (3.27)$$

which reduces to

$$\ddot{\phi} + 3H\dot{\phi} + V_{,\phi} = 0, \quad (3.28)$$

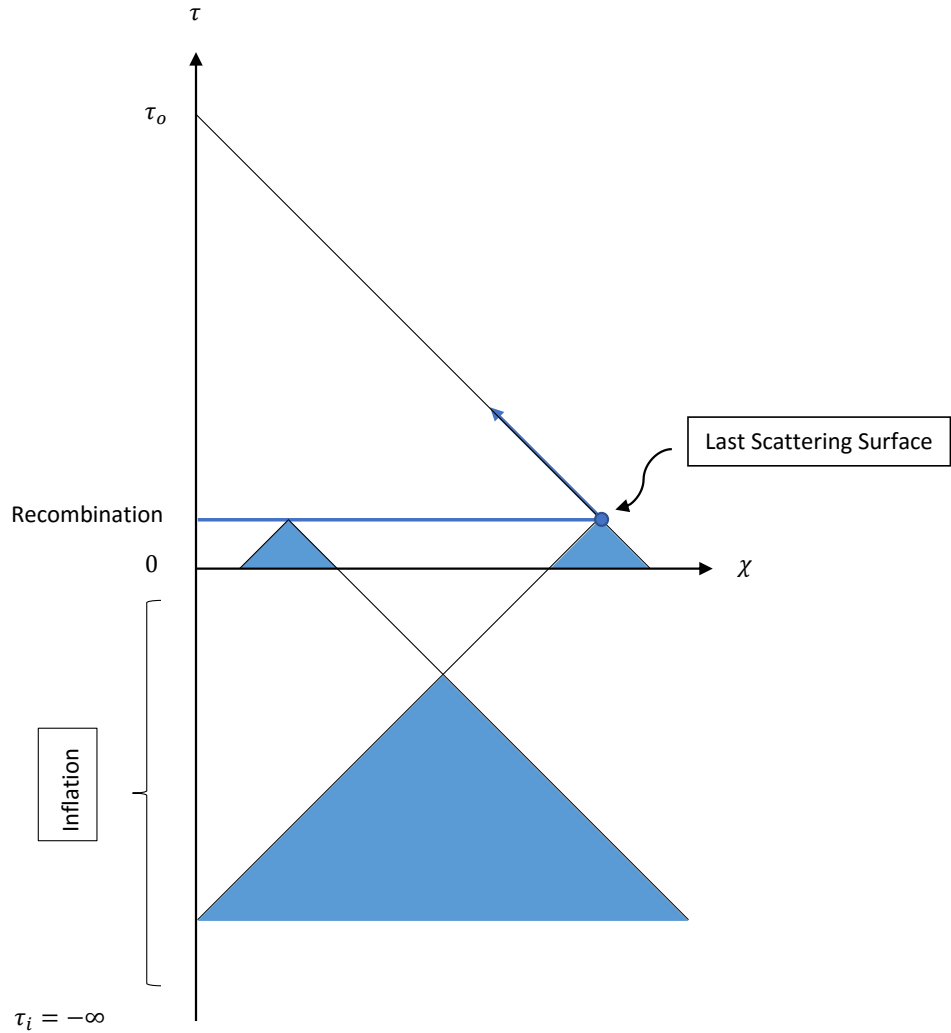


Figure 3.2: Inflation solves the causal problem in conformal diagram, the Big Bang singularity is pushed further down to  $\tau = -\infty$ .

where  $H^2 = (\dot{\phi}^2/2 + V(\phi))/3$ . The energy momentum tensor for the inflaton field is defined by,

$$T_{\mu\nu}(\phi) \equiv -\frac{2}{\sqrt{-g}} \frac{\delta(\sqrt{-g}\mathcal{L}_{\phi\phi})}{\delta g^{\mu\nu}}. \quad (3.29)$$

The energy density and pressure of the inflaton are

$$\rho_\phi = \frac{1}{2}\dot{\phi}^2 + V(\phi), \quad (3.30)$$

$$p_\phi = \frac{1}{2}\dot{\phi}^2 - V(\phi). \quad (3.31)$$

The condition for accelerated expansion  $\ddot{a} > 0$  can be translated to

$$\frac{\ddot{a}}{a} = \dot{H} + H^2 > 0, \quad (3.32)$$

thus

$$\epsilon \equiv -\frac{\dot{H}}{H^2} < 1, \quad (3.33)$$

where  $\epsilon$  is called a slow-roll parameter. Since  $V$  is dominating over  $\dot{\phi}^2$ , one have

$$\epsilon \simeq \epsilon_v \equiv \frac{1}{2} \left( \frac{V'}{V} \right)^2, \quad (3.34)$$

the prime denotes derivative with respect to  $\phi$ . In order for the slow-roll inflation to persist for sufficiently long time to match the observation, one also requires  $\ddot{\phi}$  to be small compared to the other two terms in Eq. (3.28), leading to

$$3H\dot{\phi} \simeq V_{,\phi}, \quad (3.35)$$

defining a second slow-roll parameter  $\eta$ , one requires

$$\eta = -\frac{\ddot{\phi}}{H\dot{\phi}} \ll 1. \quad (3.36)$$

Using Eq. (3.35),  $\eta$  is related to a  $\eta_v$

$$\eta + \epsilon_v \simeq \eta_v \equiv \frac{V''}{V}. \quad (3.37)$$

Practically in these kinds of models, one requires both  $\epsilon_v$  and  $\eta_v \ll 1$  and  $\epsilon_v = 1$  would mark the end of inflation. Before passing onto quantum fluctuations of the inflaton field, the number of  $e$ -folds is introduced, measuring the duration of inflation and in terms of  $a$ , as

$$N_e \equiv \ln \frac{a_f}{a_i} = \int_{t_i}^{t_f} H dt = \int_{\phi_i}^{\phi_f} \frac{H}{\dot{\phi}} d\phi \approx \int_{\phi_f}^{\phi_i} \frac{V}{V'} d\phi. \quad (3.38)$$

Using  $\epsilon_v$ , one gets

$$N_e = \int_{\phi_f}^{\phi_i} \frac{d\phi}{\sqrt{2\epsilon_v}}. \quad (3.39)$$

In the next section, the quantum fluctuation of scalar inflation models are considered and they are related to the anisotropies of CMB and the formation of large scale structure/matter distribution of our universe.

### 3.1.4 Quantum Fluctuations and Large Scale Structure

As mentioned in Sec. 3.1.1, the universe can be considered as a homogeneous and isotropic background with irregularities, *i.e.* CMB anisotropies and matter distributions. The dynamics of the homogeneous universe have been discussed in Sec. 3.1.1 and the inhomogeneous part is studied in this subsection. When discussing perturbations of a physical quantity around its background, the first question one would ask is which part should be considered as the background and which as perturbations. Since the background is homogeneous, it is straightforward to write

$$\Psi(\mathbf{x}, t) \equiv \bar{\Psi}(t) + \delta\Psi(\mathbf{x}, t), \quad (3.40)$$

where  $\Psi$  denotes any physical quantity. One immediately realizes that the definition of perturbations  $\delta\Psi(\mathbf{x}, t)$ , of either matter contents or the geometry, depends on the coordinate system, which is usually called gauge choice. The perturbations of matter field is related to perturbations of the geometry through the Einstein's equations, assuming vanishing

cosmological constant and expanding Eq. (3.5) to linear order

$$\delta G_{\mu\nu} = 8\pi G \delta T_{\mu\nu}. \quad (3.41)$$

Certain combinations of the perturbations are independent of the gauge choice with clear physical meanings. This section focuses on gauge invariant measures of the perturbations important for inflation, and relates them to observations. For a more detailed review, see Refs. [24, 25].

Looking at the inflation action Eq. (3.26), in the comoving gauge where  $\delta\phi = 0$ , one can parametrize the metric such that

$$g_{ij} = a^2[(1 - 2\mathcal{R})\delta_{ij} + h_{ij}]. \quad (3.42)$$

$\mathcal{R}$  is a scalar perturbation and  $h_{ij}$  is a tensor perturbation generating gravitational waves. The other perturbations of the metric are either constrained by the Einstein's equations or are vanishing in this gauge choice. The tensor perturbation is itself gauge-invariant while a gauge-invariant measure of the curvature is given by  $\mathcal{R} + H\delta\phi/\dot{\bar{\phi}}$ , which is just  $\mathcal{R}$  in the comoving gauge. Vector perturbations are not considered here since they decay as the universe expands. These perturbations are created with full spectrum in terms of wave number  $k$ , in other words, the perturbations are of all length scales. As mentioned in previous sections, the period of inflation is characterized by shrinking comoving Hubble length  $(aH)^{-1}$ , making the comoving scale of a perturbation  $1/k$  larger than comoving Hubble horizon at a point called horizon exit. The perturbation would get frozen and remain constant after horizon exit since causal physics does not work outside the horizon. After inflation, the comoving Hubble horizon grows monotonically as predicted by conventional cosmology, the perturbation will eventually enter the horizon again and evolve under standard Big Bang cosmology. Later at the recombination epoch, photons decoupled from the rest of the stuff and started traveling freely. The perturbations would translate to the temperature and polarization distributions of the CMB observed today through Thomas scattering. This is

illustrated in Fig. 3.3.

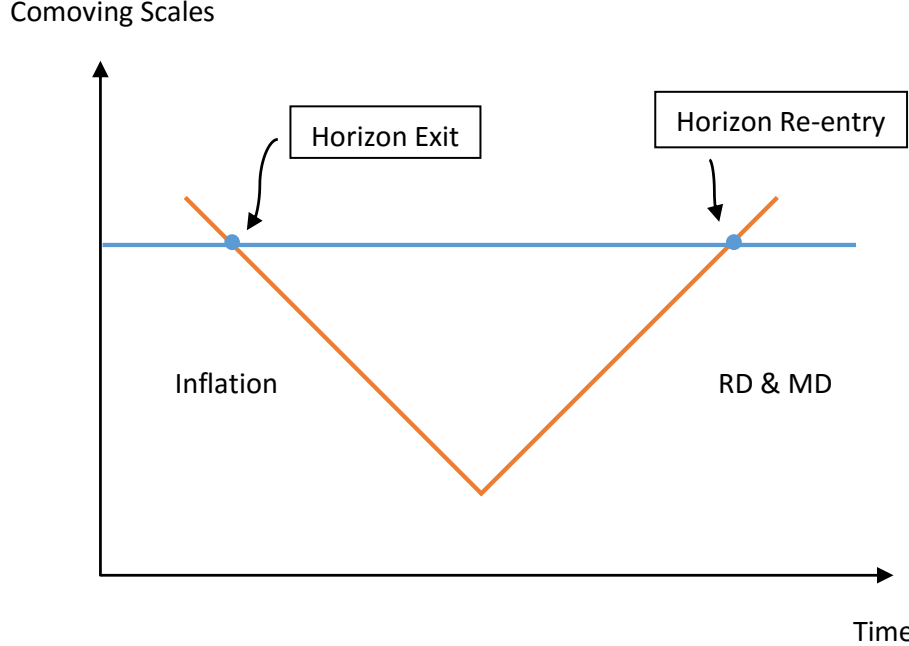


Figure 3.3: The orange line shows the time evolution of the comoving Hubble horizon. The blue line indicates the length scale of a particular quantum fluctuation.

Mathematically, this evolution process can be approximated by a transfer function that relates horizon-exit values of fluctuations to observables today. The calculation of the transfer function is not covered in this dissertation but can be found in [24]. The primordial power spectrum of quantum fluctuations, mainly scalar fluctuations, then can be inferred from the experimentally observed CMB anisotropies and density distributions. Turning back to the inflationary models, these variables  $\mathcal{R}$  and  $h_{ij}$  are essentially quantum fields, the power spectrum is defined as vacuum expectation values. For the scalar fluctuation  $\mathcal{R}$ , the power spectrum  $\Delta_{\mathcal{R}}^2$  is defined

$$\Delta_{\mathcal{R}}^2(k) \equiv \frac{k^3}{2\pi^2} P_{\mathcal{R}}(k), \text{ where } \langle \mathcal{R}_{\mathbf{k}} \mathcal{R}_{\mathbf{k}'} \rangle = (2\pi)^3 \delta(\mathbf{k} + \mathbf{k}') P_{\mathcal{R}}(k). \quad (3.43)$$

As for tensor perturbation  $h_{ij}$ , which has two polarization states  $+$  and  $\times$  as constrained

by the linearized Einstein's equations, its Fourier expansion can be written

$$h_{ij} = \int \frac{d^3 k}{(2\pi)^3} \sum_s \epsilon_{ij}^s(k) h_{\mathbf{k}}^s(\tau) e^{i\mathbf{k}\cdot\mathbf{x}}, \quad (3.44)$$

where the superscript  $s$  denotes polarization states  $+$  and  $\times$ . The power spectrum of tensor fluctuations is

$$\Delta_t^2(k) = 2\Delta_h^2(k) = \frac{k^3}{\pi^2} P_h(k), \text{ where } \langle h_{\mathbf{k}}^s h_{\mathbf{k}'}^{s'} \rangle = (2\pi)^3 \delta(\mathbf{k} + \mathbf{k}') \delta_{ss'} P_h(k). \quad (3.45)$$

Spectral index is defined to measure the  $k$ -dependence of the power spectrum

$$\begin{aligned} n_s &\equiv 1 + \frac{d \ln \Delta_s^2}{d \ln k}, \\ n_t &\equiv \frac{d \ln \Delta_t^2}{d \ln k}. \end{aligned} \quad (3.46)$$

As the tensor fluctuation would produce gravitational waves, the tensor-to-scalar ratio is a good indicator of primordial gravitational waves.

$$r \equiv \frac{\Delta_t^2(k)}{\Delta_{\mathcal{R}}^2(k)}. \quad (3.47)$$

Under slow-roll conditions, these measures can all be expressed with slow-roll parameters and easily calculated from the functional forms of the potential in inflation models. They are given by

$$\begin{aligned} \Delta_{\mathcal{R}}^2(k) &= \frac{1}{24\pi^2} \frac{V}{\epsilon_v}, \\ \Delta_t^2(k) &= \frac{2}{3\pi^2} V, \\ n_s &= 1 + 2\eta_v - 6\epsilon_v, \\ n_t &= -2\epsilon_v, \\ r &= 16\epsilon_v. \end{aligned} \quad (3.48)$$

The RHS are all evaluated at horizon-exit when  $k = aH$  and the perturbations got frozen.

In the case of multi-field inflation, the scalar perturbations can be decomposed to adiabatic perturbation along the inflationary trajectory and entropy perturbations orthogonal to the trajectory. These perturbations will both contribute to the scalar power spectrum and some of the above expressions need to be modified to accommodate them. Determined by the perturbed equations of motion, the entropy perturbations are suppressed by the effective mass squared along the direction they are defined, which is chosen to be large compared to the Hubble scale in the models considered in Chapter 3, enabling us to ignore the entropy perturbations in those models. The tensor perturbations are decoupled from the scalar perturbations at linear order thus the tensor power spectrum remains the same as in single-field theory.

Due to the anisotropies caused by the perturbations, the radiation field is also polarized through Thomas scattering. The anisotropy field, which is a  $2 \times 2$  tensor field, can be decomposed into 3 scalar quantities, the temperature  $T$  and two polarizations  $E$  and  $B$  respectively. The polarization modes  $E$  and  $B$  are defined such that, under parity transformation,  $E$  stays the same while  $B$  changes sign. Thus the  $E/B$  decomposition is also called scalar/pseudo-scalar decomposition. As derived in Ref. [26, 27],  $B$ -polarization can only be produced by tensor fluctuations, making  $B$ -modes polarization a direct indicator of primordial gravitational wave and inflation. Recall from previous section Eq. (3.39), using  $r = 16\epsilon_v$ , one gets

$$\frac{d\phi}{dN} = \sqrt{\frac{r}{8}}. \quad (3.49)$$

Assuming the slow-roll conditions hold for most of the inflationary process thus  $r$ , as a function of  $N$ , does not change much. For 60  $e$ -folds

$$\Delta\phi = C(1) \sqrt{\frac{r}{0.01}}, \quad (3.50)$$

where  $C(1)$  is a constant of order 1 and  $\Delta\phi$  is in the unit of reduced Planck mass. However, observably large  $B$ -modes require a tensor-to-scalar ratio to be larger than 0.01 according

to the sensitivity of PIPER [28], setting the energy scale of inflation to be as high as Planck scale, which makes the effective inflation model invalid. This is called the Lyth bound. There are various methods to evade the Lyth bound and have models able to accommodate large  $B$ -mode signals. One approach is to use a two-field axion-monodromy model with one of the fields retaining a discrete shift symmetry. In this chapter, several such models are researched and the effect of adding a field space metric is analyzed.

## 3.2 Dante’s Waterfall

### 3.2.1 Introduction

The  $B$ -modes in the polarization of the cosmic microwave background (CMB) reported by the BICEP2 collaboration [29] may be due to primordial gravitational waves [30, 31], or may be due to conventional polarization-dependent processes such as scattering off of galactic dust [32, 33], as suggested by recent measurements by the Planck collaboration [34]. Tensor modes in primordial gravitational waves could produce an observably large  $B$ -mode polarization signal if the scale of inflation is high enough, typically around the GUT scale. However, the Lyth bound [35] implies that generically in such scenarios, the inflaton varies over a super-Planckian range of field values during inflation. This would render an effective field theory treatment invalid, so possibilities for evading the Lyth bound are of practical interest. One possibility is that the slow-roll parameter  $\epsilon$  varies by a large multiplicative factor during inflation, which renders the Lyth-bound analysis invalid [36, 37]. Another possibility is that the inflaton is an axion with an associated shift symmetry. In such a scenario, super-Planckian values of the inflaton field are identified with sub-Planckian values plus additional fluxes of one or more other fields [38]. These axion-monodromy models provide a framework consistent with effective field theory which could accommodate an observably large amplitude in tensor modes.

A simplified scenario incorporating the axion-monodromy idea, improving on inflation models with two axions [39], is known as Dante’s Inferno [40]. The two axions of the Dante’s

Inferno model play different roles: one has an explicitly broken shift symmetry while the other maintains a discrete shift symmetry. The periodic nature of the two-field potential gives rise to a trench that extends down to the minimum of the potential. The inflaton field is identified with the linear combination of fields that slowly rolls down the trench, and can wind many times during inflation while neither of the two fields ever takes super-Planckian values. Hence, this model is amenable to an effective-field-theory treatment even if significant power in tensor modes is produced during inflation. The inflationary dynamics in the Dante's Inferno scenario is controlled by the shape of the potential along the one-dimensional trench, and the scenario makes the same predictions as a single-field chaotic inflation model. The Lagrangian for the two fields,  $r$  and  $\theta$ , in the Dante's Inferno model is given by [40]

$$\mathcal{L} = \frac{1}{2}(\partial_\mu r)^2 + \frac{1}{2}(\partial_\mu \theta)^2 - V(r, \theta) , \quad (3.51)$$

where the potential  $V(r, \theta)$  respects the discrete shift symmetry in  $\theta$  and the broken shift symmetry in  $r$ :

$$V(r, \theta) = W(r) + \Lambda^4 \left[ 1 - \cos \left( \frac{r}{f_r} - \frac{\theta}{f_\theta} \right) \right] . \quad (3.52)$$

The potential  $W(r)$  explicitly breaks the shift symmetry of the field  $r$ , which in a string theory realization could be due to nonperturbative effects related to moduli stabilization [40]. Assuming  $W(r) = \frac{1}{2}m^2r^2$ , the cosine term in  $V(r, \theta)$  gives rise to a staircase-like trench in the potential, as shown in Fig. 3.4, where the coordinate  $\theta$  is wrapped in cylindrical coordinates to reflect the shift symmetry. With this choice of  $W(r)$ , the inflaton accelerates along the trench, both before and for some time after the end inflation, with the transition occurring when the slow roll conditions (*e.g.*  $\epsilon < 1$ ) are violated. The dynamics of the inflaton field can be described by an effective one-dimensional inflaton potential that is quadratic [40], so that the predictions for inflationary observables are identical to those of an analogous chaotic inflation model [41]. In particular, the scenario allows for relatively large power in tensor modes, with ratio of tensor to scalar amplitudes  $r = 0.14$ .

We present a variation of the Dante's Inferno scenario in which the inflaton trench

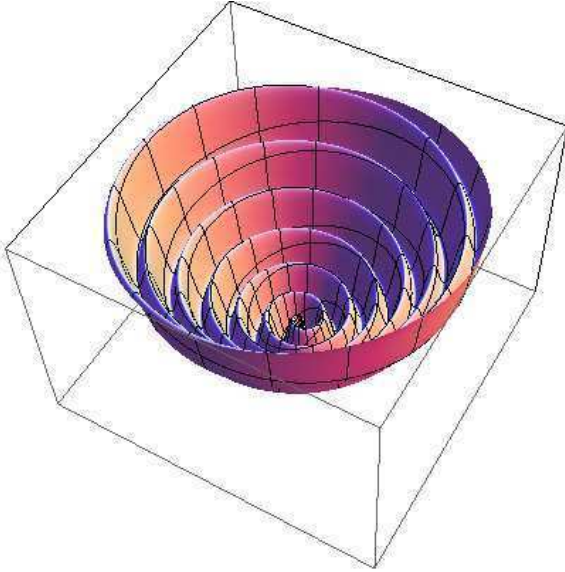


Figure 3.4: The potential as a function of  $r$  and  $\theta$  in Dante’s Inferno with a quadratic shift-symmetry-breaking potential, as in Ref. [40]. The field  $\theta$  is represented in cylindrical coordinates with period  $2\pi f_\theta$ .

becomes unstable for a range of inflaton field values. In this scenario, the slow-roll conditions break down only after the inflaton rolls off the trench and begins moving rapidly in an independent direction in field space. Thus, inflation ends as in a hybrid model. In hybrid inflation, the waterfall field has an effective squared mass that depends on the inflaton field value. At a critical point, this squared mass becomes negative and the system rapidly evolves to its global minimum. In our scenario, the same is true for a linear combination of the fields  $r$  and  $\theta$ : one linear combination is identified as the inflaton and the effective squared mass of the remaining combination depends on the inflaton field value. When this squared mass becomes negative, the combination of fields that rolls quickly towards the potential minimum (and then oscillates about it) acts as the waterfall field of hybrid inflation [42]. Hence, we refer to this scenario as Dante’s Waterfall. The model has the same Lagrangian as the Dante’s Inferno model, Eqs. (3.51)-(3.52), but with a symmetry-breaking potential

$$W(r) = -\frac{1}{2}m^2r^2 + \frac{\lambda}{4!}r^4 + \frac{3}{2}\frac{m^4}{\lambda}. \quad (3.53)$$

An inflation model with a similar symmetry-breaking potential has been considered recently

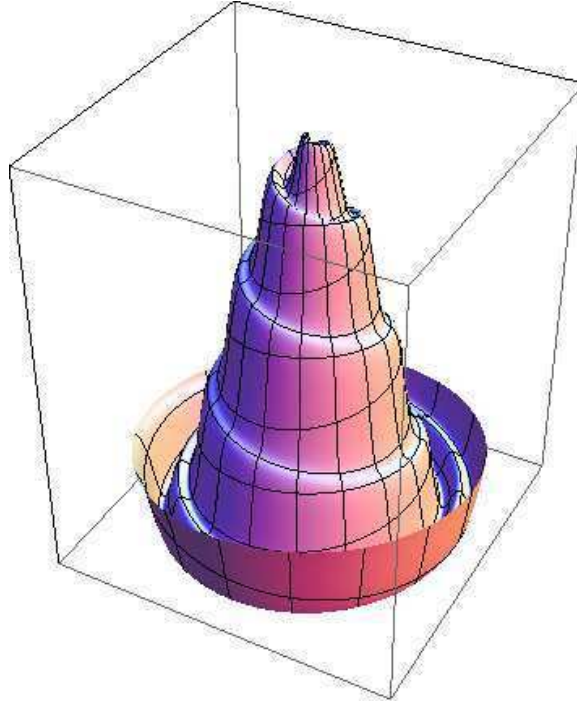


Figure 3.5: The potential as a function of  $r$  and  $\theta$  in Dante’s Waterfall, with symmetry-breaking potential  $W(r)$  as in Eq. (3.53). The field  $\theta$  is represented in cylindrical coordinates with period  $2\pi f_\theta$ .

in Ref. [43, 44]. The last term in Eq. (3.53) is included so that the full potential  $V(r, \theta)$  vanishes at its global minimum. This is the usual fine-tuning of the cosmological constant. With this form for  $W(r)$ , the potential  $V(r, \theta)$  is as in Fig. 3.5. In the typical Dante’s Inferno scenario, the trench is unstable only for large field values not relevant during inflation. However, in the present scenario, depending on the choice of model parameters, it is possible for the trench to become unstable for a range of intermediate field values. This is the scenario we consider here. We analyze cosmological observables analytically under certain assumptions in Sec. 3.2.2, and more generally in Sec. 3.2.3. We conclude in Sec. 3.2.4.

### 3.2.2 Single-Field Effective Theory

By a field rotation the potential, Eqs. (3.52)-(3.53), can be written

$$V = -\frac{1}{2}m^2r^2 + \frac{\lambda}{4!}r^4 + \frac{3}{2}\frac{m^4}{\lambda} + \Lambda^4[1 - \cos(\tilde{r}/f)] , \quad (3.54)$$

where  $r = c\tilde{r} + s\tilde{\theta}$ ,  $\theta = c\tilde{\theta} - s\tilde{r}$ , and  $s \equiv \sin \xi$ ,  $c \equiv \cos \xi$  define the field rotation. In terms of the parameters in Eqs. (3.52)-(3.53),

$$\sin \xi = \frac{f_r}{\sqrt{f_r^2 + f_\theta^2}}, \quad \cos \xi = \frac{f_\theta}{\sqrt{f_r^2 + f_\theta^2}}, \quad \text{and} \quad f = \frac{f_r f_\theta}{\sqrt{f_r^2 + f_\theta^2}}. \quad (3.55)$$

We assume for most of our analysis that  $\sin \xi \ll 1$ , or equivalently,  $f_r \ll f_\theta$ . The trench in field space is given by  $\partial V(\tilde{r}, \tilde{\theta})/\partial \tilde{r} = 0$ , or

$$-m^2 c r + \frac{\lambda}{6} c r^3 + \frac{\Lambda^4}{f} \sin(\tilde{r}/f) = 0. \quad (3.56)$$

This equation has been expressed in terms of  $r$  and  $\tilde{r} = c r - s \theta$  such that it is in a notationally compact form and easier comparing with Ref. [40] where the same mixed notation was used. The bottom of the trench defines an effective one-dimensional potential along which the inflaton field slowly rolls. During inflation, motion continues along the trench provided the stability condition  $\partial^2 V(\tilde{r}, \tilde{\theta})/\partial \tilde{r}^2 > 0$  is satisfied. The end of inflation happens where Eq. (3.131) where  $\partial^2 V/\partial \tilde{r}^2 = 0$  is satisfied, or equivalently

$$-m^2 c^2 + \frac{\lambda}{2} c^2 r^2 + \frac{\Lambda^4}{f^2} \cos(\tilde{r}/f) = 0. \quad (3.57)$$

As we will see, the fields then rapidly deviate from their original trajectory and approach the global minimum of the potential.

As in the model of Ref. [40], there are certain limits of our model where inflation can be described by the evolution of a single field with canonically normalized kinetic terms. The inflaton is approximated by as the linear combination of the fields along the bottom of the trench given by Eq. (3.131). Assume one is in a field region where

$$|c f(m^2 r - \lambda r^3/6)|/\Lambda^4 \ll 1, \quad (3.58)$$

which allows one to approximate  $\sin(\tilde{r}/f) \approx \tilde{r}/f$ . And one chooses

$$s c f^2 m^2 / \Lambda^4 \ll 1 , \quad (3.59)$$

such that the trench equation Eq. (3.131) reduces to a linear relationship between  $\tilde{r}$  and  $\tilde{\theta}$ :

$$\tilde{r} = \left[ \frac{f^2 m^2 s c}{\Lambda^4 - f^2 m^2 c^2} \right] \tilde{\theta} \approx s c \left( \frac{f^2 m^2}{\Lambda^4} \right) \tilde{\theta} . \quad (3.60)$$

This way, inflation happens mostly in the  $\tilde{\theta}$  direction thus  $\tilde{\theta} \equiv \phi$  is identified as the inflaton in the single-field effective description. Eq. (3.59) assures that the inflaton kinetic terms are canonical, up to small corrections of order  $(s c m^2 f^2 / \Lambda^4)^2$ . We will make the further simplifying assumption in what follows that both  $s \ll 1$  and  $f^2 m^2 / \Lambda^4 \ll 1$ .

Eliminating  $\tilde{r}(\tilde{\theta})$  from Eq. (3.54) using Eq. (3.60), one obtains the effective single-field inflaton potential

$$V_{\text{eff}} = -\frac{1}{2} m_{\text{eff}}^2 \phi^2 + V_0 , \quad (3.61)$$

where

$$m_{\text{eff}} \equiv m s , \quad V_0 \equiv \frac{3}{2\lambda} m^4 , \quad \text{and} \quad \phi \equiv \tilde{\theta} . \quad (3.62)$$

In the case where  $f_r \ll f_\theta$ ,  $s \approx f_r/f_\theta$  and  $m_{\text{eff}} = m f_r/f_\theta$ , as in the model of Ref. [40].

Now we can use this effective description to look for a viable point in model parameter space. One should keep in mind that such solutions are approximate since the assumptions that justify the single-field approximation will generally fail somewhere near the end of the trajectory in field space, the point where the waterfall occurs, as determined by Eq. (3.57), rendering the calculated number of  $e$ -folds of inflation deviating from its counterpart in the two-field complete theory, which we aim to hold fixed between 50 and 60. However, since most of inflation occurs on the earlier part of the trajectory where the single-field approximation is valid, our solutions should be qualitatively trustworthy, as we check in Sec. 3.2.3. This is not very different from the case in non-hybrid inflation models, where one computes the number of  $e$ -folds by first declaring that the end of inflation corresponds

to the value of the slow-roll parameter  $\epsilon = 1$ . Here, we define the end of inflation as  $\phi_f = \tilde{\theta}_f$ , where  $(\tilde{r}_f, \tilde{\theta}_f)$  lies on a trench and satisfies  $\partial^2 V / \partial \tilde{r}^2 = 0$ .

We define an acceptable solution for the effective theory by requiring the calculated spectral index  $n_s$  and the amplitude of the scalar perturbations  $\Delta_R^2$  matching their experimentally measured values. For definiteness, we assume the experimental central values [45]. We first define the slow-roll parameters

$$\epsilon \equiv \frac{M_P^2}{16\pi} \left( \frac{V'}{V} \right)^2, \quad \eta \equiv \frac{M_P^2}{8\pi} \frac{V''}{V}, \quad \gamma \equiv \frac{M_P^4}{64\pi^2} \frac{V' V'''}{V^2}, \quad (3.63)$$

where  $M_P$  is the Planck mass and the primes indicate derivatives of the potential with respect to  $\phi$ . In general, it follows from Eq. (3.61) that  $\gamma = 0$  for our model, and the other two are given by

$$\epsilon = \frac{M_P^2}{4\pi} \frac{\phi^2}{(2V_0/m_{\text{eff}}^2 - \phi^2)^2} \quad \text{and} \quad \eta = -\frac{M_P^2}{4\pi} \frac{1}{(2V_0/m_{\text{eff}}^2 - \phi^2)}. \quad (3.64)$$

The spectral index  $n_s$  and scalar amplitude  $\Delta_R^2$  may be expressed as

$$n_s = [1 - 6\epsilon + 2\eta]_{\phi=\phi_i}, \quad (3.65)$$

$$\Delta_R^2 = \left[ \frac{8}{3M_P^4} \frac{V}{\epsilon} \right]_{\phi=\phi_i} \quad (3.66)$$

where  $\phi_i$  is the value of the inflaton field 50-60  $e$ -folds before the end of inflation, when the largest distance scales that are currently observable exited the horizon. Using Eq. (3.64) one finds

$$n_s = 1 - \frac{M_P^2}{4\pi} \left[ \frac{6\phi_i^2}{(2V_0/m_{\text{eff}}^2 - \phi_i^2)^2} + \frac{2}{(2V_0/m_{\text{eff}}^2 - \phi_i^2)} \right], \quad (3.67)$$

$$\Delta_R^2 = \frac{16\pi}{3M_P^6} \frac{m_{\text{eff}}^2}{\phi_i^2} \left[ \frac{2V_0}{m_{\text{eff}}^2} - \phi_i^2 \right]^3. \quad (3.68)$$

Our formulae assume  $2V_0/m_{\text{eff}}^2 - \phi_i^2 > 0$ , which is consistent with our numerical results. We work henceforth in units where  $M_P = 1$ .

Fixing  $n_s = 0.9603$  and  $\Delta_R^2 = 2.2 \times 10^{-9}$  [45] and varying  $m_{\text{eff}}$ , we find that Eqs. (3.67)

and (3.68) only have solutions if  $m_{\text{eff}} \lesssim 8.31 \times 10^{-7}$ . For example, the choice  $m_{\text{eff}} = 1.2 \times 10^{-7}$  yields

$$V_0 = 2.885 \times 10^{-14} \quad \text{and} \quad \phi_i = 0.0838 . \quad (3.69)$$

We can now check whether there is an acceptable trajectory in the full theory starting from  $\tilde{\theta} = \phi_i$ , and terminating at a point where  $d^2V/d\tilde{r}^2 = 0$  such that 50 to 60  $e$ -folds of inflation is obtained. Fixing  $m_{\text{eff}}$  and  $V_0$  allows us to constrain two degrees of freedom in the parameter space of the complete theory. We choose the value of  $s$  and fix

$$m = m_{\text{eff}}/s \quad (3.70)$$

and

$$\lambda = \frac{3}{2} \frac{m_{\text{eff}}^4}{s^4} \frac{1}{V_0} . \quad (3.71)$$

Specifying  $\Lambda$  and  $f$  then completely determines Eq. (3.54). Consider the following choice of parameters, that are consistent with Eqs. (3.69), (3.70) and (3.71):

$$\begin{aligned} s &= 0.0010 , \\ \lambda &= 1.078 \times 10^{-2} , \\ \Lambda &= 0.0001 , \\ m &= 0.00012 , \\ f &= 2.453 \times 10^{-5} . \end{aligned} \quad (3.72)$$

One can verify that the following points in field space are continuously connected by a solution to Eq. (3.131)

$$\begin{aligned} (\tilde{r}, \tilde{\theta})_i &= (8.099 \times 10^{-6}, 8.377 \times 10^{-2}) , \\ (\tilde{r}, \tilde{\theta})_f &= (3.647 \times 10^{-5}, 2.485 \times 10^{-1}) . \end{aligned} \quad (3.73)$$

In addition,  $(\tilde{r}, \tilde{\theta})_f$  satisfies Eq. (3.57). Identifying  $\phi_f = \tilde{\theta}_f$ , one can now evaluate the

number of  $e$ -folds,

$$N = \frac{2\sqrt{\pi}}{M_P} \int_{\phi_i}^{\phi_f} \frac{1}{\sqrt{\epsilon}} d\phi \quad (3.74)$$

$$= \frac{4\pi}{M_P^2} \left[ \frac{2V_0}{m_{\text{eff}}^2} \ln(\phi_f/\phi_i) - \frac{1}{2}(\phi_f^2 - \phi_i^2) \right] , \quad (3.75)$$

from which one obtains  $N = 54.4$ .

The remaining cosmological parameters of interest can be expressed in terms of the slow-roll parameters. The ratio of tensor-to-scalar amplitudes is presented by  $\underline{r}$  (to distinguish it from the field  $r$ ), which is given by

$$\underline{r} = [16\epsilon]_{\phi=\phi_i} , \quad (3.76)$$

and the running of the spectral index by

$$n_r = [16\epsilon\eta - 24\epsilon^2 - 2\gamma]_{\phi=\phi_i} . \quad (3.77)$$

In the present example, one finds

$$\begin{aligned} \underline{r} &= 5.585 \times 10^{-4} , \\ n_r &= -1.114 \times 10^{-5} . \end{aligned} \quad (3.78)$$

These are consistent with current bounds [45], given the lingering questions surrounding the current BICEP2 measurement of  $\underline{r}$ . We will discuss larger possible values of  $\underline{r}$  later in this section.

To estimate the validity of the effective description, it is worth checking, to what extent the two conditions Eq. (3.59) and Eq. (3.58) hold along the inflationary trajectory for the above solution. The left-hand-side of Eq. (3.59) evolves from 0.324 to 0.996 during inflation while that of Eq. (3.58) be  $8.7 \times 10^{-5}$  indifferent of position in field space. The first condition breaks down at the end of inflation as expected.

To better visualize the solution, we first note that in the original  $(r, \theta)$  coordinate system, the global minimum is located at

$$r_{min} = \sqrt{\frac{6}{\lambda}}m = 2.831 \times 10^{-3} , \quad (3.79)$$

while the initial and final  $r$  values are

$$\begin{aligned} r_i &= 9.187 \times 10^{-5} \\ r_f &= 2.850 \times 10^{-4} . \end{aligned} \quad (3.80)$$

The trajectory in this example is far from the global minimum at positive  $r$  and moving toward it, as one might expect. A plot of the trajectory in  $\tilde{r} - \tilde{\theta}$  space during inflation is shown in Fig. 3.6.

One can confirm the end of inflation in this example by studying the time evolution of the fields in the full theory,  $\tilde{r}(t)$  and  $\tilde{\theta}(t)$ , which satisfy the coupled equations of motion

$$\begin{aligned} \ddot{\tilde{r}} + 3H\dot{\tilde{r}} + \frac{\partial V}{\partial \tilde{r}} &= 0 , \\ \ddot{\tilde{\theta}} + 3H\dot{\tilde{\theta}} + \frac{\partial V}{\partial \tilde{\theta}} &= 0 . \end{aligned} \quad (3.81)$$

For definiteness, we assume the following boundary conditions

$$\begin{aligned} \tilde{r}(0) &= \tilde{r}_i & \dot{\tilde{r}}(0) &= 0 , \\ \tilde{\theta}(0) &= \tilde{\theta}_i & \dot{\tilde{\theta}}(0) &= 0 , \end{aligned} \quad (3.82)$$

while qualitatively similar solutions are obtained for other choices as long as the slow-roll conditions are satisfied. The results are shown in Fig. 3.7, with the time variable  $t_r = H_0 t$  where  $H_0 \equiv H(t = 0)$  is the Hubble parameter at the beginning of inflation. Notice that  $\tilde{\theta}(t_r)$  pauses for a brief interval near  $\tilde{\theta}_f$  (around  $t_r \approx 50$ ), at precisely the same time that  $\tilde{r}(t_r)$  rapidly increases away from  $\tilde{r}_f$ : this is the waterfall. The fields then oscillate as they

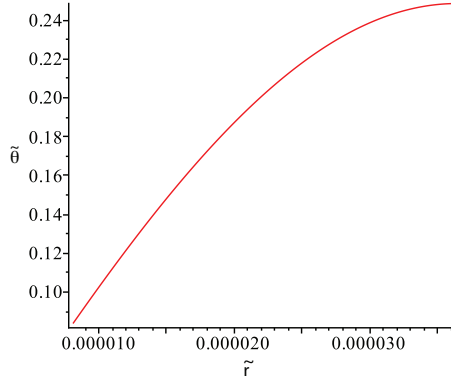


Figure 3.6: Trajectory in field space,  $\tilde{\theta}(\tilde{r})$ , during inflation.

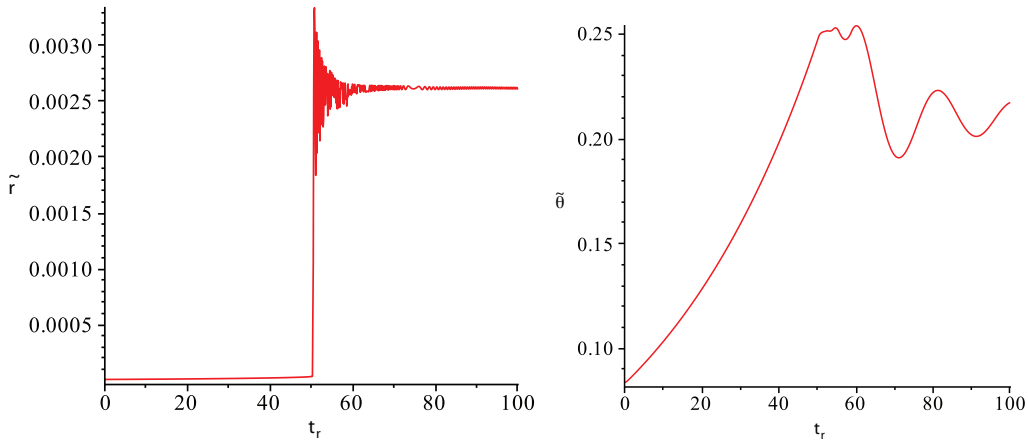


Figure 3.7: Time-evolution of the fields: (a)  $\tilde{r}(t)$ , (b)  $\tilde{\theta}(t)$ . The time is in units of the inverse Hubble parameter at the beginning of inflation and the Planck mass has been set to one.

approach the global minimum, the period when reheating presumably occurs.

The example we have presented is useful in illustrating the qualitative features of a typical solution. Originally motivated by the BICEP2 result, we now investigate whether our model can accommodate solutions with larger values of  $\underline{r}$ , *i.e.* larger tensor perturbations. Given the constraints of Eqs. (3.67) and (3.68), specification of  $m_{\text{eff}}$  determines  $\phi_i$  and hence also the parameter  $\underline{r}$  in our effective theory. It follows that

$$\underline{r}(m_{\text{eff}}) = \frac{2}{9\pi C_0^2} \left[ C_1 \pm (C_1^2 - 4 C_0 m_{\text{eff}}^2)^{1/2} \right] , \quad (3.83)$$

where

$$C_0 = [\Delta_R^2/(144\pi)]^{1/3} \quad \text{and} \quad C_1 = 6\pi C_0^2 (1 - n_s) . \quad (3.84)$$

Numerically,  $C_0 = 1.694 \times 10^{-4}$  and  $C_1 = 2.164 \times 10^{-8}$ . For these values, Eq. (3.83) is maximized when  $\underline{r}_{\max+} = 0.107$  or  $\underline{r}_{\max-} = 0.053$ , depending on the sign of the square root, which corresponds to different possible solutions for  $\phi_i$ . We can make further progress by imposing constraint on the number of  $e$ -folds, given in Eq. (3.75). As a function of  $\phi_f$ , this expression is maximized when  $\phi_f^2 = 2V_0/m_{\text{eff}}^2$ . The value at the maximum,  $N_{\max}$ , is thus a function of  $m_{\text{eff}}$ , like  $\underline{r}$ , and depends on the same sign choice appearing in Eq. (3.83). We find that for the positive square root,  $N_{\max}$  is below 42.4 for any  $m_{\text{eff}}$ ; hence, these solutions are excluded. For the negative square root,  $N_{\max}$  falls below the desired range, 50 to 60, before  $m_{\text{eff}}$  is large enough to yield  $\underline{r}_{\max-} = 0.053$ . We find numerically that  $N > 50$  forces  $\underline{r} < 0.03$ . Hence, we expect on general grounds that

$$\underline{r} < 0.03 , \quad (3.85)$$

provided that Eq. (3.61) is an accurate effective description of the theory. Whether a choice of parameters and field trajectory exists in the complete theory for which this bound is saturated is not guaranteed. However, it is not hard to discover solutions that are of order this bound. Following the approach of this section, one can check, for example, that the parameter choice

$$\begin{aligned} s &= 0.01 , \\ \lambda &= 1.635 \times 10^{-5} , \\ \Lambda &= 5.0 \times 10^{-5} , \\ m &= 5.0 \times 10^{-5} , \\ f &= 2.610 \times 10^{-7} , \end{aligned} \quad (3.86)$$

is consistent with the trajectory

$$\begin{aligned} (\tilde{r}, \tilde{\theta})_i &= (1.120 \times 10^{-7}, 0.406) , \\ (\tilde{r}, \tilde{\theta})_f &= (4.099 \times 10^{-7}, 1.105) . \end{aligned} \quad (3.87)$$

This leads to the values  $\underline{r} = 0.011$  and  $N = 51.1$

### 3.2.3 Numerical Analysis

In the previous section we obtained an approximation for the shape of the one-dimensional potential, Eq. (3.61), which followed from the linear relation in Eq. (3.60). This relation breaks down before the end of inflation. In this section, we find the shape of the trench and compute observables numerically, allowing us to test the validity of our previous approximation.

We again choose  $f_r \ll f_\theta$  and identify  $\tilde{\theta}$  as the inflaton field. Along the trench, Eq. (3.131),  $\tilde{r}$  is non-dynamical to lowest order in  $f_r/f_\theta$  and corrections to the  $\tilde{\theta}$  kinetic terms are negligible. This can be verified by differentiating Eq. (3.131), which yields

$$\frac{\dot{\tilde{r}}}{\dot{\tilde{\theta}}} = \frac{sc f^2 (m^2 - \frac{1}{2}\lambda r^2)}{\Lambda^4 \cos(\tilde{r}/f) - c^2 f^2 (m^2 - \frac{1}{2}\lambda r^2)} . \quad (3.88)$$

In the region of field space where  $m^2 > \frac{1}{2}\lambda r^2$ , as long as

$$\frac{\Lambda^4 \cos(\tilde{r}/f)}{f^2} \geq c^2 (2m^2 - \lambda r^2) , \quad (3.89)$$

the kinetic terms for  $\tilde{r}$  and  $\tilde{\theta}$  sum to

$$\frac{1}{2}\dot{\tilde{r}}^2 + \frac{1}{2}\dot{\tilde{\theta}}^2 \leq (1 + \tan^2 \xi) \frac{1}{2}\dot{\tilde{\theta}}^2 . \quad (3.90)$$

In this case, the  $\tilde{\theta}$  kinetic terms remain canonically normalized to leading order in  $f_r/f_\theta$ .

The potential of the effective single-field description of the theory is given by

$$V(\tilde{\theta}) \equiv V(\tilde{r}_t(\tilde{\theta}), \tilde{\theta}) , \quad (3.91)$$

where  $\tilde{r}_t(\tilde{\theta})$  is the solution to the trench equation Eq. (3.131). Derivatives of Eq. (3.91) with respect to  $\tilde{\theta}$  can be computed numerically to obtain the slow-roll parameters and the inflationary observables discussed in Sec. 3.2.2.

To test the accuracy of the quadratic form of the effective single-field potential, Eq. (3.61), we evaluate observables following from Eq. (3.91) using the same parameters, Eqs. (3.72) and (3.73). Following from Eqs. (3.65), (3.66), (3.76) and (3.77), we find that  $(n_s, \Delta_R^2, \underline{r}, n_r) = (0.956, 1.833 \times 10^{-9}, 6.70 \times 10^{-4}, -1.47 \times 10^{-5})$ . The number of  $e$ -folds is determined by Eq. (3.74), from which we obtain  $N = 49.44$ , somewhat smaller than the value  $N = 54.4$  that followed from the approximations of Sec. 3.2.2. This exercise confirms that the approximation scheme of Sec. 3.2.2 provides a qualitatively accurate solution for the set of cosmological quantities of interest: the breakdown in this scheme occurs close enough to the end of the inflationary trajectory that it does not substantially alter the qualitative results.

In the current numerical treatment, however, we can now find solutions that more exactly match the cosmological observables. For example, with  $(f/s, f/c, m, \lambda, \Lambda) = (0.1043, 3.127 \times 10^{-4}, 1.367 \times 10^{-4}, 1.314 \times 10^{-3}, 3.654 \times 10^{-4})$ ,  $(\tilde{r}_i, \tilde{\theta}_i) = (1.112 \times 10^{-4}, 0.322)$  and  $(\tilde{r}_f, \tilde{\theta}_f) = (4.738 \times 10^{-4}, 1.039)$ , we obtain

$$\begin{aligned} n_s &= 0.960 , \\ \Delta_R^2 &= 2.23 \times 10^{-9} , \\ \underline{r} &= 7.45 \times 10^{-3} , \\ n_r &= -1.42 \times 10^{-4} , \\ N &= 59.7 . \end{aligned} \quad (3.92)$$

As with our previous solution, we may solve the coupled equations of motion for  $\tilde{r}(t)$  and  $\tilde{\theta}(t)$ , with  $\tilde{r}(0) = \tilde{r}_i$  and  $\tilde{\theta}(0) = \tilde{\theta}_i$ . For definiteness, we again assume that the first time

derivatives of the fields vanish at  $t = 0$ , as discussed after Eq. (3.189). The trajectory in field space is shown in Fig. 3.8, while  $\tilde{r}(t)$  and  $\tilde{\theta}(t)$  are shown in Fig. 3.9. We can see that the system rolls along the trench until the instability is reached where inflation ends. The system then moves quickly towards the global minimum of the potential. We have checked that  $\dot{\tilde{r}}(t)^2/\dot{\tilde{\theta}}(t)^2$  remains small along the portion of this trajectory where inflation occurs, never exceeding  $10^{-7}$ , so that the classical wavefunction renormalization of the inflaton field is negligible.

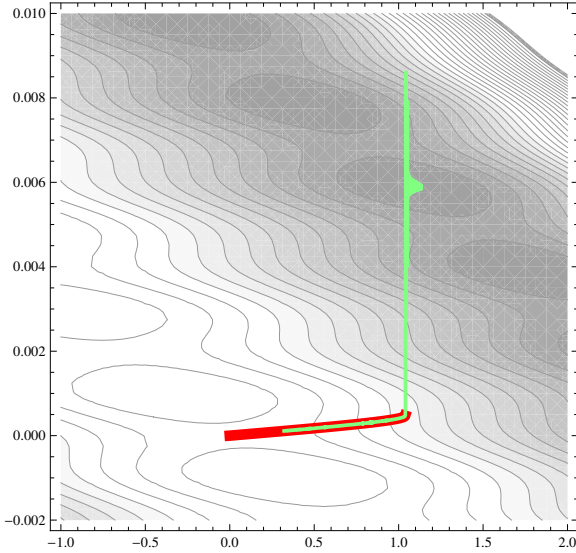


Figure 3.8: Contour plot of the potential in terms of  $\tilde{r}$  (vertical axis) and  $\tilde{\theta}$  (horizontal axis). The thick, solid red line indicates the bottom of the trench. The inflationary trajectory is shown by the thin green line.

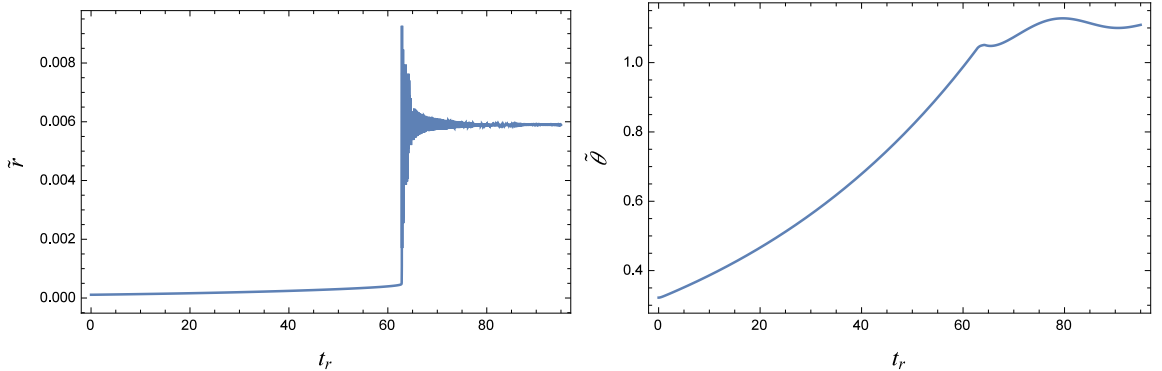


Figure 3.9: Dynamic solutions. The left graph shows  $\tilde{r}(t_r)$  and the right graph shows  $\tilde{\theta}(t_r)$ . The time variable  $t_r = H_0 t$  is scaled in units of Hubble time at the beginning of inflation.

### 3.2.4 Comments

We have studied a new realization of hybrid inflation in a variant of an axion monodromy model known as Dante’s Inferno [40]. By altering the assumed form of the shift-symmetry-breaking potential of one of the axion fields, the scalar potential in our model takes the form of a Mexican hat with an indentation, or trench, spiraling down from its peak. Inflation corresponds to slowly rolling down this trench until a point where the trench becomes shallow and can no longer support the motion; the system then evolves rapidly in the radial direction towards the global minimum of the potential. After formulating an appropriate single-field approximation for the period of inflation, we studied viable points in model parameter space where the amplitude of scalar perturbations, the spectral index, the running of the spectral index, and the number of  $e$ -folds of inflation are consistent with observational data. In an approximation where the single-field potential could be studied analytically, we argued that, given the assumed form of the potential, the parameter  $\underline{r}$ , which reflects that power in tensor modes, could be no larger than 0.03, and we found explicit solutions where the value was  $\sim 0.01$ . Future measurements of the microwave background polarization, that may probe  $\underline{r} > 0.007$  [28], have the potential of detecting a gravity-wave signal of this size; observational results closer to those of BICEP2 [29] would exclude the model. It would be interesting to consider in more detail the various possibilities for the post-inflationary dynamics and reheating in this scenario.

In Fig. 3.4 and Fig. 3.5, the coordinate  $\tilde{\theta}$  is wrapped in cylindrical coordinate in order to make the discrete shift symmetry manifest. However, in the Dante’s Inferno and Dante’s Waterfall scenario, fields are canonically normalized and independent, *i.e.* the field space metric takes the form of a unit matrix, while in actual cylindrical coordinate system, the  $\theta$ - $\theta$  component of the field space metric is  $\tilde{r}^2$ , which would definitely make nontrivial contribution to the dynamics of the system and calculated slow-roll parameters. Since it remains our interest to explore models predicting larger primordial gravitational wave, a research on the effect of field space metric may shed light on our analysis of multi-field inflation models. In Sec. 3.3, a comprehensive analysis of various inflation scenarios and comparison of models

with same fields and potential but different field space metric is presented, in addition to which, a study of the mass-matrix formalism of single field description is also included.

### 3.3 Field-Space Metric in Spiral Inflation and Related Models

#### 3.3.1 Introduction

In the previous section, we have seen an example of two-field inflation model and depending on the parameter choice, different scenarios of inflation ending could be achieved. Predictions for inflationary observables depend on both the field-space metric and potential of the fields responsible for the inflationary dynamics. Nontrivial kinetic terms which modify the field-space metric arise in many ways: from radiative corrections, from a higher-dimensional origin of the fields, or simply from a field redefinition. Supersymmetric models of inflation typically include nontrivial Kahler potentials which modify the field-space metric, as in Ref. [46, 47] and many of the models reviewed in Refs. [48]. A covariant approach to analyzing fluctuations in an inflationary setting with nontrivial kinetic terms was developed in Ref. [49], and analysis of phenomenological effects of nontrivial kinetic terms in certain inflationary contexts appear in several places, for example Ref. [50]. In this section, we compare two classes of multi-field inflation models which differ only in their kinetic terms, and we discuss some of the lessons learned from these examples. We justify a single-field effective description of these models and derive a mass matrix appropriate for calculation of inflationary observables in these models.

As mentioned in Sec. 3.2.1, the observations by the BICEP2 collaboration of B-modes in the polarization of microwave radiation [29] can be attributed to scattering off of galactic dust [32, 33] as demonstrated by the Planck experiment [34]. However, current and proposed experiments such as PIPER [28] remain sensitive to signatures of primordial gravitational waves produced during inflation. In slow-roll inflation models, the Lyth bound [35] implies that the inflaton field typically varies over super-Planckian values if sufficiently large power

in gravitational waves is produced during inflation. This makes it difficult to describe such an inflationary scenario in terms of an effective field theory valid below the Planck scale. There are several ways to evade the Lyth bound, for example if the slow-roll parameter  $\epsilon$  increases for some period during inflation, as happens in certain hybrid inflation models [36, 37], or if the inflaton is embedded in a multi-field model in which one of the fields has a discrete shift symmetry, as in axion-monodromy models [38]. Simplified models of the latter type were developed in Refs. [39, 40].

Inflationary models based on one or more pseudo-Nambu-Goldstone bosons have a long history (for example, Refs. [51, 52, 53, 54, 55, 56, 57, 58]). Again, we start with the Dante's inferno model, developed in Ref. [40], including two axion fields which evolve along a trench in the potential during inflation, as in Fig. 3.10.

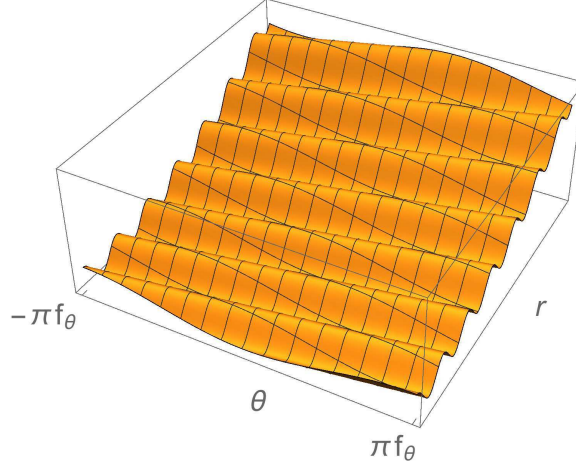


Figure 3.10: The potential as a function of  $r$  and  $\theta$  in Dante's Inferno with a quadratic shift-symmetry-breaking potential  $W(r) = \frac{1}{2}m^2r^2$ , as in Ref. [40].

The two axions  $r$  and  $\theta$  in Dante's inferno have canonical kinetic terms,

$$\mathcal{L}_{\text{DI}} = \frac{1}{2}(\partial_\mu r)^2 + \frac{1}{2}(\partial_\mu \theta)^2 - V(r, \theta). \quad (3.93)$$

The potential has the form

$$V(r, \theta) = W(r) + \Lambda^4 \left[ 1 - \cos \left( \frac{r}{f_r} - \frac{\theta}{f_\theta} \right) \right], \quad (3.94)$$

where the discrete shift symmetry of the axion field  $r$  is broken by the term  $W(r)$  in the potential. A string-theoretic origin of the Dante's Inferno model was presented in Ref. [40], in which the shift-symmetry-breaking potential  $W(r)$  describes the axion on an NS5 brane wrapped on a 2-cycle belonging to a family of homologous 2-cycles which extend into a warped throat geometry.

We will consider a generalization of the potential Eq. (3.94) of the form,

$$V(r, \theta) = W(r) + \Lambda^4 \left[ 1 - \cos \left( \frac{r^n}{f_r^n} - \frac{\theta}{f_\theta} \right) \right]. \quad (3.95)$$

This class of potentials appears in models with a complex scalar field and a single anomalous U(1) symmetry, as in the axion inflation model of Ref. [43]. In this case, the real fields  $r/\sqrt{2}$  and  $\theta$  are the magnitude and phase, respectively, of a canonically normalized complex scalar field  $\Phi = re^{i\theta}/\sqrt{2}$ , in which case we take  $f_\theta = 1$ . The trench spirals around the potential as in Fig. 3.11. The kinetic terms are now different and the Lagrangian takes the form

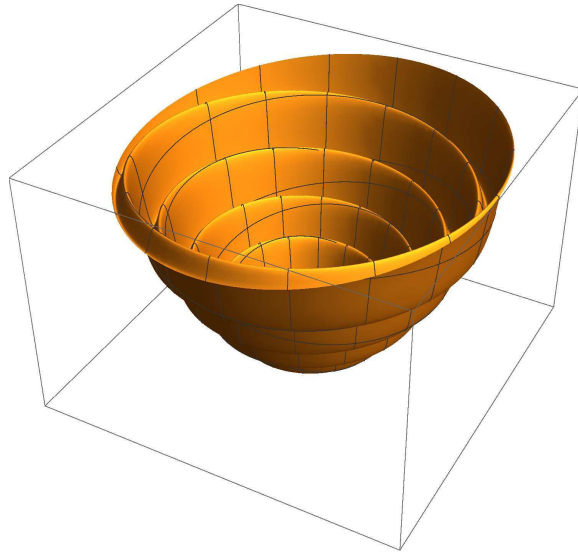


Figure 3.11: The potential as a function of  $r$  and  $\theta$  in a spiral inflation model with a quadratic shift-symmetry-breaking potential  $W(r) = \frac{1}{2}m^2r^2$ . The fields  $r$  and  $\theta$  are represented in polar coordinates.

$$\mathcal{L}_{\text{SI}} = |\partial_\mu \Phi|^2 - V(\Phi) = \frac{1}{2}(\partial_\mu r)^2 + \frac{1}{2}r^2(\partial_\mu \theta)^2 - V(r, \theta). \quad (3.96)$$

In this section we are interested in whether there are generic phenomenological consequences of the difference in kinetic terms in these models. The additional factor of  $r^2$  in the kinetic term for  $\theta$  can have important effects, even affecting the phenomenological viability of these models, as we will see. We compare the predictions for a number of two-field models with canonical and non-canonical kinetic terms of the form Eq. (3.93) and Eq. (3.96). These include models which are effectively either chaotic inflation or hybrid inflation models. Hybrid inflation models of this type include Dante's waterfall [59] and certain spiral inflation [60, 61, 62] models. In the case of spiral inflation we will take  $f_\theta = 1$  so that the potential is periodic in  $\theta \rightarrow \theta + 2\pi$ , while there is a monodromy in shifts of  $r$ . The qualitative difference between these models can be described in terms of the trajectories of the fields which evolve during inflation: In the Dante's inferno and Dante's waterfall scenarios the fields evolve along an approximately linear trajectory in the canonically normalized field space, whereas in spiral inflation models the fields evolve along a nearly circular trajectory. In a single-field effective description both Dante's inferno and spiral inflation are chaotic inflation models, but one must take care in the analysis of models with changing inflaton direction as in spiral inflation.

In Sec. 3.3.2 we describe the single-field effective description of these multi-field models, and derive a mass-matrix whose smaller eigenvalue has the interpretation of the inflaton mass-squared. This mass matrix may be used in the calculation of inflationary observables. In Sec. 3.3.3, we compare the predictions for inflationary observable in a variety of models which differ in their kinetic terms, most of which already appear in the literature. We conclude in Sec. 3.3.4.

### 3.3.2 Single-Field Effective Description

Here we review the single-field description of spiral inflation models with Lagrangian Eq. (3.96), and derive a mass-matrix method for single-field approximation. We begin with analyzing the role of field space metric in the single-field effective description of multi-field inflation models. A more complete analysis of multi-field models requires analysis of the isocur-

vature fluctuations corresponding to fluctuations orthogonal to the inflaton direction as in Refs. [64, 65, 66]. However, in the models considered in this section, the existence of a steep-walled trench in the potential makes those fluctuations massive compared to the Hubble scale so that they are not produced during inflation [43, 44].

### From many fields to one

Consider a model with real scalar fields  $\phi^a$  in a background spacetime described by the metric  $g_{\mu\nu}$ . During inflation we assume the spacetime is given by the flat Friedmann-Robertson-Walker (FRW) metric  $g_{00} = 1$ ,  $g_{ij} = -a^2(t)\delta_{ij}$ , where  $i, j \in \{1, 2, 3\}$  and  $t \equiv x^0$ , but for now we allow an arbitrary time-dependent metric. The Lagrangian for the theory is,

$$\sqrt{|g|}\mathcal{L} = \sqrt{|g|}\frac{1}{2}G_{ab}g^{\mu\nu}\partial_\mu\phi^a\partial_\nu\phi^b - \sqrt{|g|}V(\{\phi^a\}), \quad (3.97)$$

where  $G_{ab}(\{\phi^c\})$  in the kinetic terms defines the field-space metric, which is taken to be symmetric in  $a \leftrightarrow b$ . Under a nonlinear field redefinition  $\phi^a \rightarrow \tilde{\phi}^a(\{\phi^b\})$ , the Lagrangian transforms as,

$$\sqrt{|g|}\mathcal{L} = \sqrt{|g|}\frac{1}{2}G_{ab}\frac{\partial\phi^a}{\partial\tilde{\phi}^c}\frac{\partial\phi^b}{\partial\tilde{\phi}^d}g^{\mu\nu}\partial_\mu\tilde{\phi}^c\partial_\nu\tilde{\phi}^d - \sqrt{|g|}V\left(\phi^a(\{\tilde{\phi}^b\})\right) \quad (3.98)$$

$$\equiv \sqrt{|g|}\frac{1}{2}\tilde{G}_{cd}g^{\mu\nu}\partial_\mu\tilde{\phi}^c\partial_\nu\tilde{\phi}^d - \sqrt{|g|}V\left(\phi^a(\{\tilde{\phi}^b\})\right), \quad (3.99)$$

which defines the transformed field-space metric as

$$\tilde{G}_{cd} = G_{ab}\frac{\partial\phi^a}{\partial\tilde{\phi}^c}\frac{\partial\phi^b}{\partial\tilde{\phi}^d}. \quad (3.100)$$

In this sense, the field-space metric transforms as a tensor under field transformations. Locally one can redefine the fields so that the field-space metric is flat,  $\tilde{G}_{cd} = \delta_{cd}$ , but this can be done globally only if the field-space metric originally describes a flat field space.

In order to compare with a single-field description we consider the equations of motion.

The equations of motion for the fields  $\phi^a$  are,

$$\frac{1}{\sqrt{|g|}} \partial_\mu \left( G_{ab}(\{\phi\}) \sqrt{|g|} g^{\mu\nu} \partial_\nu \phi^b \right) = -\frac{\partial V}{\partial \phi^a} + \frac{1}{2} g^{\mu\nu} \frac{\partial G_{cb}}{\partial \phi^a} \partial_\mu \phi^c \partial_\nu \phi^b. \quad (3.101)$$

We will be interested in spatially uniform solutions to the equations of motion, so that the fields  $\phi^a$  only have dependence on  $t$ . For these solutions, the equations of motion are

$$\frac{1}{\sqrt{|g|}} \frac{d}{dt} \left( \sqrt{|g|} g^{00} G_{ab} \dot{\phi}^b \right) - \frac{1}{2} g^{00} \frac{\partial G_{cb}}{\partial \phi^a} \dot{\phi}^c \dot{\phi}^b = -\frac{\partial V}{\partial \phi^a}, \quad (3.102)$$

where  $\dot{\phi}^a \equiv d\phi^a/dt$ .

Now suppose that the trajectory describing a solution to the equations of motion is known, parametrized by a parameter  $I$  along the trajectory, so that along the given solution we have  $\phi^a(I)$ . For such a solution, the equations of motion determine the time dependence of  $I$ . Multiplying Eq. (3.102) by  $\phi^{a'}$ ( $I$ ) gives,

$$\frac{1}{\sqrt{|g|}} \phi^{a'}(I) \frac{d}{dt} \left( \sqrt{|g|} g^{00} G_{ab} \dot{\phi}^b \right) - \frac{1}{2} g^{00} G'_{ab}(I) \dot{\phi}^a \dot{\phi}^b = -V'(I). \quad (3.103)$$

Now choose  $I$  to satisfy the field-space condition

$$G_{ab} \phi^{a'}(I) \phi^{b'}(I) = 1. \quad (3.104)$$

This condition makes the parameter  $I$  analogous to the invariant length, but in field space, and will give  $I$  the interpretation of a canonically normalized inflaton field, with kinetic term  $\frac{1}{2} \dot{I}^2$ . A derivative of Eq. (3.104) with respect to  $I$  gives,

$$G_{ab}'(I) \phi^{a'}(I) \phi^{b'}(I) + 2G_{ab} \phi^{a''}(I) \phi^{b'}(I) = 0. \quad (3.105)$$

Multiplying by  $\dot{I}^2$ , we have

$$\frac{1}{2} G_{ab}'(I) \dot{\phi}^a \dot{\phi}^b = -G_{ab} \phi^{a''}(I) \dot{\phi}^b \dot{I}. \quad (3.106)$$

Using Eq. (3.106), the equations of motion Eq. (3.103) become,

$$\frac{1}{\sqrt{|g|}}\phi^{a'}(I)\frac{d}{dt}\left(\sqrt{|g|}g^{00}G_{ab}\dot{\phi}^b\right) + g^{00}G_{ab}\phi^{a''}(I)\dot{\phi}^b\dot{I} = -V'(I). \quad (3.107)$$

The first two terms in Eq. (3.107) combine to give a time derivative,

$$\frac{1}{\sqrt{|g|}}\frac{d}{dt}\left(\sqrt{|g|}g^{00}G_{ab}\phi^{a'}(I)\phi^{b'}(I)\dot{I}\right) = -V'(I), \quad (3.108)$$

or using Eq. (3.104),

$$\frac{1}{\sqrt{|g|}}\frac{d}{dt}\left(\sqrt{|g|}g^{00}\dot{I}\right) = -V'(I). \quad (3.109)$$

Together with the trajectory  $\phi^a(I)$  that solves the equations of motion, a solution to Eq. (3.109) then determines the time dependence of that trajectory. Consequently, Eq. (3.109) provides enough information to determine inflationary observables, as long as the fluctuations in the direction orthogonal to the trajectory are massive compared to  $H$  so that those fluctuations (isocurvature fluctuations) are not produced during inflation.

The field-space parameter  $I$  above plays the role of the inflaton in the single-field description of any model with Lagrangian of the form Eq. (3.97). The analysis above supposed that we knew the trajectory along a solution to the equations of motion. Now suppose that we had instead imposed as a constraint that the fields lie on the trajectory  $\phi^a(I)$ . In Dante's inferno and spiral inflation models, the trajectory is approximately known due to the presence of a steep-walled trench in the potential. This is a holonomic constraint, as can be made explicit by inverting the expression for one of the fields, say  $\phi^1(I)$  to give  $I(\phi^1)$ . We assume that this inverse exists throughout the field trajectory. Then the remaining constraints are of the form  $\phi^a - \phi^a(I(\phi^1)) = 0$ . Such constraints can be imposed either by Lagrange multipliers in the Lagrangian, or by simply replacing  $\phi^a$  by  $\phi^a(I)$  in the Lagrangian. We are left with a description of the theory in terms of the single field  $I$ .

If we again choose  $I$  to satisfy the condition Eq. (3.104), then the Lagrangian Eq. (3.97)

constrained to a field-space trajectory takes the canonical form,

$$\sqrt{|g|}\mathcal{L}_I = \sqrt{|g|} \left( \frac{1}{2} g^{00} \dot{I}^2 - V(I) \right). \quad (3.110)$$

The equations of motion that follow from this single-field effective description are the same as Eq. (3.109), which was derived in the multi-field description. This justifies the interpretation of the field  $I$  as the canonical inflaton in these models. Note that the only assumption in the analysis of this section was that we knew the trajectory taken by the fields  $\phi^a$ , which in the models considered in this paper is known by the presence of a steep-walled trench in the potential.

### Spiral Inflation Models and a Mass Matrix

At this stage we will focus on spiral inflation models, for which  $G_{rr} = 1$ ,  $G_{\theta\theta} = r^2$ , and  $G_{r\theta} = G_{\theta r} = 0$ . The condition Eq. (3.104) defining the canonical inflaton field can be written

$$dI^2 = dr^2 + r^2 d\theta^2. \quad (3.111)$$

We suppose that the trajectory  $r(\theta)$ , approximately determined by the shape of the trench in the potential, is known. At a given time, the inflaton direction in field space is specified by the unit vector

$$\hat{\mathbf{e}}_I = c_r \hat{\mathbf{e}}_r + c_\theta \hat{\mathbf{e}}_\theta, \quad (3.112)$$

where

$$c_r = \frac{dr}{dI} = \frac{r'(\theta)}{\sqrt{r^2 + r'^2}}, \quad c_\theta = r \frac{d\theta}{dI} = \frac{r}{\sqrt{r^2 + r'^2}}, \quad (3.113)$$

and the unit vectors  $\hat{\mathbf{e}}_r$  and  $\hat{\mathbf{e}}_\theta$  are the usual basis vectors in polar coordinates, which in a Cartesian coordinate system with  $x = r \cos \theta$ ,  $y = r \sin \theta$  have components  $\hat{\mathbf{e}}_r = \cos \theta \hat{\mathbf{e}}_x + \sin \theta \hat{\mathbf{e}}_y$ ,  $\hat{\mathbf{e}}_\theta = -\sin \theta \hat{\mathbf{e}}_x + \cos \theta \hat{\mathbf{e}}_y$ . In spiral inflation models the field evolution is mostly in the  $\hat{\mathbf{e}}_\theta$  direction. In order to compare with a mass matrix description, as in Ref. [60], we make the approximation that the trajectory is nearly circular, and set to zero

$c_r'(\theta)$ ,  $c_\theta'(\theta)$ , which is a good approximation for typical parameter choices in these models as we will confirm numerically in Sec. 3.3.3.

The slow-roll parameters, and consequently inflationary observables, depend on derivatives of the potential with respect to the canonically normalized inflaton field. In multi-field models this is a directional derivative (which for comparison with the previous section is simply the chain rule with Eq. (3.113)):

$$\frac{dV}{dI} = (\hat{\mathbf{e}}_I \cdot \nabla) V = c_r \partial_r V + c_\theta/r \partial_\theta V, \quad (3.114)$$

where  $\nabla V$  is the gradient in polar coordinates,  $\nabla V = \partial_r V \hat{\mathbf{e}}_r + 1/r \partial_\theta V \hat{\mathbf{e}}_\theta$ . The derivative  $dV/dI$  determines the slow-roll parameter  $\epsilon$  defined by

$$\epsilon = \frac{M_*^2}{2} \left( \frac{V'(I)}{V} \right)^2, \quad (3.115)$$

where  $M_* = 2.4 \times 10^{18}$  GeV is the reduced Planck mass. Noting that

$$\frac{d\hat{\mathbf{e}}_r}{d\theta} = \hat{\mathbf{e}}_\theta, \quad \frac{d\hat{\mathbf{e}}_\theta}{d\theta} = -\hat{\mathbf{e}}_r, \quad (3.116)$$

we have

$$\frac{d^2V}{dI^2} = \frac{d}{dI} (\hat{\mathbf{e}}_I \cdot \nabla) V \quad (3.117)$$

$$= \frac{d\hat{\mathbf{e}}_I}{dI} \cdot \nabla V + \hat{\mathbf{e}}_I \cdot \frac{d}{dI} (\nabla V) \quad (3.118)$$

$$\begin{aligned} &= \frac{d\theta}{dI} (c_r \hat{\mathbf{e}}_\theta - c_\theta \hat{\mathbf{e}}_r) \cdot (\partial_r V \hat{\mathbf{e}}_r + \frac{1}{r} \partial_\theta V \hat{\mathbf{e}}_\theta) \\ &\quad + \hat{\mathbf{e}}_I \cdot \left[ \left( (\hat{\mathbf{e}}_I \cdot \nabla) \partial_r V \right) \hat{\mathbf{e}}_r + \left( (\hat{\mathbf{e}}_I \cdot \nabla) \frac{1}{r} \partial_\theta V \right) \hat{\mathbf{e}}_\theta \right] \\ &\quad + \hat{\mathbf{e}}_I \cdot \left[ \partial_r V \frac{d\hat{\mathbf{e}}_r}{dI} + \frac{1}{r} \partial_\theta V \frac{d\hat{\mathbf{e}}_\theta}{dI} \right] \end{aligned} \quad (3.119)$$

Eq. (3.119) can be simplified using

$$\frac{d\theta}{dI} = \frac{c_\theta}{r}, \quad (3.120)$$

yielding

$$\frac{d^2V}{dI^2} = c_r^2 \partial_r^2 V + 2 \frac{c_r c_\theta}{r} \partial_r \partial_\theta V + \frac{c_\theta^2}{r^2} \partial_\theta^2 V - \frac{c_r c_\theta}{r^2} \partial_\theta V \quad (3.121)$$

$$= \begin{pmatrix} c_r & c_\theta \end{pmatrix} \begin{pmatrix} \partial_r^2 V & \frac{1}{r} \partial_r \partial_\theta V - \frac{1}{2r^2} \partial_\theta V \\ \frac{1}{r} \partial_r \partial_\theta V - \frac{1}{2r^2} \partial_\theta V & \frac{1}{r^2} \partial_\theta^2 V \end{pmatrix} \begin{pmatrix} c_r \\ c_\theta \end{pmatrix}. \quad (3.122)$$

We can now identify the mass matrix appropriate for calculation of inflationary observables,

$$M_{r\theta}^2 = \begin{pmatrix} \partial_r^2 V & \frac{1}{r} \partial_r \partial_\theta V - \frac{1}{2r^2} \partial_\theta V \\ \frac{1}{r} \partial_r \partial_\theta V - \frac{1}{2r^2} \partial_\theta V & \frac{1}{r^2} \partial_\theta^2 V \end{pmatrix}. \quad (3.123)$$

In particular, the slow-roll parameter  $\eta$  is defined as,

$$\eta = M_*^2 \frac{V''(I)}{V}, \quad (3.124)$$

which may be calculated directly in the single-field effective description, or else (to good approximation) as the smaller eigenvalue of the mass matrix  $M_{r\theta}^2$ .

We note that the mass matrix  $M_{r\theta}^2$  differs from the mass matrix of Refs. [60, 61, 62] in the off-diagonal terms, which explains differences in the results of this paper and those of some earlier papers.<sup>1</sup> In particular, by identifying successive derivatives in the  $\hat{\mathbf{e}}_r$  and  $\hat{\mathbf{e}}_\theta$  directions as  $\partial_r$  and  $\partial_\theta/r$ , respectively, the mass matrix of Refs. [60, 61, 62] neglects the  $1/(2r^2)\partial_\theta V$  term in the off-diagonal elements of Eq. (3.123). It is perhaps worthwhile therefore to discuss other mass matrices whose eigenvalues are not directly related to derivatives with respect to the inflaton in the single-field description. To that effect we will introduce some well motivated straw-man mass matrices in spiral inflation models, and describe their physical interpretation in relation to the inflaton dynamics.

Rather than begin with the field-space variables  $r$  and  $\theta$  in spiral inflation models, which have noncanonical kinetic terms, one might have instead considered beginning with field-space variables  $x^1 \equiv r \cos \theta$ ,  $x^2 \equiv r \sin \theta$ , in which case the kinetic terms are canonical and

---

<sup>1</sup>We are grateful to Gabriela Barenboim and Wan-Il Park for discussion on this point.

one can define the mass matrix  $(M_{\text{Cartesian}}^2)_{ij} \equiv \partial_i \partial_j V[r(x, y), \theta(x, y)]$ , where  $\partial_i \equiv \partial/\partial x^i$ . This mass matrix, evaluated at a point in field space, determines the quadratic terms in a Taylor expansion of the potential about that point. Then transforming to the polar variables in the neighborhood of that point,  $(dx, dy)^T \rightarrow (dr, r d\theta)^T = R(\theta)(dx, dy)^T$ , where  $R(\theta)$  is the  $2 \times 2$  rotation matrix with angle  $\theta$ , gives the mass matrix  $\tilde{M}_{\text{Cartesian}}^2$ , where

$$\tilde{M}_{\text{Cartesian}}^2 = R(\theta) M^2 R^{-1}(\theta) = \begin{pmatrix} \partial_r^2 V & \frac{1}{r} \partial_r \partial_\theta V - \frac{1}{r^2} \partial_\theta V \\ \frac{1}{r} \partial_r \partial_\theta V - \frac{1}{r^2} \partial_\theta V & \frac{1}{r^2} \partial_\theta^2 V + \frac{1}{r} \partial_r V \end{pmatrix}, \quad (3.125)$$

so that a Taylor expansion of the potential *in Cartesian coordinates* about a point  $(r_0, \theta_0)$  has quadratic part,

$$V(r, \theta) = \dots + \begin{pmatrix} dr, & r d\theta \end{pmatrix} \begin{pmatrix} \partial_r^2 V & \frac{1}{r} \partial_r \partial_\theta V - \frac{1}{r^2} \partial_\theta V \\ \frac{1}{r} \partial_r \partial_\theta V - \frac{1}{r^2} \partial_\theta V & \frac{1}{r^2} \partial_\theta^2 V + \frac{1}{r} \partial_r V \end{pmatrix} \begin{pmatrix} dr \\ r d\theta \end{pmatrix} + \dots, \quad (3.126)$$

where  $dr = (r - r_0)$ ,  $d\theta = (\theta - \theta_0)$ . The matrix  $\tilde{M}_{\text{Cartesian}}^2$  is also closely related to the matrix of covariant derivatives in polar coordinates,

$$M_{\text{cov } ab}^2 = D_a D_b V = \partial_a \partial_b V - \Gamma_{ab}^c \partial_c V, \quad (3.127)$$

except that  $\theta$  components have been rescaled by  $1/r$  in  $\tilde{M}_{\text{Cartesian}}^2$  to transform to the basis  $(dr, r d\theta)$  from  $(dr, d\theta)$ . Here,  $\Gamma_{ab}^c$  is the Christoffel symbol in field space, with nonvanishing components,

$$\Gamma_{\theta\theta}^r = -r, \quad (3.128)$$

$$\Gamma_{r\theta}^\theta = \Gamma_{\theta r}^\theta = 1/r. \quad (3.129)$$

The eigenvectors of the various mass matrices described above are numerically similar along the trench defined by  $\partial_r V = 0$  in the models considered in this paper. The eigenvalues of the mass matrices, however are quite different. This is illustrated in Fig. 3.13 in a

numerical example of Sec. 3.3.3.

To summarize this subsection, with knowledge of the trajectory describing the evolution of fields constrained to follow a steep-walled trench during inflation, one can define a single-field effective description in terms of a potential  $V(I)$  in terms of a canonically normalized inflaton field  $I$ . The single-field description allows for straightforward computation of inflationary observables, and is the usual procedure for calculation of observables in multi-field models constrained to a trajectory in field space as in spiral inflation models. A mass matrix relating the single-field and multi-field descriptions may be constructed, and differs significantly from the mass matrix as usually defined if the direction of field evolution varies significantly during inflation, as in spiral inflation models.

### 3.3.3 Results

We consider models with both canonical and non-canonical kinetic terms in this section. We use units of the reduced Planck mass  $M_* = 2.4 \times 10^{18}$  GeV throughout. Respectively, the Lagrangians are of the form Eq. (3.93) and Eq. (3.96), where  $V(r, \theta) = W(r) + \Lambda^4 \left[ 1 - \cos \left( \left( \frac{r}{f} \right)^n - \theta \right) \right]$ . The inflaton field is defined so that along a trajectory  $(r(t), \theta(t))$  the field is canonically normalized. Recall that in the Dante's inferno-type model the fields  $r$  and  $\theta$  are canonically normalized, and in spiral inflation models the fields are non-canonically normalized. In these cases, respectively, the inflaton field  $I(t)$  satisfies

$$\begin{aligned} dI_C &= \frac{\dot{r}}{\sqrt{\dot{r}^2 + \dot{\theta}^2}} dr + \frac{\dot{\theta}}{\sqrt{\dot{r}^2 + \dot{\theta}^2}} d\theta , \\ dI_{NC} &= \frac{\dot{r}}{\sqrt{\dot{r}^2 + r^2 \dot{\theta}^2}} dr + \frac{r \dot{\theta}}{\sqrt{\dot{r}^2 + r^2 \dot{\theta}^2}} r d\theta . \end{aligned} \quad (3.130)$$

In both cases, the trajectory closely follows the bottom of the trench defined by  $\partial V(r, \theta)/\partial r = 0$ , or

$$\sin \left( \left( \frac{r}{f} \right)^n - \theta \right) = - \frac{f^n}{n \Lambda^4} W'(r) r^{1-n} . \quad (3.131)$$

We denote the trajectory by  $r(\theta)$ . Eq. (3.130) can be restated as

$$\begin{aligned} dI_C &= \frac{r'}{\sqrt{r'^2 + 1}} dr + \frac{1}{\sqrt{r'^2 + 1}} d\theta = \sqrt{r'^2 + 1} d\theta , \\ dI_{NC} &= \frac{r'}{\sqrt{r'^2 + r^2}} dr + \frac{r}{\sqrt{r'^2 + r^2}} rd\theta = \sqrt{r'^2 + r^2} d\theta . \end{aligned} \quad (3.132)$$

The derivative of  $V$  with respect to  $I$  becomes

$$\begin{aligned} \frac{dV}{dI_C} &= \frac{1}{\sqrt{r'(\theta)^2 + 1}} \frac{dV(r(\theta), \theta)}{d\theta} , \\ \frac{dV}{dI_{NC}} &= \frac{1}{\sqrt{r'(\theta)^2 + r(\theta)^2}} \frac{dV(r(\theta), \theta)}{d\theta} . \end{aligned} \quad (3.133)$$

We normally work in the region where  $r'(\theta) \ll 1$  in the canonical case, and  $r'(\theta) \ll r$  in the non-canonical case. Then, Eq. (3.133) can be approximated by

$$\begin{aligned} \frac{dV}{dI_C} &\approx \frac{dV(r(\theta), \theta)}{d\theta} , \\ \frac{dV}{dI_{NC}} &\approx \frac{1}{r(\theta)} \frac{dV(r(\theta), \theta)}{d\theta} . \end{aligned} \quad (3.134)$$

The slow-roll parameters can now be calculated by

$$\epsilon \equiv \frac{M_*^2}{2} \left( \frac{V'(I)}{V} \right)^2 , \quad \eta \equiv M_*^2 \frac{V''(I)}{V} , \quad \gamma \equiv M_*^4 \frac{V'(I)V'''(I)}{V^2} . \quad (3.135)$$

The inflationary observables are then given by

$$\tilde{r} = [16\epsilon]_{I=I_i} , \quad n_s = [1 + 2\eta - 6\epsilon]_{I=I_i} , \quad \Delta_R^2 = \left[ \frac{V}{24\pi^2\epsilon} \right]_{I=I_i} , \quad n_r = [16\epsilon\eta - 24\epsilon^2 - 2\gamma]_{I=I_i} , \quad (3.136)$$

where  $I_i$  is the value of the inflaton field at the time when the observed inflationary perturbations were created, which in most models is 50-60  $e$ -folds before the end of inflation, but is sensitive to the details of reheating after inflation. The observable  $\tilde{r}$  is the ratio of the tensor to scalar amplitude, where we use the unconventional tilde over  $r$  to distinguish the observable from the field  $r$  in these models. The other observables are the scalar tilt  $n_s$ ; the

scalar amplitude  $\Delta_R^2$ , also denoted  $A_s$ ; and the running of the scalar tilt  $n_r$ . Definitions in terms of the CMB spectrum are available in many places, for example in the Planck 2015 results papers [63].

The number of  $e$ -folds is given by

$$N_e = \int_{I_i}^{I_f} \frac{V}{V'(I)} dI . \quad (3.137)$$

In our numerical analysis we take the attitude that the window of inflation between the time that inflationary perturbations observable on current cosmological scales and the time at which inflation ended is sensitive to details of the post-inflationary dynamics, and we assume that the “initial” point of inflation, *i.e.* the time at which fluctuations on today’s cosmological scales were created, is such that  $n_s = 0.96$  and  $\Delta_R^2 = 2.2 \times 10^{-9}$ , close to the values measured by the Planck experiment [63],  $n_s = 0.9655 \pm 0.0062$ ,  $\ln(10^{10} \Delta_R^2) = 3.089 \pm 0.036$ . The current experimental constraint on  $n_r$  is based on the Planck measurement,  $n_r = -0.003 \pm 0.015$  [63]. The end of inflation occurs when either

$$[\epsilon]_{I=I_f} = 1, \quad (3.138)$$

or when the potential reaches a hybrid-inflation-type instability as in the Dante’s waterfall model. Two types of  $W(r)$  are studied in the following sections and their corresponding single-field approximations are compared with the full theory.

$$\lambda r^p$$

We first consider  $W(r) = \lambda r^p$ . The trench equation Eq. (3.131) becomes

$$\sin\left(\left(\frac{r}{f}\right)^n - \theta\right) = -\frac{p\lambda f^n}{n\Lambda^4} r^{p-n} . \quad (3.139)$$

We consider the case that during inflation the magnitude of the right-hand side of Eq. (3.139) is  $\ll 1$ , corresponding to a steep-walled trench, so that Eq. (3.139) can be solved by

$$\theta = \frac{r^n}{f^n} + \frac{p\lambda f^n}{n\Lambda^4} r^{p-n} \quad (3.140)$$

up to a constant phase. If we choose parameters so that the second term on the right-hand side is negligible, Eq. (3.140) reduces to  $r = f\theta^{\frac{1}{n}}$ , and away from the global minimum of the potential we have  $V(r(\theta), \theta) \approx W(r(\theta)) = \lambda f^p \theta^{\frac{p}{n}}$ . From Eq. (3.132), we have

$$\begin{aligned} dI_C &\approx d\theta , \\ dI_{NC} &\approx f\theta^{\frac{1}{n}} d\theta . \end{aligned} \quad (3.141)$$

The single-field description of the potential in this approximation is therefore given by the potential,

$$\begin{aligned} V_C(I) &\sim I^{\frac{p}{n}} , \\ V_{NC}(I) &\sim I^{\frac{p}{n+1}} . \end{aligned} \quad (3.142)$$

We work through the ( $p = 4$ ,  $n = 1, 2$ ) case for illustration.

$$p = 4, n = 1$$

First we show the predictions of the observables from the single-field approximation. Using Eqs. (3.134)–(3.138), we analyze theories with both canonical and non-canonical kinetic terms, as earlier. For  $(p, n) = (4, 1)$ , Eq. (3.140) is now  $\theta = \frac{r}{f} + \frac{4\lambda f}{\Lambda^4} r^3$ . Assuming the second term on the right-hand-side is negligible, we get that the trench follows  $r(\theta) \approx f\theta$  thus  $V(r(\theta), \theta) \approx W(r(\theta)) = \lambda f^4 \theta^4$ . We determine the initial and final point of inflation in field space by fixing  $n_s = 0.96$  and  $[\epsilon]_{\theta=\theta_f} = 1$ . Note that  $n_s$  and  $\epsilon$  are not sensitive to the overall scale in the potential while  $\Delta_R^2$  is, so  $\Delta_R^2$  can be controlled by rescaling the potential. Fixing observables this way, the model then predicts the number of  $e$ -folds during inflation and the ratio of tensor to scalar amplitudes  $\tilde{r}$ . The results are given in Table 3.1.

	$\theta_i$	$\theta_f$	$\tilde{r}$	$N_e$	$V(I)$
$C$	$10\sqrt{6}$	$2\sqrt{2}$	0.2133	74	$\sim I^4$
$NC$	$(\frac{800}{f^2})^{\frac{1}{4}}$	$(\frac{8}{f^2})^{\frac{1}{4}}$	0.16	49.5	$\sim I^2$

Table 3.1: Observables from the single-field approximation for the  $(p, n) = (4, 1)$  model, fixing  $n_s = 0.96$  and  $[\epsilon]_{\theta=\theta_f} = 1$ .

In a more precise analysis, rather than assume that the trajectory is given by an approximation to the shape of the trench, we solve the field equations for the time dependence of the inflaton trajectory and use that trajectory to determine the effective single-field description of the model as described in Sec. 3.3.2. We find for this model, in units  $M_* = 1$ , the following examples of parameter sets and the corresponding predictions for observables and the number of  $e$ -folds in the inflationary window as defined earlier: With  $(\lambda, \Lambda^4, f)_C = (0.02025, 1.377 \times 10^{-9}, 0.001)$  and  $(\lambda, \Lambda^4, f)_{NC} = (6.525 \times 10^{-6}, 1.68 \times 10^{-10}, 0.001)$ , we get that  $(\tilde{r}, n_s, n_r, \Delta_R^2, N_e)_C = (0.2012, 0.96, -4.88 \times 10^{-4}, 2.2 \times 10^{-9}, 73.87)$  and  $(\tilde{r}, n_s, n_r, \Delta_R^2, N_e)_{NC} = (0.1593, 0.96, -7.97 \times 10^{-4}, 2.2 \times 10^{-9}, 49.52)$ . Note that in the non-canonical case the coupling  $\lambda$  is driven to be nonperturbative and the perturbative analysis is not valid, but for the purpose of comparison with the single-field description we treat this case classically. The results match well with those from Table 3.1, derived from the single-field approximation. The dynamical solutions to the equations of motion Eq. (3.102) are plotted in Fig 3.12. In order to test the sensitivity to changes in the presumed window of inflation, we checked that with the same parameters assuming 60  $e$ -folds of inflation we would obtain  $n_s = 0.951$  in the canonical case and  $n_s = 0.967$  in the noncanonical case. The latter would still be phenomenologically viable, but the former is likely ruled out.

Note that the nontrivial field-space metric in the non-canonical case has the consequence of reducing both the number of  $e$ -folds and  $\tilde{r}$ . However, this model is ruled out by the large values of  $\tilde{r} > 0.11$  [63] and  $N_e > 60$  in the canonical case, and the large value of  $\tilde{r}$  in the non-canonical case.

For the non-canonical case, the eigenvalues and eigenvectors of the three different ma-

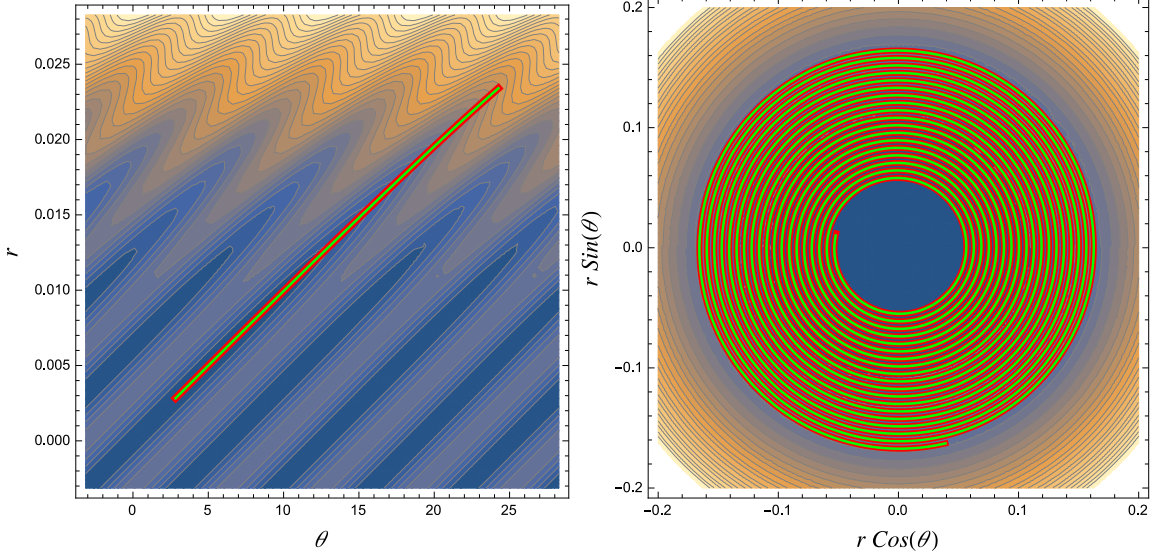


Figure 3.12: Contour plot of the potential for  $p = 4$ ,  $n = 1$ . The canonical case is plotted on the left, the non-canonical case is plotted on the right. The red line indicates the bottom of the trench. The inflationary trajectory is shown by the green line.

trices discussed in Sec. 3.3.2 are shown in Fig 3.13. Note that the eigenvectors are similar for all three mass matrices, but the eigenvalues disagree. The solid blue line corresponds to the mass matrix of Eq. (3.123), and the smaller eigenvalue of this matrix agrees with the second derivative of the potential along the inflaton direction. Hence, diagonalizing this mass matrix allows for calculation of observables that depend on that second derivative, although it is simpler to work with the single-field effective description.

For completeness, in Fig. 3.14, we plot the larger eigenvalue  $m_\perp$  of the mass matrix Eq. (3.123) compared to the Hubble parameter along the inflaton trajectory to demonstrate that  $m_\perp/H \gg 1$  as required for the absence of isocurvature modes produced during inflation. This requirement is generally satisfied in the models considered in this section, and we provide plots for this example and later (in Fig. 3.16) for the Dante's waterfall model with noncanonical kinetic term.

$$p = 4, n = 2$$

For  $(p, n) = (4, 2)$ , Eq. (3.140) gives  $r = \alpha \sqrt{\theta}$ , where  $\alpha = (\frac{1}{f^2} + \frac{4\lambda f^2}{2\Lambda^4})^{-\frac{1}{2}}$ . Thus  $V(r(\theta), \theta) \approx W(r(\theta)) = \lambda \alpha^4 \theta^2$ . Following the analysis of the previous section, the results

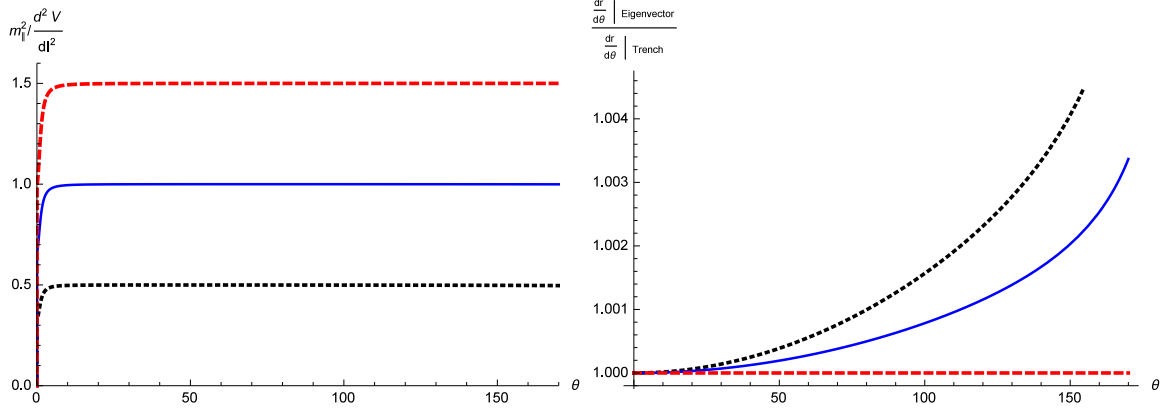


Figure 3.13: The solid blue line, dotted black line, and dashed red line correspond to our mass matrix Eq. (3.123), the Cartesian mass matrix Eq. (3.125), and the mass matrix of Refs. [60, 61, 62], respectively. The lower eigenvalue of each matrix, indicated as  $m_{\parallel}^2$  in units of  $d^2V/dI^2$ , is plotted along the trench in the left graph. The corresponding eigenvector's slope is shown on the right, compared to that of the trench.

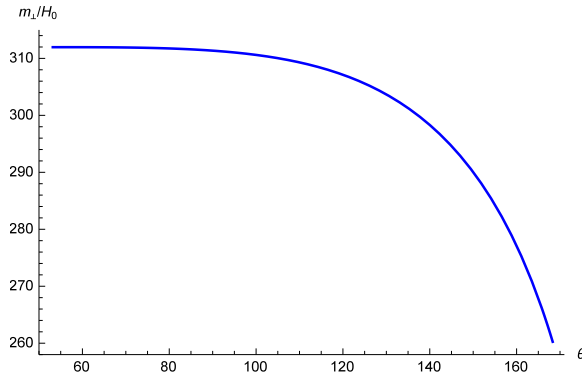


Figure 3.14: The larger eigenvalue  $m_{\perp}$  of the mass matrix Eq. (3.123) compared to the Hubble parameter along the inflaton trajectory in spiral inflation with  $p = 4$ ,  $n = 1$ .

are given in Table 3.2.

Numerical results of the complete two-field models follow. With  $(\lambda, \Lambda^4, f)_C = (27.5, 8.8 \times 10^{-10}, 0.001)$  and  $(\lambda, \Lambda^4, f)_{NC} = (0.0105, 2.1 \times 10^{-11}, 0.001)$ , we get that  $(\tilde{r}, n_s, n_r, \Delta_R^2, N_e)_C = (0.1578, 0.96, -7.83 \times 10^{-4}, 2.2 \times 10^{-9}, 49.71)$  and  $(\tilde{r}, n_s, n_r, \Delta_R^2, N_e)_{NC} = (0.128, 0.96, -9.6 \times 10^{-4}, 2.2 \times 10^{-9}, 41.33)$ . Note that in the canonical case the coupling  $\lambda$  is driven to be nonperturbative and the perturbative analysis is not valid, but for the purpose of comparison with the single-field description we treat this case classically. The results match relatively well with those from single-field approximations. Note that, again, the

	$\theta_i$	$\theta_f$	$\tilde{r}$	$N_e$	$V(I)$
$C$	$10\sqrt{2}$	$\sqrt{2}$	0.16	49.5	$\sim I^2$
$NC$	$(\frac{250}{\alpha^2})^{\frac{1}{3}}$	$(\frac{2}{\alpha^2})^{\frac{1}{3}}$	0.128	41.33	$\sim I^{\frac{4}{3}}$

Table 3.2: Observables from the single-field approximation for the  $(p, n) = (4, 2)$  model, fixing  $n_s = 0.96$  and  $[\epsilon]_{\theta=\theta_f} = 1$ .

non-canonical kinetic term leads to a reduced  $\tilde{r}$  and  $N_e$ .

We also notice that the  $(4, 2)_C$  model gives similar numerical predictions to the  $(4, 1)_{NC}$  model. More generally, from Eq. (3.142) we see that the  $(p, n+1)_C$  model and  $(p, n)_{NC}$  model have the same single-field approximation. This is a type of duality between inflation models. The dynamical solutions are plotted in Fig 3.15.

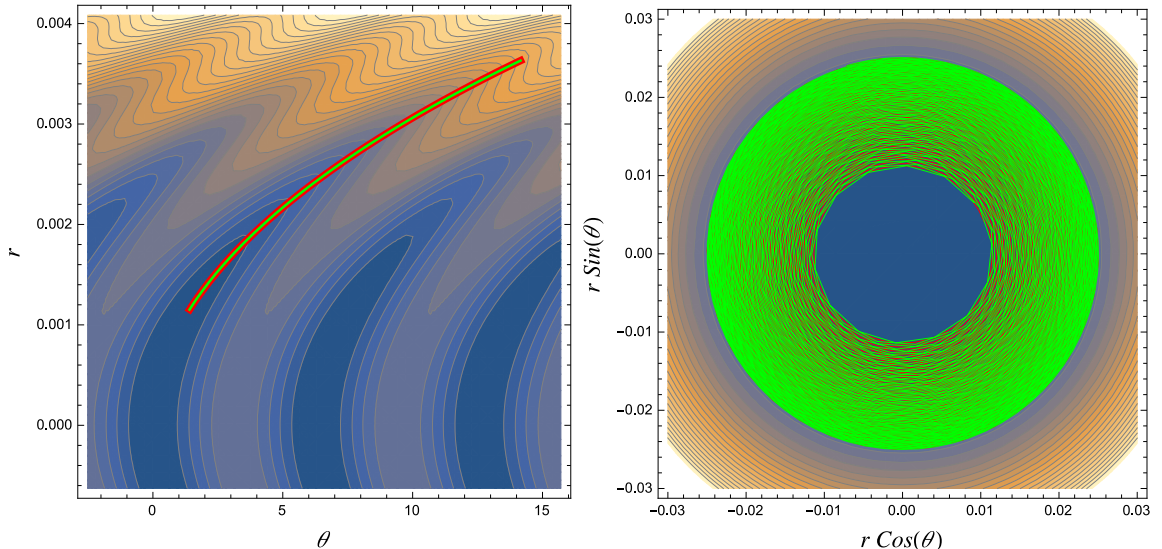


Figure 3.15: Contour plot of the potential for  $p = 4$ ,  $n = 2$ . The canonical case is plotted on the left, the non-canonical case is plotted on the right. The red line indicates the bottom of the trench. The inflationary trajectory is shown by the green line.

$\lambda I^p$  with the desired observables

We see from the above that the viability of these models is sensitive only to the power  $p$  in the single-field effective description, as long as the single-field description is valid. Here we assume a simple potential  $V(I) = \lambda I^p$  in the single-field description and work out the value of  $p$  that would reproduce desired observables with the inflation process spanning 60

$e$ -folds. Using Eqs. (3.160)–(3.138) and fixing  $n_s = 0.96$ , one gets  $N_e = \frac{49}{4}p + 25$ . Imposing  $N_e = 60$ , we have  $p = 20/7$ .  $\tilde{r}$  is then calculated to be 0.188. Other observables may be calculated or fixed as in the earlier analysis.

### Mexican hat

Now we consider the potential  $W(r) = -\frac{1}{2}m^2r^2 + \frac{\lambda}{4}r^4 + \frac{m^4}{4\lambda}$  as in Dante's waterfall. Eq. (3.131) becomes

$$\sin\left(\left(\frac{r}{f}\right)^n - \theta\right) = \frac{f^n}{n\Lambda^4}(m^2r^{2-n} - \lambda r^{4-n}). \quad (3.143)$$

We again consider the  $n = 1, 2$  cases for this potential and assume that the inflationary system starts near the origin where  $-\frac{1}{2}m^2r^2$  dominates over  $\frac{\lambda}{4}r^4$ .

$$n = 1$$

With  $n = 1$ , Eq. (3.143) reduces to  $r = \alpha\theta$  if we neglect the  $\lambda$  term, where  $\alpha = (\frac{1}{f} - \frac{fm^2}{\Lambda^4})^{-1}$ . For a stable trench to exist, the trench equation Eq. (3.143) should be solvable; however, over a range of  $r$  a solution might not exist, depending on the model parameters [59, 60]. The canonical case is analyzed in Ref. [59], where a viable parameters space is found with inflation ending as in hybrid inflation. For the non-canonical case, with  $(m, \lambda, \Lambda^4, f) = (8.88 \times 10^{-4}, 33.5 m^2, 7.2 \times 10^{-5} m^2, 0.001)$ , we have  $(\tilde{r}, n_s, n_r, \Delta_R^2, N_e) = (0.1608, 0.96, -7.55 \times 10^{-4}, 2.2 \times 10^{-9}, 49.77)$ . The end of inflation happens when  $[\epsilon]_{\theta=\theta_f} = 1$  in this example. Alternatively, if we change the  $\Lambda^4$  to be  $6.65 \times 10^{-5} m^2$  in the above example, this model becomes a hybrid model as Dante's waterfall and inflation ends when the trench loses stability. The observables become  $(\tilde{r}, n_s, n_r, \Delta_R^2, N_e) = (0.1610, 0.96, -7.52 \times 10^{-4}, 2.2 \times 10^{-9}, 21.22)$ .

We check the condition  $m_\perp/H \gg 1$  for the absence of isocurvature perturbations produced during inflation in Fig. 3.16.

We note that in the Dante's waterfall model the ratio of tensor to scalar amplitudes  $\tilde{r}$  was found to be typically small with  $\tilde{r} < 0.03$ . The noncanonical kinetic term in the spiral inflation models above would predict larger values of  $\tilde{r}$  but smaller  $N_e$  than in the Dante's

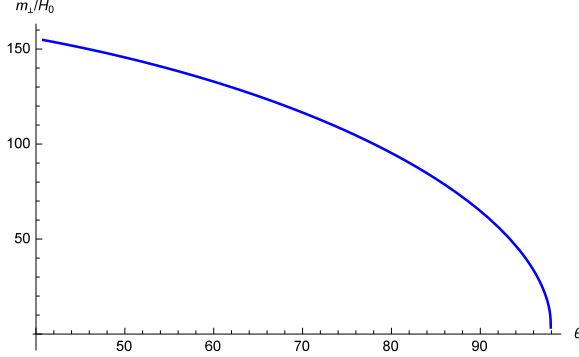


Figure 3.16: The larger eigenvalue  $m_{\perp}$  of the mass matrix Eq. (3.123) compared to the Hubble parameter along the inflaton trajectory in the Dante's waterfall scenario with  $n = 1$  and noncanonical kinetic term.

waterfall model, and it is challenging to find a viable parameter space in this class of spiral inflation models.

$$n = 2$$

With  $n = 2$ , Eq. (3.143) leads to  $r = \alpha\sqrt{\theta + \beta}$ , where  $\alpha = (\frac{1}{f^2} + \frac{\lambda f^2}{2\Lambda^4})^{-\frac{1}{2}}$  and  $\beta = \frac{f^2 m^2}{2\Lambda^4}$ . We define a new field  $\theta' \equiv \theta + \beta$ , thus  $V(r(\theta')) \approx -\frac{1}{2}m^2\alpha^2\theta' + V_0$ . Using Eq. (3.141), the canonical and non-canonical cases should be effectively described by  $V_C(I) = -I + V_0$  and  $V_{NC}(I) = -I^{-\frac{2}{3}} + V_0$ , respectively. For the canonical case, we have the same prediction as the non-canonical  $n = 1$  case discussed above with  $\tilde{r} = 0.1067$ ,  $N_e = 37.5$ . The numerical results for the non-canonical case are presented below.

With  $(m, \lambda, \Lambda^4, f)_C = (0.457, 500 m^2, 1 \times 10^{-6} m^2, 0.001)$  and  $(m, \lambda, \Lambda^4, f)_{NC} = (0.0677, 150 m^2, 5 \times 10^{-7} m^2, 0.001)$ , we find  $(\tilde{r}, n_s, n_r, \Delta_R^2, N_e)_C = (0.16, 0.96, -8 \times 10^{-4}, 2.2 \times 10^{-9}, 49.5)$  and  $(\tilde{r}, n_s, n_r, \Delta_R^2, N_e)_{NC} = (0.1611, 0.96, -7.97 \times 10^{-4}, 2.2 \times 10^{-9}, 49.61)$ . It is noticeable that the numerical results of all three models with  $W(r) = -\frac{1}{2}m^2r^2 + \frac{\lambda}{4}r^4 + \frac{m^4}{4\lambda}$  considered in this section coincide with the prediction of a  $V(I) \sim I^2$  model. This may be a result of the inflationary process occurring close to the minimum of the potential where the potential can be described as  $\sim I^2$ .

### 3.3.4 Comments

We have analyzed and compared a variety of two-field inflation models with one or two axions, in particular Dante’s inferno/waterfall-type models and spiral inflation models. These models include a trench in the two-field potential that constrains the trajectory of the fields during inflation and justifies a single-field description. Dante’s inferno and spiral inflation models are described by equivalent potentials, but differ in the kinetic terms for the fields, or equivalently the field-space metric. We have found that, not surprisingly, the field-space metric plays an important role in predictions for inflationary observables, with spiral inflation models generally requiring a smaller number of  $e$ -folds  $N_e$  during inflation and predicting a smaller tensor-to-scalar ratio  $\tilde{r}$  than the Dante’s inferno model with the same potential. Whereas the Dante’s waterfall scenario yields a phenomenologically viable parameter space, the corresponding spiral inflation model appears to face tighter phenomenological constraints.

In some of the recent spiral inflation literature, observables were calculated using a mass-matrix formalism rather than appealing to a single-field effective description. It has been suggested that the single-field description, which maps these models to chaotic-inflation type models during inflation, is not generally valid [62]. We have argued that a single-field description which maps these models into chaotic inflation models is valid (until the end of inflation, at which point the multi-field nature of the models is indeed important), and we constructed the mass matrix relevant for comparison with the single-field description. The geometric approach taken here can be generalized to other multi-field models, but is simplified in spiral-inflation models by their nearly circular field-space trajectories.

The single-field description relates observables in Dante’s inferno-type models to those in spiral inflation models with related potentials, which is a type of duality between inflation models. Finally, we note that both the Dante’s inferno and spiral inflation models have a flat field space, albeit in different parametrizations. It would be worthwhile to classify the effects of field-space curvature on inflation models with potential trenches, generalizing the models analyzed here.

So far in this dissertation, there has been no connection between the inflaton field and the standard model. In the next section, a scenario is presented in which the two axions are pseudo-Nambu-Goldstone bosons resulting from spontaneously broken accidental continuous global flavor symmetries. These flavor symmetries are from the model of flavons, which is an extension to the standard model, giving rise to the hierarchy of fermion masses.

## 3.4 Flavored Axion-Monodromy Inflation

### 3.4.1 Introduction

Effective inflationary models, as discussed in the previous two sections, are often studied in terms of the properties of the inflaton potential and the predictions for the spectrum of fluctuations in the microwave background. However, there is less focus on other roles the inflaton could play in extensions of the standard model. If the only purpose of the inflaton field is to drive inflation, then its model building would be isomorphic to studying ways of generating various functional forms for the inflaton potential. Review of these possibilities can be found in [67]).

In this section, an axion-monodromy inflation model is embedded as an integral part of an extension of the standard model, which models the flavor sector thus addressing the hierarchy of elementary fermion masses. Horizontal discrete symmetries in flavor models are set to be broken by a series of fields, namely flavons, which couple to standard model fermions through higher-dimensional operators. Resulting from the discrete flavor symmetries, there are often accidental continuous global symmetries respected by renormalizable terms of the flavon potential. In this scenario, the axions in the inflation model are approximate goldstone bosons appear as these accidental symmetries are spontaneously broken. The model presented in this part of the work focus on two-axion case hence distinguishing the present work from the relatively sparse literature that explores the use of flavon fields for a similar purpose [68].

Consider a single flavon field  $\Psi$  transforming under a  $\mathbf{Z}_N$  flavor symmetry as  $\Phi \rightarrow \omega\Phi$ ,

where  $\omega = \exp(2\pi i/N)$ . If the standard model fermions are charged under the discrete group, a tree-level Yukawa coupling would then be possible through a higher-dimensional operator. For example, for a down-type quark, one might have

$$\frac{1}{M_F^p} \bar{Q}_L H \phi^p D_R + \text{h.c.} , \quad (3.144)$$

where  $H$  is the standard model Higgs doublet,  $M_F$  is the flavor scale, and  $p$  is an integer. The Yukawa coupling is associated with the ratio  $(\langle \phi \rangle / M_F)^p$  which can be much less than one; hierarchical pattern of entries in the Yukawa matrix can be easily filled by operators with different values of  $p$ . The flavor scale  $M_F$  is identified with that of new heavy states that account for the origin of the higher-dimensional operators. In this model, a simpler assumption is adopted that  $M_F$  is the reduced Planck mass  $M_*$ ; the desired operators appear as part of the most general set that are allowed by the local symmetries of the theory, as one expects based on our current understanding of quantum gravity [69]. Immediately followed from this assumption, we have the vacuum expectation value (vev)  $\langle \Phi \rangle < M_*$ , leading to an important constraint in our attempt to identify the inflaton with a part of the field  $\Phi$ .

To obtain an inflation potential, the goldstone boson degree-of-freedom receives no contribution to its potential from renormalizable terms involving  $\Psi$ . Assume that  $N \geq 5$ , the renormalizable terms in the potential are simply

$$V(\Phi) = -m_\Phi^2 \Phi^\dagger \Phi + \frac{\lambda_\Phi}{2} (\Phi^\dagger \Phi)^2 . \quad (3.145)$$

Terms such as  $(\Phi^4 + \text{h.c.})$  are forbidden by the  $\mathbf{Z}_N$  symmetry. Using the nonlinear decomposition

$$\Phi = \frac{\phi + f}{\sqrt{2}} \exp(i\theta/f) , \quad (3.146)$$

where  $f/\sqrt{2} \equiv \langle \Phi \rangle$ , one sees immediately that  $V(\Phi)$  is independent of  $\theta$ , leading to an spontaneously broken accidental global  $U(1)$  symmetry with  $\theta$  being the goldstone boson. Since global symmetries are not respected by quantum gravitational corrections, it is natural

to expect Planck suppressed corrections,

$$\mathcal{L} \supset \frac{c_0}{2} \frac{1}{M_*^{N-4}} \Phi^N + \text{h.c.} , \quad (3.147)$$

that generate a potential for  $\theta$ , where  $c_0$  is an unknown order-one coefficient. In the models considered in this section, Planck-suppressed operators that directly breaks the discrete flavor symmetry are not present since we assume discrete gauge symmetries preserved with appropriate anomaly cancellation conditions satisfied thus immune to quantum gravitational corrections. Basic issues of discrete gauge symmetries relevant to our model building are review in the appendix.

The operator in Eq. (3.147) leads to the  $\theta$  potential

$$V(\theta) = c_0 M_*^4 \left( \frac{\langle \Phi \rangle}{M_*} \right)^N [1 - \cos(N\theta/f)] . \quad (3.148)$$

A constant have been added to make sure  $V(0) = 0$ . This is exactly the potential one expects in “Natural Inflation” scenarios [51, 52]. But as argued in the previous two sections, if set to predict a spectral index  $n_s$  within the range allowed by current Planck data, such model would require super-Planckian field values. Then  $f$  must be well above the Planck scale [39]. For our present application, this would imply that  $\langle \phi \rangle / M_*$  is not a small flavor-symmetry-breaking parameter and we lose the ability to predict standard model Yukawa couplings in a controlled approximation. Again, two-field axion-monodromy models [38, 40, 59, 43, 44, 60, 61, 70, 71] are used to resolve this problem in this section. We will show that these can be adapted for the present purpose.

The two pseudo-goldstone fields can have their origin if there are two flavon fields,  $\Psi$  and  $\chi$ , that transform under the discrete group  $\mathbf{Z}_p^\Phi \times \mathbf{Z}_r^\chi$ . Each field is assumed to transform only under one of the  $\mathbf{Z}_N$  factors,

$$\Phi \rightarrow \omega_\Phi \Phi \quad \text{and} \quad \chi \rightarrow \omega_\chi \chi , \quad (3.149)$$

where  $\omega_\Phi = \exp(2\pi i/p)$  and  $\omega_\chi = \exp(2\pi i/r)$ , where  $p$  and  $r$  are integers. For  $p \geq 5$  and  $r \geq 5$ , the renormalizable terms in the potential are

$$V(\Phi, \chi) = -m_\Phi^2 \Phi^\dagger \Phi + \frac{\lambda_\Phi}{2} (\Phi^\dagger \Phi)^2 - m_\chi^2 \chi^\dagger \chi + \frac{\lambda_\chi}{2} (\chi^\dagger \chi)^2 + \lambda_p \Phi^\dagger \Phi \chi^\dagger \chi , \quad (3.150)$$

where  $\lambda_p$  is a portal-type coupling. The parameters are chosen such that each field develops a vev. This potential has an accidental  $U(1) \times U(1)$  global symmetry that is spontaneously broken. Extending our previous parameterization, we write

$$\Phi = \frac{\phi_0 + f_\theta}{\sqrt{2}} \exp(i\theta/f_\theta) \quad \text{and} \quad \chi = \frac{\chi_0 + f_\rho}{\sqrt{2}} \exp(i\rho/f_\rho) . \quad (3.151)$$

Spontaneous symmetry breaking renders the fields  $\phi_0$  and  $\chi_0$  massive so that they are decoupled from the inflation dynamics. The potential for the goldstone bosons  $V(\rho, \theta)$  that follows from Eq. (3.150) is exactly flat.

We will discuss later how to generate a potential for  $\rho$  and  $\theta$  of the following axion-monodromy form

$$V(\rho, \theta) = \Lambda_1^4 \left[ 1 + \cos \left( \frac{\rho}{f_\rho} \right) \right] + \Lambda_2^4 \left[ 1 - \cos \left( \frac{n\rho}{f_\rho} - \frac{\theta}{f_\theta} \right) \right] , \quad (3.152)$$

where  $n$  is an integer. The first few terms in the expansion of the first cosine factor have the same form as  $-m_r^2 r^2/2 + \lambda_r r^4/4!$ , the shift-symmetry-breaking potential  $W(r)$  assumed in the Dante's Waterfall scenario discussed in Ref. [59]. In this section, it is again assumed this form of the potential in (Eq. 3.152) is readily obtained with field theoretic origins. This monodromy scenario allows for large number of  $e$ -folds to be achieved within a bounded, sub-Planckian region of field space. The decay constant  $f_\theta$  is assumed to satisfy

$$\frac{f_\theta}{\sqrt{2}} = \lambda M_* \approx 0.22 M_* , \quad (3.153)$$

where  $\lambda$  is a flavor-symmetry-breaking parameter of the same size as the Cabibbo angle. This will allow us to identify the field  $\Phi$  (and perhaps in some models both  $\Phi$  and  $\chi$ ) as

flavons that can be used in flavor model building. We will see that the discrete symmetry  $\mathbf{Z}_p^\Phi \times \mathbf{Z}_r^\chi$  serves four purposes: (*i*) it assures that there are goldstone bosons that have no potential generated by renormalizable couplings, (*ii*) it will serve as a flavor symmetry to create a hierarchy of standard model fermion Yukawa couplings, (*iii*) it will lead to the correct pattern of couplings in a new gauge sector that provides for the desired form of the inflaton potential, Eq. (3.152), and (*iv*) it will keep quantum gravitational corrections to the potential highly suppressed.

The remaining contents of this section are organized as follows. In Sec. 3.4.2, the inflationary dynamics that follows from the potential given in Eq. (3.152) is researched. Solutions are classified into two categories: the ones in which inflation ends when single-field slow-roll conditions are violated and others where the termination of inflation is analogous to a hybrid model [42]. Model building issues are considered in Sec. 3.4.3, in particular, how the discrete symmetries of the theory play an important role in assuring that the proper potential is obtained, and how the same symmetries can be used to produce a plausible model of standard model fermion masses. Our comments are summarized in Sec. 3.4.4. A brief review of discrete gauge symmetries is provided in Appendix A.

### 3.4.2 Inflationary Trajectories

In this section, inflationary trajectories are studied for the two-field potential given by Eq. (3.152), that are compatible with flavor model-building requirement Eq. (3.153). Two example solutions that differ qualitatively in how inflation ends are given.

#### Termination without a waterfall.

For our first solution, we make the parameter choice  $f_\rho = f_\theta \equiv f_1$  and also define  $f_1/n \equiv f_2$ . We assume  $f_1 \gg f_2$ , which is equivalent to  $n \gg 1$ . The potential Eq. (3.152) then takes the form

$$V(\rho, \theta) = \Lambda_1^4 \left[ 1 + \cos \left( \frac{\rho}{f_1} \right) \right] + \Lambda_2^4 \left[ 1 - \cos \left( \frac{\rho}{f_2} - \frac{\theta}{f_1} \right) \right]. \quad (3.154)$$

The second cosine term creates a series of trenches on the surface of the potential defined by the first cosine term. If the field  $\theta$  is plotted as a polar coordinate, the trenches form spirals originating at  $\rho = 0$ . As in Ref. [59], it is convenient to work in the rotated field basis  $\rho = c\tilde{\rho} + s\tilde{\theta}$  and  $\theta = c\tilde{\theta} - s\tilde{\rho}$  with

$$c = \frac{f_1}{\sqrt{f_1^2 + f_2^2}} \quad \text{and} \quad s = \frac{f_2}{\sqrt{f_1^2 + f_2^2}} . \quad (3.155)$$

This allows us to rewrite the potential as

$$V(\tilde{\rho}, \tilde{\theta}) = \Lambda_1^4 \left[ 1 + \cos \left( \frac{c\tilde{\rho} + s\tilde{\theta}}{f_1} \right) \right] + \Lambda_2^4 \left[ 1 - \cos \left( \frac{\tilde{\rho}}{f} \right) \right] , \quad (3.156)$$

where  $f = f_1 f_2 / \sqrt{f_1^2 + f_2^2}$ . The modulations in the potential due to the  $\cos(\tilde{\rho}/f)$  term create the trench, whose location is given by  $\partial V / \partial \tilde{\rho} = 0$ , or

$$\sin \left( \frac{\tilde{\rho}}{f} \right) - s c \frac{\Lambda_1^4}{\Lambda_2^4} \sin \left( \frac{c\tilde{\rho} + s\tilde{\theta}}{f_1} \right) = 0 . \quad (3.157)$$

The inflaton is the linear combination of the fields that slowly rolls along the trench; inflation terminates when the slow-roll conditions are violated. For the solutions considered in this subsection, the stability condition  $\partial^2 V / \partial \tilde{\rho}^2 > 0$  will hold throughout this trajectory.

To study inflationary observables, we first consider a good approximation to the single-field inflaton potential, which holds for our choice of parameters and can be studied analytically, and then discuss an exact numerical approach that we use to confirm the validity of our results. Let us define  $\kappa \equiv s c (\Lambda_1^4 / \Lambda_2^4)$  and consider parameter choices where  $\kappa \ll 1$ . It follows from Eq. (3.157) that to good approximation

$$\tilde{\rho}/f \approx 2\pi j , \quad (3.158)$$

where  $j$  is an integer. Given our assumption that  $f_1 \gg f_2$ , it follows from Eqs. (3.156)-(3.158) that  $\partial^2 V(\tilde{\rho}, \tilde{\theta}) / \partial \tilde{\rho}^2 > 0$ , confirming that the trench is stable. Substituting Eq. (3.158)

into our original potential yields

$$V(\tilde{\theta}) = \Lambda_1^4 \left[ 1 + \cos \left( \delta + \tilde{\theta}/f_0 \right) \right] , \quad (3.159)$$

where  $\delta = 2\pi scj$  and  $f_0 = f_1/s$ . Setting  $j = 0$  is equivalent to redefining the origin of field space, so we will ignore  $\delta$  henceforth. We note that the present approximation scheme differs from the one used in Ref. [59], in which one would expand the sinusoidal functions in Eq. (3.157) to linear order in their arguments, but is nonetheless accurate as we confirm numerically later. We note that  $s \ll 1$  in the limit  $n \gg 1$ , so that the derived quantity  $f_0$  can be super-Planckian even when the decay constants  $f_1$  and  $f_2$  are not.

We compare the predictions of the model to the latest results from the Planck Collaboration [63]. The slow roll parameters are defined by

$$\epsilon = \frac{1}{2} \left( \frac{V'}{V} \right)^2 , \quad \eta = \frac{V''}{V} \quad \text{and} \quad \gamma = \frac{V' V'''}{V^2} , \quad (3.160)$$

where the primes refer to derivatives with respect to the inflaton field and we work in units where the reduced Planck mass  $M_* \equiv M_P/\sqrt{8\pi} = 1$ . In the present case, these are given by

$$\epsilon = \frac{1}{2f_0^2} \tan^2[\tilde{\theta}/(2f_0)] , \quad (3.161)$$

$$\eta = -\frac{1}{f_0^2} \frac{\cos(\tilde{\theta}/f_0)}{1 + \cos(\tilde{\theta}/f_0)} , \quad (3.162)$$

$$\gamma = -\frac{1}{f_0^4} \tan^2[\tilde{\theta}/(2f_0)] . \quad (3.163)$$

Inflation ends when  $\epsilon(\tilde{\theta}_f) = 1$ . The initial value of the inflaton,  $\tilde{\theta}_i$  is determined by the requirement that we achieve a desired number of e-folds of inflation, given in general by

$$N = \int_{\tilde{\theta}_i}^{\tilde{\theta}_f} \frac{1}{\sqrt{2\epsilon}} d\tilde{\theta} = 2f_0^2 \ln \left[ \frac{\sin[\tilde{\theta}_f/(2f_0)]}{\sin[\tilde{\theta}_i/(2f_0)]} \right] . \quad (3.164)$$

We set  $N = 60$  in the numerical results that follow. We evaluate the slow-roll parameters

and the potential  $V(\tilde{\theta})$  at  $\tilde{\theta}_i$  in determining the spectral index  $n_s = 1 - 6\epsilon + 2\eta$ , the ratio of tensor-to-scalar amplitudes  $r = 16\epsilon$ , the running of the spectral index  $n_r = 16\epsilon\eta - 24\epsilon^2 - 2\gamma$  and the scalar amplitude  $\Delta_R^2 = V/(24\pi^2\epsilon)$ . From Eqs. (3.161)-(3.163), it follows that

$$n_s = 1 + \frac{1}{f_0^2} \left( 1 - 2 \sec^2[\tilde{\theta}_i/(2f_0)] \right) , \quad (3.165)$$

$$r = \frac{8}{f_0^2} \tan^2[\tilde{\theta}_i/(2f_0)] , \quad (3.166)$$

$$n_r = -\frac{2}{f_0^4} \tan^2[\tilde{\theta}_i/(2f_0)] \sec^2[\tilde{\theta}_i/(2f_0)] , \quad (3.167)$$

$$\Delta_R^2 = \frac{1}{12\pi^2} \Lambda_1^4 f_0^2 \left( 1 + \cos[\tilde{\theta}_i/f_0] \right)^3 \csc^2[\tilde{\theta}_i/f_0] . \quad (3.168)$$

To illustrate a viable solution, consider the parameter choice (again, in units where  $M_* = 1$ )

$$f_1 = 0.22\sqrt{2} , \quad (3.169)$$

$$f_2 = f_1/21 , \quad (3.170)$$

$$\Lambda_1 = \Lambda_2 = 0.006 , \quad (3.171)$$

which corresponds to  $n = 21$  and  $\kappa \approx 1/21$ . We find that the initial and final fields for the inflaton trajectory are given by

$$(\tilde{\rho}, \tilde{\theta})_i = (6.04 \times 10^{-4}, 6.74) \quad \text{and} \quad (\tilde{\rho}, \tilde{\theta})_f = (1.50 \times 10^{-4}, 19.14) , \quad (3.172)$$

respectively. Using this value for  $\tilde{\theta}_i$ , we find the following set of cosmological parameters:

$$n_s = 0.96 , \quad (3.173)$$

$$r = 0.060 , \quad (3.174)$$

$$n_r = -0.00046 , \quad (3.175)$$

$$\Delta_R^2 = 2.2 \times 10^{-9} . \quad (3.176)$$

Fig. 3.17 displays the path followed by the inflaton during the 60 e-folds of inflation for this

particular solution. The predictions in Eq. (3.176) are consistent with the results from the Planck experiment [63]:  $n_s = 0.968 \pm 0.006$ ,  $r < 0.12$  (95% C.L.),  $n_r = -0.003 \pm 0.007$  and  $\Delta_R^2 = 2.19 \pm 0.08 \times 10^{-9}$ . (The value of  $\Delta_R^2$ , also called  $A_s$ , was taken from the first column of Table 3 in Ref. [63].)

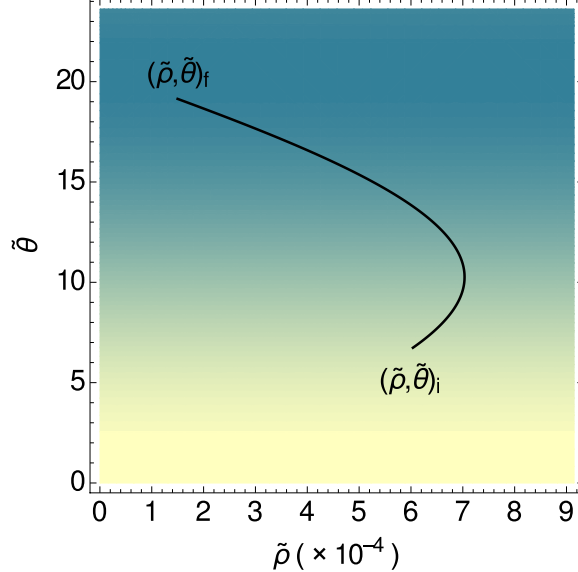


Figure 3.17: Path followed by the inflaton during 60 e-folds of inflation corresponding to the solution of Sec. 3.4.2, in units where  $M_* = 1$ . The background is a density plot where darker zones have lower values of the potential than lighter ones.

We may check the validity of the results in this section by numerically evaluating the slow-roll parameters in the two-field problem. Let  $a$  represent the linear combination of the fields that evolves along the minimum of the trench. Given that  $da = \sqrt{d\tilde{\rho}^2 + d\tilde{\theta}^2}$  along the trench, it follows that we can write the  $n^{th}$  derivative of the potential with respect to  $a$  as

$$\frac{d^n V}{da^n} = \left[ \left( 1 + \frac{d\tilde{\rho}}{d\tilde{\theta}} \right)_{tr}^{-1/2} \frac{d}{d\tilde{\theta}} \right]^n V(\tilde{\theta}, \tilde{\rho}(\tilde{\theta})_{tr}), \quad (3.177)$$

where the subscript “tr” indicates quantities evaluated along  $\tilde{\rho}(\tilde{\theta})_{tr}$ , the solution to Eq. (3.157). Note that as the quantity  $da$  is defined above, the kinetic terms for  $a$  are canonically normalized. The slow roll parameters can be evaluated numerically according to Eq. (3.177).

We find in this case that  $n_s = 0.96$ ,  $r = 0.060$ ,  $n_r = -0.00046$  and  $\Delta_R^2 = 2.2 \times 10^{-9}$ , in agreement with the results in Eq. (3.176).

### Termination with a waterfall.

For different choices of the model parameters, inflation will end before  $\epsilon = 1$  is reached, at a point where there is no longer a solution to Eq. (3.157). At this point, the stability condition  $\partial^2 V / \partial \tilde{\rho}^2 > 0$  is also not satisfied, and the fields evolve rapidly in a direction orthogonal to the original trajectory [59]. If one visualizes the motion by plotting the fields as polar coordinates, the evolution corresponds to a transition from spiraling to rapid motion in the radial direction, eventually ending at a global minimum. In Ref. [59] this was called the waterfall, in analogy to the behavior of hybrid inflation models [42], where stability in one field direction can be a function of the value of a second field.

Given an input of model parameters, we determine the final inflaton field value  $a_f$  by solving

$$\left. \frac{\partial^2 V}{\partial \tilde{\rho}^2} \right|_{tr} = 0 , \quad (3.178)$$

and then the initial value  $a_i$  from

$$N = \int_{a_i}^{a_f} \left| \frac{V'}{V} \right| da . \quad (3.179)$$

where the primes refer to derivatives evaluated numerically according to Eq. (3.177), and  $a$  ( $\approx \tilde{\theta}$ ) is the canonically normalized inflaton field. Again, we set  $N = 60$ . To illustrate a solution that ends with the waterfall behavior, consider the parameter choices

$$f_1 = 0.22\sqrt{2} , \quad (3.180)$$

$$f_2 = f_1/17 , \quad (3.181)$$

$$\Lambda_1 = 3.38 \times 10^{-3} , \quad (3.182)$$

$$\Lambda_2 = 1.61 \times 10^{-3} . \quad (3.183)$$

which corresponds to  $n = 17$  and  $\kappa = 1.13$ . We find that the initial and final fields for the inflaton trajectory are given by

$$(\tilde{\rho}, \tilde{\theta})_i = (6.83 \times 10^{-3}, 1.63) \quad \text{and} \quad (\tilde{\rho}, \tilde{\theta})_f = (0.0281, 5.2970) , \quad (3.184)$$

respectively. Using this value for  $\tilde{\theta}_i$ , we find the following set of cosmological parameters:

$$n_s = 0.96, \quad (3.185)$$

$$r = 0.0078, \quad (3.186)$$

$$n_r = -7.2 \times 10^{-5}, \quad (3.187)$$

$$\Delta_R^2 = 2.2 \times 10^{-9} . \quad (3.188)$$

These are consistent with the ranges allowed by Planck, as quoted in the previous subsection. The complete inflaton trajectory, extending beyond the point where Eq. (3.157) is no longer satisfied, can be found by solving the coupled equations of motion

$$\begin{aligned} \ddot{\rho} + 3H\dot{\rho} + \frac{\partial V}{\partial \rho} &= 0 , \\ \ddot{\theta} + 3H\dot{\theta} + \frac{\partial V}{\partial \theta} &= 0 , \end{aligned} \quad (3.189)$$

where  $H$  is the Hubble parameter. The result is shown in Fig. 3.18. One can see from the plot that the bottom of the trench given by Eq. (3.157), denoted by the thick red line, approximates the actual trajectory, given by the thin green line, very well. The inflaton eventually oscillates about and then settles at the global minimum of the potential.

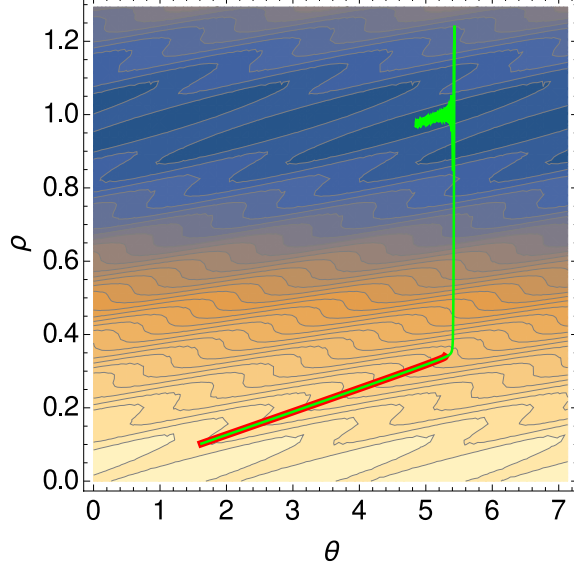


Figure 3.18: Inflaton trajectory, in  $\rho$ - $\theta$  space, overlaid on a contour plot of the potential, in units where  $M_* = 1$ . The bottom of the trench is indicated by the thick red line while the inflation trajectory is denoted by the thin green line.

### 3.4.3 Models

#### Origins of the potential

The successful inflationary trajectories in the previous section are based on a potential of the form

$$V(\rho, \theta) = \Lambda_1^4 \left[ 1 + \cos \left( \frac{\rho}{f_\rho} \right) \right] + \Lambda_2^4 \left[ 1 - \cos \left( \frac{n\rho}{f_\rho} - \frac{\theta}{f_\theta} \right) \right] , \quad (3.190)$$

where  $n$  is an integer. Here in this section, this potential is proposed to arise via the effects of anomalies associated with new gauge groups.

Hence, the standard model gauge group is extended by the additional factors  $SU(N_1) \times SU(N_2)$ , and the fermions  $A_L \sim A_R \sim (\mathbf{N}_1, \mathbf{1})$  and  $B_L^{(i)} \sim B_R^{(i)} \sim C_L \sim C_R \sim (\mathbf{1}, \mathbf{N}_2)$  are introduced. The Lagrangian now contains the following interactions

$$\mathcal{L} \supset h_1 \bar{A}_R A_L \chi + \sum_{i=1}^n h_2^{(i)} \bar{B}_R^{(i)} B_L^{(i)} \chi + h_3 \bar{C}_R C_L \Phi^* + \text{h.c.} . \quad (3.191)$$

Here, the  $h_j$ 's are Yukawa couplings and the terms shown generate heavy fermion masses

when the  $\Phi$  and  $\chi$  fields develop vevs. The accidental global U(1) symmetries are each chiral when appropriate charges are assigned to the  $A$ ,  $B$  and  $C$  fermions. However, these symmetries are anomalous with respect to the new gauge groups. Triangle diagrams lead to the interactions [43, 44]

$$\frac{g_1^2}{32\pi^2} \left( \frac{\rho}{f_\rho} \right) F_1 \tilde{F}_1 + \frac{g_2^2}{32\pi^2} \left( \frac{n\rho}{f_\rho} - \frac{\theta}{f_\theta} \right) F_2 \tilde{F}_2 , \quad (3.192)$$

and the non-perturbative generation of a potential [43, 44]

$$V(\rho, \theta) = \Lambda_1^4 \left[ 1 - \cos \left( \frac{\rho}{f_\rho} \right) \right] + \Lambda_2^4 \left[ 1 - \cos \left( \frac{n\rho}{f_\rho} - \frac{\theta}{f_\theta} \right) \right] , \quad (3.193)$$

with the scales  $\Lambda_1$  and  $\Lambda_2$  identified with the scale of strong dynamics for each SU( $N$ ) factor. (We assume  $N_1$  and  $N_2$  are chosen so that each group is asymptotically free.) Redefining the origin of field space via

$$\rho \rightarrow \rho + \pi f_\rho \quad \text{and} \quad \theta \rightarrow \theta + n\pi f_\theta \quad (3.194)$$

puts the potential in the form that we previously assumed in Eq. (3.190). Note that the new gauge groups may be spontaneously broken at a scale well below  $\Lambda_1$  and  $\Lambda_2$  without affecting our conclusions.

The interactions given in Eq. (3.191) are clearly not generic. In the absence of the discrete charge assignments for  $\Phi$  and  $\chi$ , there would be no reason for the  $\Phi$  field to avoid coupling to the  $A$  and  $B$ -type fermions directly, nor would there be any prohibition of explicit fermion mass terms. Hence, this sector is suggestive of additional symmetries even had they not been put forward immediately as a starting assumption in our model building. Given the transformation properties of  $\Phi$  and  $\chi$  fields under the  $\mathbf{Z}_p^\Phi \times \mathbf{Z}_r^\chi$  symmetry, Eq. (3.149), one can account for the desired pattern on couplings in Eq. (3.191) by choosing

$$A_R \rightarrow \omega_\chi A_R , \quad B_R^{(i)} \rightarrow \omega_\chi B_R^{(i)} , \quad C_L \rightarrow \omega_\Phi C_L , \quad (3.195)$$

with the remaining heavy fermions taken as singlets under the discrete group. However, the fermion content must now be enlarged to assure that discrete gauge anomalies are cancelled (see the appendix), and do so in a way that assures that the additional fermions can become massive. To demonstrate that this can be accomplished, one considers an example suggested by one of the previous cosmological solutions, discussed in Sec. 3.4.2, corresponding to the potential in Eq. (3.190) with  $n = 21$ . Choosing  $p = r = 21$  means that there are 21  $B$ -type fermions transforming each with  $\mathbf{Z}_{21}^\chi$  charge +1, where the charge  $Q$  is specified by defining the group element to be  $\exp(2i\pi Q/21)$ . This implies that the  $\mathbf{Z}_{21}^\chi$ - $SU(N_2)^2$  discrete anomaly cancellation condition would be satisfied by the  $B$  particle content alone. The  $A$  and  $C$  fermions, on the other hand, lead to anomalies, so additional fermions are included with matching gauge quantum numbers and the discrete transformation rules

$$\begin{aligned} A_R^{(i)} &\rightarrow \omega_\chi^{10} A_R^{(i)} & , & \quad A_L^{(i)} \rightarrow A_L^{(i)} & \quad (i = 1 \dots 2) \\ C_L^{(i)} &\rightarrow \omega_\Phi^{10} C_L^{(i)} & , & \quad C_R^{(i)} \rightarrow C_R^{(i)} & \quad (i = 1 \dots 2) \end{aligned} \quad (3.196)$$

which allow the anomaly cancellation conditions to be satisfied. Finally, these fields will develop masses as a result of Planck-suppressed operators, for example,  $\bar{A}_R^{(i)} \chi^{10} A_L^{(i)} / M_*^9 + \text{h.c.}$  and  $\bar{C}_L^{(i)} \Phi^{10} C_R^{(i)} / M_*^9 + \text{h.c.}$ , which lead to masses of order  $\lambda^{10} M_* \sim 10^{11}$  GeV.

The discrete symmetry that are assumed to assure the form of couplings in Eq. (3.191) also leads to a suppression of direct Planck suppressed corrections to the potential. Since quantum gravitational effects must respect the discrete gauge symmetry, the lowest order operators that will correct the potential have the form  $\Phi^{21}/M_*^{17}$  or  $\chi^{21}/M_*^{17}$ ; the scale of these corrections are of order  $\lambda^{21} M_*^4 \sim 10^{-14} M_*^4$ , negligible compared to the values of  $\Lambda_1$  and  $\Lambda_2$  that are found previously to be of order  $10^{-3} M_*$ .

## Standard Model Flavor

The fields  $\Phi$  and  $\chi$  can now be utilized in constructing models of standard model fermion masses. These fields will appear in higher-dimension operators that generate the small entries of the standard model Yukawa matrices. Given the choice  $\langle \Phi \rangle / M_* = \langle \chi \rangle / M_* = \lambda$ ,

$Q_{1L}$	$Q_{2L}$	$Q_{3L}$	$u_R^c$	$c_R^c$	$t_R^c$	$d_R^c$	$s_R^c$	$b_R^c$
6	5	3	2	-1	-3	-1	-2	-2

$L_{1L}$	$L_{2L}$	$L_{3L}$	$e_R^c$	$\mu_R^c$	$\tau_R^c$	$\nu_{1R}^c$	$\nu_{2R}^c$	$\nu_{3R}^c$
0	0	0	5	3	1	-3	-3	-3

Table 3.3:  $\mathbf{Z}_{21}^\Phi$  charge assignments  $q$ , where the group transformation is defined by  $\exp(2i\pi q/21)$ . The Higgs doublet is a singlet under the flavor symmetry.

the size of these entries will be determined by powers of the Cabibbo angle  $\lambda$ . In the example presented in this section, the desired set of higher-dimension operators is obtained via the same discrete symmetries that were used to obtain the inflaton potential. Based on the  $n = p = r = 21$  model just discussed, the  $\Phi$  and  $\chi$  fields each transform under a separate  $\mathbf{Z}_{21}$  symmetry. Of course, other choices of the symmetry group are possible, and the present choice does not suggest a unique set of fermion charge assignments (since there are many possible Yukawa textures that are viable). The example given here will suffice by serving as a proof of principle<sup>2</sup>.

The simplest incorporation of the  $n = 21$  model in a flavor sector is via the identification of  $\mathbf{Z}_{21}^\Phi$  as the flavor symmetry and  $\Phi$  as the sole flavon field. The charge assignments of the standard model fermions and a set of right-handed neutrinos are given in Table 3.3. Entries of the Yukawa matrices arise from  $\mathbf{Z}_{21}^\Phi$ -invariant higher dimension operators. For example, the 1-1 entry in the up-sector Yukawa matrix involves the fields  $\bar{Q}_{1L}H u_R$ , which has flavor charge  $-8$ . This arises at lowest order via

$$\frac{1}{M_*^8} \bar{Q}_{1L} H \Phi^8 u_R + \text{h.c.}, \quad (3.197)$$

and hence the corresponding Yukawa matrix entry is of order  $\lambda^8$ . Since  $\omega^8$  and  $\omega^{-13}$  are identical, there is another possible operator,  $\bar{Q}_{1L} H \Phi^{*13} u_R / M_*^{13} + \text{h.c.}$ , but it is of higher

---

<sup>2</sup>It should also be clear that one could alternatively construct a model starting with the  $n = 17$  potential that we discussed earlier, but there are no new qualitative insights gained by presenting two very similar examples.

order and can be neglected. It may be populated that the remaining entries of the quark and charged lepton Yukawa matrices in a similar manner. One finds

$$Y_u = \begin{pmatrix} \lambda^8 & \lambda^5 & \lambda^3 \\ \lambda^7 & \lambda^4 & \lambda^2 \\ \lambda^5 & \lambda^2 & 1 \end{pmatrix}, \quad Y_d = \begin{pmatrix} \lambda^5 & \lambda^4 & \lambda^4 \\ \lambda^4 & \lambda^3 & \lambda^3 \\ \lambda^2 & \lambda & \lambda \end{pmatrix}, \quad Y_e = \begin{pmatrix} \lambda^5 & \lambda^3 & \lambda \\ \lambda^5 & \lambda^3 & \lambda \\ \lambda^5 & \lambda^3 & \lambda \end{pmatrix}, \quad (3.198)$$

where order one coefficients in each entry have been suppressed. These achieve the desired ratios  $m_u/m_t \sim \lambda^8$ ,  $m_c/m_t \sim \lambda^4$ ,  $m_d/m_b \sim \lambda^4$ , and  $m_s/m_b \sim \lambda^2$ , with the charged lepton Yukawa mass eigenvalues comparable in size to those of the down quark sector. It is not hard to verify that the choice of right-handed neutrino charge assignments leads via the see-saw mechanism to a neutrino mass matrix of the form  $[\langle H \rangle^2/\Lambda_R]Y_\nu$ , where  $\Lambda_R$  is the right-handed neutrino mass scale,  $\langle H \rangle$  is the standard model Higgs vev, and  $Y_\nu$  is a matrix in which each entry is of order  $\lambda^0$  times a function of (typically many) undetermined order one coefficients. These can be chosen to obtain the desired phenomenology without unnaturally large or small values of the individual coefficient <sup>3</sup>.

Finally, one must check that the standard model fermion charge assignments in this model satisfy the linear Ibáñez-Ross anomaly cancellation conditions for the non-Abelian gauge groups and gravity. Summing the  $\mathbf{Z}_{21}^\Phi$  charges times the appropriate multiplicity factors for the color SU(3), weak SU(2), and gravitational anomalies gives 21, 42 and 63, respectively. These results mod 21 are zero, indicating that the discrete gauge anomaly cancellation conditions discussed in Appendix A remain satisfied.

### 3.4.4 Comments

Models of standard model flavor that are based on discrete gauge symmetries can have accidental continuous global symmetries that are spontaneously broken. We have argued

---

<sup>3</sup>It is not necessarily the case that an alternative model that predicts the neutrino mass hierarchy via powers of  $\lambda$  is more desirable than this example. The reason is that the predictions for neutrino mass matrix entries in such a model also come multiplied by functions of products of a number of the order one operator coefficients. This can spoil the naive  $\lambda$  power counting without any individual operator coefficient being unnaturally small or large. This is a problem that is unique to the neutrino sector in such models when the mass matrix arises via the seesaw mechanism.

that a linear combination of the approximate goldstone bosons that may arise in these models can serve plausibly as the inflaton in two-field models of inflation based on the axion monodromy idea. These models can accommodate the current Planck data on the microwave background [63] while allowing the flavor-symmetry-breaking vacuum expectation values (vevs) to remain sub-Planckian. This is important in the present work since the ratios of the flavon vevs to the reduced Planck scale serve as small flavor-symmetry-breaking parameters in our models, which allows one to predict the standard model Yukawa coupling entries in a controlled approximation. In addition to making correct Yukawa coupling predictions possible, the discrete symmetries of the theory also maintain the correct pattern of the interactions in a new gauge sector, leading to the desired form of the inflaton potential; they also keep the quantum gravitational corrections to the potential well under control. The literature on models of standard model fermion masses is vast and it is imaginable that more economical and compelling examples of flavor-sector inflation models are yet to be found. The present work suggests that exploring the full landscape of such models may be a fertile direction for future investigation.

# Chapter 4

## Conclusions

The first part of this dissertation examined the quantitative success of holographic superconductors by analyzing the model sensitivity to the higher-dimensional spacetime geometry. The motivation of this research arises from the freedom over the choice of the background geometry in these phenomenological models inspired by AdS/CFT. It would be intriguing to find any generic features of holographic superconductors which are independent of the higher dimensional metric. We have presented the dependence of the charged condensate and complex conductivity on a class of geometric backgrounds. A desired feature of holographic superconductors as models of unconventional superconductors is their prediction of a higher ratio of superconducting gap to the critical temperature than conventional metal superconductors. However, this feature is shown to strongly depend on the choice of the background metric and can be a lot smaller in the deconstructed models. We have also found that in the continuum models, independent of background metric, the gap frequency equals the charged condensate.

The second part of this dissertation focused on inflation models capable of producing observably large primordial gravitational waves (tensor modes) while allowing enough  $e$ -folds of inflation to explain the statistical uniformity of the observable universe, evading the Lyth bound. We provide a two-field axion-monodromy scheme in which the potential assumes a “Mexican Hat”-like form and the system spirals down the hill along a prescribed

trench. With a particular range of parameters, inflation terminates as the trench loses stability and the system approaches the global minimum of the field space rapidly. We also considered the effects of a nontrivial field-space metric on the predictions for inflationary observables in a series of models. The final section of the inflation chapter tries to embed the axion-monodromy model as an extension of the standard model of particles. We propose a scenario in which the two axions from the inflation model are identified as the pseudo-goldstone bosons from the broken accidental continuous global symmetries of the flavor sector, which is designed to address the fermion mass hierarchy.

## Appendix A

# Discrete Gauge Symmetries, Briefly

It is well known that continuous gauge symmetries are not violated by quantum gravitational effects. Under what circumstances is the same true for discrete symmetries? It was noted long ago by Ibáñez and Ross (IR) [72] that a discrete group that arises as a subgroup of a continuous gauge symmetry inherits this protection. While the full theory must satisfy the anomaly cancellation conditions relevant for the continuous gauge groups, IR determined the conditions that are relevant in the low-energy theory, below the scale at which the continuous gauge symmetries are broken. Since some of the fermions in the complete theory may become massive and decoupled when symmetry breaking occurs, the low-energy theory includes only part of the fermion content that contributes to anomaly cancellation in the full theory. The low-energy constraints should refer only to the light fermion content, which in the present context corresponds to models defined below the reduced Planck scale  $M_*$ . If the appropriate consistency conditions are satisfied, the discrete gauge symmetry can be treated as fundamental, without reference to specific high-energy embeddings.

The constraints that we apply in our model building are the linear IR conditions involving non-Abelian gauge group factors; these follow from triangle diagrams involving two non-Abelian gauge group factors and one factor of the continuous gauge group in which

the discrete symmetry is embedded. For example, the  $\mathbf{Z}_N\text{-SU}(M)^2$  anomaly cancellation condition is [72]

$$\sum_i C_i q_i = \frac{1}{2} r N . \quad (\text{A.1})$$

Here  $r$  is an integer,  $q_i$  is the  $\mathbf{Z}_N$  charge of the  $i^{\text{th}}$  fermion (which transforms under  $\mathbf{Z}_N$  by  $\exp[i2\pi q_i/N]$ ) and  $C_i$  is the Casimir invariant given by  $\text{Tr}(T^a T^b) = C_i \delta^{ab}$ , where the  $T^a$  are  $\text{SU}(M)$  generators in the representation of the  $i^{\text{th}}$  fermion. Since all the fermions in the model presented in Sec. 3.4.3 are in the fundamental representations of the relevant  $\text{SU}(M)$  gauge groups,  $C_i = 1/2$ ; the linear IR conditions simply requires that the  $\mathbf{Z}_N$  charges of the fermions that transform under a specified  $\text{SU}(M)$  factor sum to an integer multiple of  $N$ . According to IR, when  $N$  is odd (relevant to the model of Sec. 3.4.3) the gravitational anomalies linear in  $\mathbf{Z}_N$  are cancelled when the sum of all the  $\mathbf{Z}_N$  charges are also an integer multiple of  $N$ . It is straightforward to verify that these conditions are satisfied by the charge assignments displayed in Table 3.3.

What about the other possible anomaly cancellation conditions? First, IR note that the linear conditions involving the Abelian gauge groups do not lead to any useful constraints on the low-energy theory [72]. Banks and Dine (BD) [73] later showed that the IR conditions non-linear in the discrete group make a tacit assumption about the high-energy embedding of the theory, through the requirement that both the light and the heavy fermions have integer U(1) charges. BD show that there are consistent, non-anomalous theories (ones in which the effective discrete symmetry at low energies is smaller than that of the full theory) in which the low-energy spectrum does not satisfy the non-linear IR constraints; their failure only implies the existence of heavy fermions with fractional charges. Thus, the non-linear IR conditions are not required for the consistency of the low-energy effective theory. BD note that the surviving discrete anomaly cancellation conditions are physically sensible: for example, the condition for the cancellation of the  $\mathbf{Z}_N\text{-SU}(M)^2$  anomaly also guarantees that there are no t'Hooft interactions generated by  $\text{SU}(M)$  instantons that would explicitly break the  $\mathbf{Z}_N$  symmetry. This physical constraint [74] is completely independent of the high-energy embedding.

# Bibliography

- [1] G. F. de Teramond and S. J. Brodsky, Phys. Rev. Lett. **94**, 201601 (2005) [hep-th/0501022]; J. Erlich, E. Katz, D. T. Son and M. A. Stephanov, Phys. Rev. Lett. **95**, 261602 (2005) [hep-ph/0501128]; J. Erlich, Int. J. Mod. Phys. A **25**, 411 (2010) [arXiv:0908.0312 [hep-ph]].
- [2] T. Sakai and S. Sugimoto, Prog. Theor. Phys. **113**, 843 (2005) [hep-th/0412141]; T. Sakai and S. Sugimoto, Prog. Theor. Phys. **114**, 1083 (2005) [hep-th/0507073].
- [3] C. Csaki, C. Grojean, H. Murayama, L. Pilo and J. Terning, Phys. Rev. D **69**, 055006 (2004) [hep-ph/0305237]; J. Hirn and V. Sanz, Phys. Rev. Lett. **97**, 121803 (2006) [hep-ph/0606086]; M. Piai, hep-ph/0609104; C. D. Carone, J. Erlich and J. A. Tan, Phys. Rev. D **75**, 075005 (2007) [hep-ph/0612242].
- [4] S. S. Gubser, Phys. Rev. D **78**, 065034 (2008) [arXiv:0801.2977 [hep-th]]. S. S. Gubser, C. P. Herzog, S. S. Pufu and T. Tesileanu, Phys. Rev. Lett. **103**, 141601 (2009) [arXiv:0907.3510 [hep-th]].
- [5] S. A. Hartnoll, C. P. Herzog and G. T. Horowitz, Phys. Rev. Lett. **101**, 031601 (2008) [arXiv:0803.3295 [hep-th]]; S. A. Hartnoll, C. P. Herzog and G. T. Horowitz, JHEP **0812**, 015 (2008) [arXiv:0810.1563 [hep-th]].
- [6] J. Erlich and C. Westenberger, Phys. Rev. D **79**, 066014 (2009) [arXiv:0812.5105 [hep-ph]].

- [7] S. J. Brodsky and R. Shrock, Phys. Lett. B **666**, 95 (2008) [arXiv:0806.1535 [hep-th]]; G. F. de Teramond and S. J. Brodsky, Phys. Rev. Lett. **102**, 081601 (2009) [arXiv:0809.4899 [hep-ph]].
- [8] A. L. Fitzpatrick, J. Kaplan, E. Katz and L. Randall, arXiv:1304.3458 [hep-th].
- [9] C. T. Hill, S. Pokorski and J. Wang, Phys. Rev. D **64**, 105005 (2001) [hep-th/0104035].
- [10] N. Arkani-Hamed, A. G. Cohen and H. Georgi, Phys. Rev. Lett. **86**, 4757 (2001) [hep-th/0104005].
- [11] N. Arkani-Hamed, A. G. Cohen and H. Georgi, Phys. Lett. B **513**, 232 (2001) [hep-ph/0105239].
- [12] D. Albrecht, C. D. Carone and J. Erlich, Phys. Rev. D **86**, 086005 (2012) [arXiv:1208.2700 [hep-th]].
- [13] J. M. Bardeen, B. Carter and S. W. Hawking, Commun. Math. Phys. **31** (1973) 161; J. D. Bekenstein, Phys. Rev. D **7** (1973) 2333.
- [14] J. M. Maldacena, Int. J. Theor. Phys. **38**, 1113 (1999) [Adv. Theor. Math. Phys. **2**, 231 (1998)] [hep-th/9711200].
- [15] D. T. Son and A. O. Starinets, JHEP **0209**, 042 (2002) [hep-th/0205051].
- [16] V. Balasubramanian, P. Kraus, A. E. Lawrence and S. P. Trivedi, Phys. Rev. D **59**, 104021 (1999) doi:10.1103/PhysRevD.59.104021 [hep-th/9808017].
- [17] D. van Delft and P. Kes, Physics Today **63**, 38-43 (2010), *The discovery of superconductivity*
- [18] J. G. Bednorz and K. A. Muller, Z. Phys. B **64**, 189 (1986).
- [19] E. Witten, Adv. Theor. Math. Phys. **2**, 505 (1998) [hep-th/9803131].
- [20] E. Kiritsis and V. Niarchos, JHEP **1107**, 112 (2011) [Erratum-ibid. **1110**, 095 (2011)] [arXiv:1105.6100 [hep-th]].

- S. A. Hartnoll, J. Polchinski, E. Silverstein and D. Tong, JHEP **1004**, 120 (2010) [arXiv:0912.1061 [hep-th]].
- [21] A. A. Starobinsky, Phys. Lett. B **91**, 99 (1980). doi:10.1016/0370-2693(80)90670-X
- [22] A. H. Guth, Phys. Rev. D **23**, 347 (1981). doi:10.1103/PhysRevD.23.347
- [23] A. D. Linde, Phys. Lett. B **108**, 389 (1982). doi:10.1016/0370-2693(82)91219-9
- [24] S. Dodelson, Amsterdam, Netherlands: Academic Pr. (2003) 440 p
- [25] A. R. Liddle and D. H. Lyth, Cambridge, UK: Univ. Pr. (2000) 400 p
- [26] M. Kamionkowski, A. Kosowsky and A. Stebbins, Phys. Rev. D **55**, 7368 (1997) doi:10.1103/PhysRevD.55.7368 [astro-ph/9611125].
- [27] M. Zaldarriaga and U. Seljak, Phys. Rev. D **55**, 1830 (1997) doi:10.1103/PhysRevD.55.1830 [astro-ph/9609170].
- [28] J. Lazear, P. A. R. Ade, D. Benford, C. L. Bennett, D. T. Chuss, J. L. Dotson, J. R. Eimer and D. J. Fixsen *et al.*, arXiv:1407.2584 [astro-ph.IM].
- [29] P. A. R. Ade *et al.* [BICEP2 Collaboration], Phys. Rev. Lett. **112**, 241101 (2014) [arXiv:1403.3985 [astro-ph.CO]].
- [30] U. Seljak and M. Zaldarriaga, Phys. Rev. Lett. **78**, 2054 (1997) [astro-ph/9609169].
- [31] M. Kamionkowski, A. Kosowsky and A. Stebbins, Phys. Rev. Lett. **78**, 2058 (1997) [astro-ph/9609132].
- [32] R. Flauger, J. C. Hill and D. N. Spergel, JCAP **1408**, 039 (2014) [arXiv:1405.7351 [astro-ph.CO]].
- [33] M. J. Mortonson and U. Seljak, arXiv:1405.5857 [astro-ph.CO].
- [34] R. Adam *et al.* [ Planck Collaboration], arXiv:1409.5738 [astro-ph.CO].
- [35] D. H. Lyth, Phys. Rev. Lett. **78**, 1861 (1997) [hep-ph/9606387].

- [36] M. Carrillo-Gonzlez, G. Germn-Velarde, A. Herrera-Aguilar, J. C. Hidalgo and R. Sussman, Phys. Lett. B **734**, 345 (2014) [arXiv:1404.1122 [astro-ph.CO]].
- [37] C. D. Carone, J. Erlich, M. Sher and R. Ramos, arXiv:1407.6017 [hep-ph].
- [38] L. McAllister, E. Silverstein and A. Westphal, Phys. Rev. D **82**, 046003 (2010) [arXiv:0808.0706 [hep-th]].
- [39] J. E. Kim, H. P. Nilles and M. Peloso, JCAP **0501**, 005 (2005) [hep-ph/0409138].
- [40] M. Berg, E. Pajer and S. Sjors, Phys. Rev. D **81**, 103535 (2010) [arXiv:0912.1341 [hep-th]].
- [41] A. D. Linde, Phys. Lett. B **129**, 177 (1983).
- [42] A. D. Linde, Phys. Rev. D **49**, 748 (1994) [astro-ph/9307002].
- [43] J. McDonald, JCAP **1501**, no. 01, 018 (2015) doi:10.1088/1475-7516/2015/01/018 [arXiv:1407.7471 [hep-ph]].
- [44] J. McDonald, JCAP **1505**, no. 05, 014 (2015) doi:10.1088/1475-7516/2015/05/014 [arXiv:1412.6943 [hep-ph]].
- [45] P. A. R. Ade *et al.* [Planck Collaboration], arXiv:1303.5082 [astro-ph.CO].
- [46] T. Li, Z. Li and D. V. Nanopoulos, JCAP **1404**, 018 (2014) [arXiv:1310.3331 [hep-ph]].
- [47] S. V. Ketov and T. Terada, arXiv:1509.00953 [hep-th].
- [48] M. Yamaguchi, Class. Quant. Grav. **28**, 103001 (2011) [arXiv:1101.2488 [astro-ph.CO]].
- [49] J. O. Gong and T. Tanaka, JCAP **1103**, 015 (2011) [JCAP **1202**, E01 (2012)] [arXiv:1101.4809 [astro-ph.CO]].
- [50] S. Cremonini, Z. Lalak and K. Turzynski, Phys. Rev. D **82**, 047301 (2010) doi:10.1103/PhysRevD.82.047301 [arXiv:1005.4347 [hep-th]].
- [51] K. Freese, J. A. Frieman and A. V. Olinto, Phys. Rev. Lett. **65**, 3233 (1990).

- [52] F. C. Adams, J. R. Bond, K. Freese, J. A. Frieman and A. V. Olinto, Phys. Rev. D **47**, 426 (1993) [hep-ph/9207245].
- [53] A. R. Liddle, A. Mazumdar and F. E. Schunck, Phys. Rev. D **58**, 061301 (1998) [astro-ph/9804177].
- [54] E. J. Copeland, A. Mazumdar and N. J. Nunes, Phys. Rev. D **60**, 083506 (1999) [astro-ph/9904309].
- [55] D. E. Kaplan and N. J. Weiner, JCAP **0402**, 005 (2004) [hep-ph/0302014].
- [56] N. Arkani-Hamed, H. C. Cheng, P. Creminelli and L. Randall, JCAP **0307**, 003 (2003) [hep-th/0302034].
- [57] S. Dimopoulos, S. Kachru, J. McGreevy and J. G. Wacker, JCAP **0808**, 003 (2008) [hep-th/0507205].
- [58] E. Silverstein and A. Westphal, Phys. Rev. D **78**, 106003 (2008) [arXiv:0803.3085 [hep-th]].
- [59] C. D. Carone, J. Erlich, A. Sen Sharma and Z. Wang, Phys. Rev. D **91**, no. 4, 043512 (2015) [arXiv:1410.2593 [hep-ph]].
- [60] G. Barenboim and W. I. Park, arXiv:1412.2724 [hep-ph]; Phys. Rev. D **91**, no. 6, 063511 (2015) [arXiv:1501.00484 [hep-ph]].
- [61] G. Barenboim and W. I. Park, Phys. Rev. D **91**, no. 6, 063511 (2015) [arXiv:1501.00484 [hep-ph]].
- [62] G. Barenboim and W. I. Park, arXiv:1504.02080 [astro-ph.CO].
- [63] P. A. R. Ade *et al.* [Planck Collaboration], arXiv:1502.02114 [astro-ph.CO].
- [64] C. Gordon, D. Wands, B. A. Bassett and R. Maartens, Phys. Rev. D **63**, 023506 (2001) doi:10.1103/PhysRevD.63.023506 [astro-ph/0009131].

- [65] S. Groot Nibbelink and B. J. W. van Tent, *Class. Quant. Grav.* **19**, 613 (2002) doi:10.1088/0264-9381/19/4/302 [hep-ph/0107272].
- [66] Z. Lalak, D. Langlois, S. Pokorski and K. Turzynski, *JCAP* **0707**, 014 (2007) doi:10.1088/1475-7516/2007/07/014 [arXiv:0704.0212 [hep-th]].  
A. H. Guth, *Phys. Rev. D* **23**, 347 (1981); A. D. Linde, *Phys. Lett. B* **108**, 389 (1982);  
A. Albrecht and P. J. Steinhardt, *Phys. Rev. Lett.* **48**, 1220 (1982).
- [67] D. H. Lyth, *Lect. Notes Phys.* **738**, 81 (2008) [hep-th/0702128].
- [68] S. Antusch, S. F. King, M. Malinsky, L. Velasco-Sevilla and I. Zavala, *Phys. Lett. B* **666**, 176 (2008) [arXiv:0805.0325 [hep-ph]].
- [69] R. Kallosh, A. D. Linde, D. A. Linde and L. Susskind, *Phys. Rev. D* **52**, 912 (1995) [hep-th/9502069].  
M. Czerny and F. Takahashi, *Phys. Lett. B* **733**, 241 (2014) [arXiv:1401.5212 [hep-ph]].
- [70] T. Li, Z. Li and D. V. Nanopoulos, arXiv:1507.04687 [hep-th]; *Phys. Rev. D* **91**, no. 6, 061303 (2015) [arXiv:1409.3267 [hep-th]]; arXiv:1412.5093 [hep-th].
- [71] J. Erlich, J. Olsen and Z. Wang, arXiv:1509.06781 [hep-ph].
- [72] L. E. Ibáñez and G. G. Ross, *Phys. Lett. B* **260**, 291 (1991).
- [73] T. Banks and M. Dine, *Phys. Rev. D* **45**, 1424 (1992) [hep-th/9109045].
- [74] J. Preskill, S. P. Trivedi, F. Wilczek and M. B. Wise, *Nucl. Phys. B* **363**, 207 (1991).

# Vita

Zhen Wang was born in Wanzhou, China. He graduated from Sichuan University in Chengdu, China with a Bachelor of Science degree in Physics in June, 2010. In August 2010, he started his Ph.D. education in the Physics Department of William and Mary. He obtained a Master of Science degree in Physics from The College of William and Mary in May, 2012.